

THE BORON DOPING OF SINGLE CRYSTAL DIAMOND FOR HIGH POWER DIODE
APPLICATIONS

By

Shannon Singer Nicley

A DISSERTATION

Submitted to
Michigan State University
in partial fulfillment of the requirements
for the degree of

Electrical Engineering - Doctor of Philosophy

2015

ABSTRACT

THE BORON DOPING OF SINGLE CRYSTAL DIAMOND FOR HIGH POWER DIODE APPLICATIONS

By

Shannon Singer Nicley

Diamond has the potential to revolutionize the field of high power and high frequency electronic devices as a superlative electronic material. The realization of diamond electronics depends on the control of the growth process of both lightly and heavily boron doped diamond. This dissertation work is focused on furthering the state of the art of boron doped diamond (BDD) growth toward the realization of high power diamond Schottky barrier diodes (SBDs). The achievements of this work include the fabrication of a new dedicated reactor for lightly boron doped diamond deposition, the optimization of growth processes for both heavily and lightly boron doped single crystal diamond (SCD), and the proposal and realization of the corner architecture SBD. Boron doped SCD is grown in microwave plasma-assisted chemical vapor deposition (MPACVD) plasma disc bell-jar reactors, with feedgas mixtures including hydrogen, methane, carbon dioxide, and diborane. Characterization methods for the analysis of BDD are described, including Fourier-transformed infrared spectroscopy (FTIR), Secondary Ion Mass Spectroscopy (SIMS) and temperature-dependent four point probe conductivity for activation energy. The effect of adding carbon dioxide to the plasma feedgas for lightly boron doped diamond is investigated. The effect of diborane levels and other growth parameters on the incorporated boron levels are reported, and the doping efficiency is calculated over a range of boron concentrations. The presence of defects is shown to affect the doping uniformity. The substrate growth temperature dependence of the plasma gas-phase to solid-phase doping efficiency in heavily boron doped SCD deposition is investigated. The substrate temperature

during growth is shown to have a significant effect on the grown sample defect morphology, and a temperature dependence of the doping efficiency is also shown. The effect of the growth rate on the doping efficiency is discussed, and the ratio of the boron concentration in the gas phase to the flux of carbon incorporated into the solid diamond phase is shown to be a more predictive measure of the resulting boron concentration than the gas phase boron to carbon ratio that is more commonly reported. The corner architecture SBD structure is proposed as an alternative vertical architecture for the realization of high power, high temperature, single crystal diamond diodes. The lightly doped layer of the diode is grown in a direction perpendicular to the previous epitaxial growth of the heavily doped layer, to reduce the threading type dislocations in the active region of the fabricated diodes. The first-ever corner architecture SBD is fabricated and evaluated for diode performance, using the regimes identified for high quality boron doped diamond deposition at light and heavy doping levels.

To my parents

TABLE OF CONTENTS

LIST OF TABLES	viii
LIST OF FIGURES	ix
Chapter 1 Background and Motivation	1
1.1 Introduction	2
1.2 Material Evaluation for Extreme Electrical Applications	3
1.3 Principles of Diamond Schottky Barrier Design	6
1.3.1 Schottky Barrier Diode Background and Theory	6
1.3.2 Vertical Schottky Barrier Diodes	8
1.4 Chemical Structure of Diamond	10
1.4.1 Crystal Structure	10
1.4.2 Dislocations	14
1.4.2.1 Edge Dislocations	15
1.4.2.2 Screw Dislocations	15
1.4.2.3 Mixed Dislocations	15
1.5 Electronic Structure of Diamond	16
1.6 Chemical Vapor Deposition of Diamond	17
1.6.1 The Historical Development of Chemical Vapor Deposition of Diamond	18
1.6.2 Types of CVD Reactors	22
1.6.2.1 Hot Filament Reactors	22
1.6.2.2 Microwave Plasma Reactors	23
1.6.2.2.1 NIRIM-type Reactors	23
1.6.2.2.2 ASTeX-type Bell-Jar Reactors	26
1.6.2.2.3 MSU-type Reactors	26
1.7 Boron Doping of Single Crystal Diamond	34
1.7.1 Defects	34
1.7.2 Unintentional Doping	36
1.7.3 Compensation	37
1.7.4 Soot Formation	38
1.7.5 Doping Efficiency	39
1.7.6 Growth Rate	39
1.8 Surface Conductivity	40
Chapter 2 Experimental Methodology	43
2.1 Experimental Diamond Deposition Reactor Systems	44
2.1.1 Diamond System 1 (DS1)	45
2.1.1.1 Gas Flow Control and Vacuum Systems	45
2.1.2 Diamond System 6 (DS6)	46
2.1.2.1 Gas Flow Control and Vacuum Systems	48

2.1.2.2	Microwave Power Supply and Waveguide/Transmission System	55
2.1.2.3	Cooling System	59
2.1.3	Measurement of Experimental Output Variables	63
2.1.3.1	Sample Temperature During Deposition	64
2.1.3.2	Grown Thickness and Growth Rate	65
2.2	Fourier Transformed Infrared Spectroscopy	65
2.2.1	Infrared Analysis of Lightly Boron Doped Diamond	67
2.2.2	Infrared Analysis of Heavily Boron Doped Diamond	73
2.2.2.1	Chrenko Calibration	73
2.2.2.2	Burns Calibration	77
2.2.2.3	Novikov Calibration	78
2.2.2.4	Davies Calibration	80
2.3	Secondary Ion Mass Spectroscopy (SIMS)	82
2.4	Temperature Dependent Four Point Probe Measurements	82
2.5	Contact Angle for Surface Termination	85
2.6	X-Ray Diffraction (XRD) for Miscut Angle Determination	89
Chapter 3	Low Level Boron Doping	90
3.1	Lightly Boron Doped Diamond Growth in DS1	91
3.2	Carbon Dioxide in the Plasma Feedgas	92
3.3	Electrical Characterization	95
3.4	Defects and the Uniformity of Doping	99
3.5	New Low Boron Doping System (DS6) Results	101
Chapter 4	Heavy Boron Doping	106
4.1	Effect of Substrate Temperature During Growth	107
4.1.1	Temperature Dependent Defect Morphology	110
4.1.2	Temperature Dependent Doping Efficiency	111
4.1.3	Temperature Dependence of the Center Growth Rate	112
4.1.4	Gas Phase Boron to Carbon Flux Ratio as a Predictor of Boron Concentration	114
4.1.5	Comparison of FTIR and SIMS for boron concentration	115
4.2	Effect of Feedgas Flow Rate	118
Chapter 5	Corner-Architecture Schottky Barrier Diodes	123
5.1	Corner Architecture Diode Fabrication	124
5.1.1	Heavy Boron Doped Deposition	125
5.1.2	Laser Cutting and Polishing	125
5.1.3	Lightly Boron Doped Deposition	127
5.1.4	Contact Deposition	127
5.2	Diode Characterization	128
5.2.1	Reverse Characteristics	130
5.2.2	Position Dependence of Diode Performance	131
5.2.3	Ideality Factor and Rectification Ratio	132
5.2.4	Forward Characteristics	134

Chapter 6 Summary and Conclusions	137
6.1 Low Level Boron Doping	138
6.2 Heavy Boron Doping	139
6.3 Corner Architecture SBD	140
6.4 Conclusions of this Work	140
REFERENCES	141

LIST OF TABLES

Table 1.1	Some Properties of Single Crystal Diamond [2, 3]	2
Table 1.2	Figures of Merit for Various Semiconductors	5
Table 2.1	$N_A - N_D$ data reported in Chrenko [83] compared to the 8×10^{17} relationship derived from Collins and Williams [81]. The data in the third (I_{2800}) and fourth ($N_A - N_D$ [ppm]) columns are given exactly as presented in a table in [83]. The second column ($N_A - N_D$ [cm^{-3}]) is calculated using Equation (2.10). For comparison, if the I_{2800} values as given in [83] had been multiplied by the 8×10^{17} calibration from Collins and Williams, the values in the fifth column (8×10^{17} cal.) would have been obtained for these samples instead.	76
Table 3.1	Deposition characteristics for samples 151-154, grown in DS1.	91
Table 3.2	Characterization results for the samples of Table 3.1	92
Table 3.3	Effect of Carbon Dioxide in the Plasma Feedgas * - 0 diborane flow in the feedgas - doping in sample is due to residual boron in reactor from previous runs † - Grown thickness below measureable threshold ‡ - 2800 cm^{-1} peak below resolution limits. Upper bound of uncompensated acceptor concentration estimated based on maximum concentration possible for grown film thickness	93
Table 3.4	Deposition characteristics for the electrically characterized samples. All samples grown in DS1. * 0 - diborane flow in the feedgas, doping in sample is due to residual boron in reactor from previous runs . . .	96
Table 3.5	Electrical characterization results for the samples of Table 3.4 * - Acid cleaned, but not oxygen plasma treated prior to measurement	99
Table 3.6	Growth conditions for the lightly boron doped process optimization experiments performed on the new low boron doping diamond deposition system	102
Table 4.1	Effect of Substrate Temperature During Growth	108
Table 4.2	Effect of Total Plasma Feedgas Flow Rate	120

LIST OF FIGURES

Figure 1.1	Energy band diagrams of a p-type semiconductor SBD (a) in thermal equilibrium (b) under forward bias (c) under reverse bias. <i>Adapted from [10]</i>	7
Figure 1.2	(a) Ideal I - V characteristics for a power rectifier. The device has zero on-voltage, zero leakage-current in the off-state and takes zero time to switch between the on- and off-states. (b) The I - V characteristics of a typical power rectifier, showing a finite on-state voltage and off-state leakage current, and a breakdown voltage (BV) at a high reverse bias voltage. <i>Adapted from [9]</i>	8
Figure 1.3	(a) Diagram of a planar architecture SBD (b) Diagram of a pseudo-vertical architecture SBD (c) Diagram of a vertical architecture SBD. For interpretation of the references to color in this and all other figures, the reader is referred to the electronic version of this thesis.	10
Figure 1.4	Diamond unit cell <i>via Wikimedia Commons</i>	11
Figure 1.5	Examples of crystallographic planes and Miller indices in a cubic structure. <i>via Wikimedia Commons</i>	12
Figure 1.6	Hard sphere model depicting the appearance of the (100) and (111) crystal planes in a diamond lattice, with reference marks for the calculation of atomic density.	13
Figure 1.7	Illustration of the surface coordination number for the (111) and (100) planes. The surface layer of atoms is shown in blue, with the second layer, immediately below in the crystal structure, in gray. The atoms in the second layer that are bonded to the central top layer atom are shown in orange. There are two atoms bonded to the surface atom in the (100) plane, and three in the (111) plane.	14
Figure 1.8	Schematic drawing showing an edge dislocation. <i>via Wikimedia Commons</i>	15
Figure 1.9	Schematic drawing showing a screw dislocation. <i>via Wikimedia Commons</i>	16
Figure 1.10	Electrically active holes from the 0.37 eV deep boron acceptor as a function of temperature, shown for 1% and 10% compensation . . .	17

Figure 1.11	Electrically active electrons from the 0.58 eV deep phosphorus donor as a function of temperature, shown for 1% and 10% compensation .	18
Figure 1.12	(a) Schematic of the tapered piston belt apparatus (b) Photo of the pieces of the HPHT assembly. <i>Reproduced from</i> Bovenkerk <i>et al.</i> 1959 [19]	19
Figure 1.13	Schematic illustration of the reactor used by Angus’s group <i>Reproduced from</i> [22]	21
Figure 1.14	Schematic illustration of the hot filament reactor developed at NIRIM <i>Reproduced from</i> [29]	24
Figure 1.15	Schematic illustration of the microwave plasma reactor developed at NIRIM. <i>Reproduced from</i> Saito <i>et al.</i> 1986 [31]	25
Figure 1.16	Schematic illustration of the ASTeX-type microwave plasma CVD reactor. <i>Adapted from</i> [33].	27
Figure 1.17	Schematic illustration of the first generation MSU MCPR CVD reactor. <i>Adapted from</i> [45].	29
Figure 1.18	Schematic illustration of the second generation MSU MCPR CVD reactor. <i>Adapted from</i> [45].	31
Figure 1.19	Schematic illustration of the third generation MSU MCPR CVD reactor. <i>Adapted from</i> [45].	32
Figure 1.20	Schematic illustration of the modified high pressure MCPR CVD reactor. <i>Adapted from</i> [49, 48].	33
Figure 1.21	Example of pyramidal hillock type defects	35
Figure 1.22	Example of flat topped hillock type defects	36
Figure 1.23	Example of unepitaxial crystallite type defects	37
Figure 1.24	X-ray topography image, showing threading dislocations in two generations of diamond growth. <i>Reproduced from</i> Friel <i>et al.</i> [54]	38
Figure 2.1	Schematic illustration of the current configuration of the gas flow path in DS1	47
Figure 2.2	Schematic illustration of the gas flow path designed for DS6	50

Figure 2.3	(a) Photo of the DS6 gas line connection ventilation box, with the front door closed (b) Photo of the DS6 gas line connection ventilation box, with the front door open, showing the mass flow controllers and isolation valves inside.	51
Figure 2.4	DS6 Gas Bottle Rack	52
Figure 2.5	DS6 Throttle Valve	53
Figure 2.6	DS6 Turbo Pump	54
Figure 2.7	Schematic illustration of the microwave power supply and waveguide/transmission system designed for DS6	56
Figure 2.8	DS6 Quartz Dome	57
Figure 2.9	Schematic illustration of the cooling system designed for DS6	58
Figure 2.10	This photograph, taken looking down the back of the Neslab HX300, shows the location of the reset button, circled in red, that will clear the interlock that is triggered if the heat exchanger is run without sufficient water pressure from the house water line.	60
Figure 2.11	Input connections of the cooling system designed for DS6	61
Figure 2.12	Output connections of the cooling system designed for DS6	62
Figure 2.13	DS6 Water Cooled Stage	63
Figure 2.14	DS6 Quartz Tube	64
Figure 2.15	DS6 Molybdenum 4 inch Sample Holder	64
Figure 2.16	Illustration of the total transmission percentage through diamond, with an index of refraction $n = 2.38$, in air with $n = 1$	67
Figure 2.17	Fourier transformed infrared transmission spectrum of doped diamond films on HPHT substrates. The top sample is an HPHT substrate prior to boron doped diamond deposition, the remaining samples were deposited in DS1, with the following B/C concentrations in the plasma feedgas: SND03 - 2.5 ppm, SND09 - 12.5 ppm, SND11 - 500 ppm, and SND30 - 2000 ppm. The deposition conditions for these samples are discussed in greater detail in Chapters 3 and 4.	68

Figure 2.18	Collins and Williams [81] studied the integrated area under the 2800 cm ⁻¹ absorption feature (I_{2800}) and hall effect data to determine the vacant acceptor concentrations in natural type IIb diamonds. The sample numbers given in that work are shown next to the relevant data points. A linear fit to this data, as shown on this plot, gives $N_A - N_D = 8 \times 10^{17}(I_{2800})$	70
Figure 2.19	Baseline calculation for the determination of the integrated area of the 2800 cm ⁻¹ feature. (a) the baseline drawn on the transmission spectrum of sample SND03 (b) the resulting absorption coefficient vs. energy plot obtained using Equation (2.3)	72
Figure 2.20	An estimate of the thickness dependent lower limit resolvable for measuring the integrated area I_{2800} in Equation (2.3)	73
Figure 2.21	The $N_A - N_D$ [cm ⁻³] and I_{2800} data from Table 2.1 has been modified by multiplying the reported I_{2800} data by 10 ⁻² for all of the samples, and not just sample 52, as discussed in the text. The extrapolated calibration curve line of $N_A - N_D = 8 \times 10^{17}(I_{2800})$ and the samples from Collins and Williams [81] are also shown for reference.	77
Figure 2.22	Diagram of a standard four point probe setup. <i>Adapted from</i> [89]	83
Figure 2.23	Exposure to a hydrogen plasma results in a high contact angle, like the 80.5° shown here for sample SND04	86
Figure 2.24	Exposure to an oxygen plasma results in a low contact angle, like the 12.7° shown here for sample SND05	86
Figure 2.25	The effect of acid cleaning steps on the contact angle and conductivity of sample SND09	87
Figure 2.26	The contact angle of an oxygen terminated sample, such as for SND02 shown here, increases significantly over a period of days, indicating the O-termination is slowly lost.	88
Figure 3.1	Reflection mode optical micrographs of SND03, SND04, and SND05, samples grown at 160 Torr and ≤ 1% CO ₂	94
Figure 3.2	Reflection mode optical micrographs of SND07, and SND08, samples grown at 75 Torr and 3.5% CO ₂	94
Figure 3.3	Reflection mode optical micrographs of SND10, and SND17, samples grown at 160 Torr and 3.5% CO ₂	95

Figure 3.4	SIMS data from Sample 174	97
Figure 3.5	Temperature dependent conductivity data for SND04 (blue), shown with the curve from the fit used to determine E_A (red)	98
Figure 3.6	Activation energies from this work, shown with other values reported in the literature [99, 100] and the model of Bardeen and Pearson [101], following the method of [102], to guide the eye.	100
Figure 3.7	Optical micrograph of SND02, which has asymmetrically distributed defects. The FTIR spectrum when only Side 1 is exposed gives a lower estimate of the uncompensated acceptor concentration than the more defect-dense Side 2 (see text). Sample has dimensions: 3.5 mm 3.5 mm	101
Figure 3.8	Transmission (a) and absorption coefficient (b) spectra for two half aperture orientations of SND02, showing the difference in the measured boron concentration based on the distribution of defects	102
Figure 3.9	Optical micrographs taken at $2.5\times$ magnification in reflection mode, showing the surface morphology of Samples LB01 and LB02. These samples were grown with substrate temperatures of 870 to 920 °C in DS6, and showed many pyramidal hillock defects	103
Figure 3.10	Optical micrographs taken at $2.5\times$ magnification in reflection mode, showing the surface morphology of samples LB03, LB04, and LB05, grown in DS6. These samples were grown with substrate temperatures of 790 to 809 °C, and have almost no pyramidal hillock defects . . .	104
Figure 3.11	Optical micrograph taken at $2.5\times$ magnification in reflection mode, showing the surface morphology of sample 156_1, grown in DS6. The optimized process resulted in a very smooth, low defect surface. . .	105
Figure 4.1	Optical micrographs, taken in reflection mode, showing the defect morphologies of samples grown with $[B]/[C] = 666$ ppm in the plasma gas phase at three different substrate growth temperatures: (a) 850 °C, (b) 950 °C, (c) 1050 °C	107
Figure 4.2	Optical micrographs, taken in reflection mode, showing the defect morphologies samples grown at 850 °C (top row) and 950 °C (bottom row). The $[B]/[C]$ ratio in the plasma feedgas for each sample is given in the column headings. For comparison, the morphologies of samples grown at 666 ppm were shown in Figure 4.1. The scale bar for all images, in the lower left of the sample grown at 850 °C and 933 ppm, is 500 μm	111

Figure 4.3	Examples of the appearances of samples of this work, shown left to right: an as received type Ib HPHT seed, sample SND22 and sample SND29	112
Figure 4.4	[B]/[C] ratio in the plasma gas phase vs. incorporated electrically active [B] in the grown diamond sample. This figure illustrates graphically the doping efficiency. Samples grown at 950 °C are shown with blue circles, samples grown at 850 °C are shown with green squares, and for comparison, samples from the work of Achard <i>et al.</i> [55] measured in that reference by FTIR using the same relationship of Equation (2.14) and confirmed by SIMS, are shown as red triangles.	113
Figure 4.5	The data from Figure 4.4 is reoriented by dividing the plasma feedgas [B]/[C] ratio by the growth rate. The samples of this investigation are divided by their individual growth rates, which are given in Table 4.1, and for comparison the samples of Achard <i>et al.</i> [55] are included as well, using the 10 $\mu\text{m h}^{-1}$ growth rate given in that reference. A legend is given in the top left of the plot area.	116
Figure 4.6	[B]/[C] ratio in the plasma gas phase vs. boron concentration in the grown diamond sample measured by SIMS (Evans Analytical Group, www.eaglabs.com). Samples grown at 950 °C are shown with blue circles, samples grown at 850 °C are shown with green squares. . . .	117
Figure 4.7	Depth profile of SIMS measurements showing uniformity of doping profile through the sample depth. The SIMS artifact of sample SND26 is due to the high boron concentration in the grown layer on top. . .	119
Figure 4.8	Reflection mode optical micrographs of samples grown with a low purity bell jar, with total flow rates of: (a) 200 sccm, (b) 400 sccm, (c) 800 sccm	120
Figure 4.9	Reflection mode optical micrographs of samples grown with high quality bell jar, with total flow rates of: (a) 200 sccm, (b) 400 sccm, (c) 800 sccm	121
Figure 5.1	The growth steps for the fabrication of a corner architecture SBD: 1. Heavily boron doped diamond is deposited on a type Ib HPHT seed. 2. The sample is then laser-cut lengthwise and both sides of a resulting slab are polished. 3. Lightly boron-doped diamond is grown perpendicular to the direction of the previous CVD growth. 4. Schottky and ohmic contacts are deposited to form a vertically oriented SBD structure	125

Figure 5.2	Reflection mode optical micrographs showing the actualization of the fabrication process shown in Figure 5.1: 1. Sample SND34, as described in Chapter 4, will be used for the heavily boron doped diamond on an HPHT seed. 2. A slab cut from the side of SND34 after laser cutting and polishing. This image was taken in the direction normal to the cut plane. 3. Lightly boron-doped diamond is grown perpendicular to the direction of the previous CVD growth, on top of the slab cut from sample SND34. The same optimized low boron doped growth process is used as was used for sample 156_1, which was described in Chapter 3. 4. Au Schottky and Ti/Au ohmic contacts are deposited to form a corner architecture diode structure.	126
Figure 5.3	Diagram of a Corner-architecture SBD	126
Figure 5.4	Example of the determination of the breakdown voltage of one of the SBDs. The leakage current is characterized from 0 V to 100 V with the Keithley 236. The reverse current is then checked by the voltage drop across a 1 M Ω resistor until a current above 1 μ A is reached. . .	129
Figure 5.5	The breakdown voltage of the individual diodes, shown by superimposing a color coded circle marked with the breakdown voltage in [V] onto the location of each Schottky contact. The underlying image is the optical micrograph of the Schottky contacts from Figure 5.2. Those diodes marked with an \otimes were shorted to the backside contact along the sample sides, and did not show diode behavior.	130
Figure 5.6	Several of the 64 working SBD contacts are numbered for reference in the text. The location of the heavily doped p^+ -layer is indicated, along the top surface. The underlying image is the optical micrograph of the Schottky contacts from Figure 5.2.	131
Figure 5.7	The $I - V$ characteristics of diodes numbered 7 and 12-15, which are enclosed in the red box in Figure 5.6. The on-state resistance, R_{ON} , shown next to the diode number, is calculated at 5 V.	132
Figure 5.8	Example of the determination of the Schottky-barrier height ϕ_B , and ideality factor n by linear fitting to the diode curve of diode 10 (shown in Figure 5.6), at room temperature. The rectification ratio of 1.6×10^9 at $ 8 \text{ V} $ is also determined from this plot.	133
Figure 5.9	The temperature dependent forward characteristics of diode 10 from Figure 5.6 is shown. The current increases with increasing temperature, and the on-state resistance decreases. High forward currents in the mA range, up to above the Keithley 236 limit of 100 mA are achieved.	134

Figure 5.10 The ideality factors n and Schottky-barrier heights, ϕ_B , fitted from the temperature varied series of diode measurements shown in Figure 5.9. The trend of the Schottky-barrier height increasing and the ideality factor initially decreasing, and then subsequently slightly increasing with increasing temperature is noted by the green arrows. 136

Chapter 1

Background and Motivation

This chapter will describe the motivation for this dissertation work, and present background information on the growth and applications of single crystal boron doped diamond. Some of the current challenges in this field will be reviewed, and the potential benefits of overcoming these challenges to realize commercially available diamond electronics for high power and high temperature devices will be presented. Section 1.1 will introduce and present the objectives of this work. Section 1.2 will describe the benefits of developing diamond for high power applications. Section 1.3 will describe the Schottky Barrier Diode (SBD), an application for which Boron Doped Diamond (BDD) has significant potential. Section 1.4 will describe the structure of the diamond crystal. Section 1.5 describes the electronic structure of diamond. Section 1.6 gives an overview of the Chemical Vapor Deposition (CVD) process, including the historical development of the process and several significant reactor designs. Section 1.7 will describe the challenges in diamond growth that currently limit the realization of BDD SBDs. Section 1.8 will describe the source of surface conductivity on a diamond surface.

1.1 Introduction

Diamond is well known for its beauty in jewelry, and for its exceptional mechanical properties, like its superior hardness. It is less commonly known that diamond also has a number of other outstanding properties, like a large bandgap, and the highest thermal conductivity of any material [1]. Several of these outstanding properties are given in Table 1.1

Property	Approximate Value (at 300K)
Thermal conductivity	21.9 W cm ⁻¹ K ⁻¹
Band gap	5.47 eV
Carrier mobility (electron, Hall effect)	660 cm V ⁻² s ⁻¹
Carrier mobility (hole, Hall effect)	1650 cm V ⁻² s ⁻¹
Dielectric constant	5.7
Breakdown electric field strength	10-20 MV cm ⁻¹
Intrinsic resistivity	1 × 10 ¹³ Ω cm
Mechanical hardness	90 GPa
Sound propagation velocity	17.5 km s ⁻¹

Table 1.1 Some Properties of Single Crystal Diamond [2, 3]

These properties suggest an enormous untapped potential as an electronic material [4]. Diamond devices have the potential to revolutionize high power and high temperature electronics in diverse fields such as power distribution, manufacturing, and alternative energy production. Because of its exceptional electronic and physical properties, diamond electronic devices may one day be able to operate without cooling at extreme temperatures and without requiring the kind of circuit protection that modern silicon-based technologies must implement. Progress toward the realization of these high-power, high-frequency, mechanically- and thermally-robust electronic devices is the goal of the work presented in this dissertation.

The research described in this dissertation is concerned with improving the state of the art in Microwave Plasma Assisted Chemical Vapor Deposition (MPACVD) of BDD. Of key importance in this field is developing the ability to reliably produce both heavily doped and

lightly doped layers of controlled doping concentration and thickness, which will allow the reliable production of BDD vertical architecture SBDs. The research described here has several objectives:

1. To control the doping concentration of lightly boron doped diamond by reducing the boron concentration in grown films.
2. To improve the doping efficiency at high boron doping levels.
3. To identify regimes for high quality diamond growth that minimize the number of defects that form at both high and low doping levels.
4. To fabricate and characterize a SBD utilizing these optimized regimes, with an architecture designed to improve the diode characteristics of diamond devices.

1.2 Material Evaluation for Extreme Electrical Applications

The selection of a material for devices with high power capabilities requires the consideration of a number of material properties that affect device performance under extreme conditions.

Johnson [5] has shown that the product of the breakdown electric field, E_B , and the maximum carrier drift velocity, v_s , sets the limit of various transistor parameters for devices made of a specified material. The result is the Johnson figure of merit (*JFOM*), given in Equation (1.1).

$$JFOM = \frac{E_B v_s}{2\pi} \quad (1.1)$$

The charge carrier transit time cut-off frequency in a transistor is defined by $f_{\text{transit}} = 1/(2\pi\tau_{\text{avg}})$, where τ_{avg} is the average time it takes a charge carrier moving at an average velocity v_{avg} to travel the emitter-to-collector distance L . τ_{avg} is maximized at maximum v_{avg} , which is set for a given material by v_s . τ_{avg} can be further reduced for carriers traveling at v_s by reducing L . There is a lower limit on L that is reached when the applied electric field exceeds the breakdown electric field, given by $V_{\text{EC}}/L \geq E_B$, where V_{EC} is the emitter-to-collector voltage. The *JFOM* therefore illustrates that for a given device cut-off frequency, there is a trade-off in the maximum allowable voltage in a charge controlled device such as a transistor.

In 1972, Keyes [6] developed a figure of merit to analyze a material's thermal limitation on switching in integrated circuits. The delay through a semiconductor device is related to the thickness of the device and an *RC* time constant, which leads to the conclusion that the smaller the device, the faster it can operate. However, Keyes points out that there is a lower limit on the size, since there is a relatively size-independent amount of power that must be conducted away from the device as heat. As the device size decreases, the thermal resistance increases, which causes the device temperature to increase as well. This means that, in general, a material with a high thermal conductivity will allow for smaller feature sizes. The material properties that govern the minimum thickness limitation therefore also limit the possible speed of devices out of a given material, which leads to the Keyes figure of merit, given in Equation (1.2), where c is the velocity of light, ϵ is the dielectric constant of the semiconductor, and λ is the thermal conductivity.

$$KFOM = \lambda \left[\frac{c v_s}{4\pi\epsilon} \right]^{\frac{1}{2}} \quad (1.2)$$

A third figure of merit was developed by Baliga [7] for evaluating the operating losses of field-effect transistors in high power applications. The Baliga figure of merit (*BFOM*) is given in Equation (1.3), where μ is the mobility, and E_G is the bandgap of the semiconductor. The *BFOM* is based upon the assumption that ohmic losses are the dominant source of power dissipation, which holds for low frequency applications.

$$BFOM = \epsilon \mu E_G^3 \quad (1.3)$$

Table 1.2, adapted from Lebedev and Chelnokov [8], shows these three figures of merit for various semiconductors as a ratio to silicon. It is clear from these figures that diamond is the superior semiconducting material for high temperature, high frequency, and high power operation. Although diamond is clearly a material well suited to these extreme applications, there are some complications that have remained as obstacles to its introduction as a commercial material. With increased understanding of the growth process, boron doped SCD has the potential to revolutionize high power devices, and open the field to a range of applications impossible for silicon devices.

Material	JFOM	KFOM	BFOM
Si	1	1.00	1
GaAs	11	0.45	28
GaP	37	0.73	16
6H-SiC	260	5.10	90
4H-SiC	410	5.10	290
GaN	790	1.80	910
Diamond	5330	31.00	14860

Table 1.2 Figures of Merit for Various Semiconductors

1.3 Principles of Diamond Schottky Barrier Design

The excellent fast switching capabilities and relatively low on-state voltage drop of the SBD have made it an attractive device for power electronics applications, where silicon devices are now widely used in power supply circuits with low operating voltages. For higher operating voltage systems, the use of silicon devices may not be possible, and commercially available devices are generally rated with breakdown voltages of less than 100 V [9]. In this section, the principles of diamond SBDs will be reviewed. Section 1.3.1 will describe the physics of the SBD, and Section 1.3.2 will describe the vertical architecture diamond SBD, comparing this architecture to other possible diamond SBD diode designs.

1.3.1 Schottky Barrier Diode Background and Theory

The Schottky barrier forms a rectifying contact, where a forward bias causes the forward current to increase as the potential barrier $q(\psi_{bi} - V_F)$ decreases, and the current due to a reverse bias becomes negligible as the barrier height, $q(\psi_{bi} + V_R)$ increases, as shown in Figure 1.1. In the case of a p -type semiconductor, the forward bias is defined with the semiconductor biased positively with respect to the metal.

Because the Schottky barrier only allows current flow in the forward direction, the Schottky barrier forms a diode. The SBD has distinct advantages for certain applications over the conventional p - n diode. One significant advantage is due to the fact that the current is due to majority- (rather than minority-) carrier injection. As such, minority-carrier effects such as storage delay times are minimized, making SBDs ideal for high-frequency (fast switching) devices.

For high power applications, the SBD should be as close to an ideal power device as

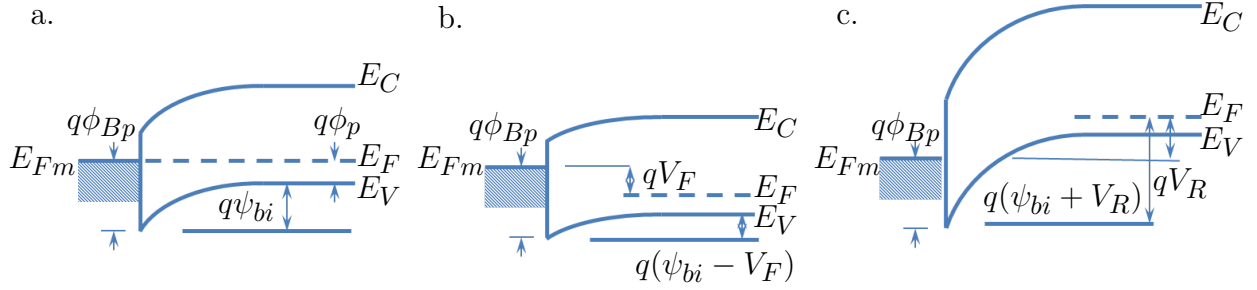


Figure 1.1 Energy band diagrams of a p-type semiconductor SBD (a) in thermal equilibrium (b) under forward bias (c) under reverse bias. *Adapted from [10]*

possible. An ideal power device would be one in which the flow of power to loads is controlled, with zero power dissipation [9]. The ideal and nonideal I - V characteristics of a power rectifier device are shown in Figure 1.2. Ideally, a power switch would operate with the I - V characteristics shown in Figure 1.2(a). Actual power devices, however, have finite on-state voltages and off-state leakage currents, as shown in Figure 1.2(b). The on-state voltage drop, V_{ON} , leads to so-called conduction power losses. The finite leakage current, I_{OFF} , leads to off-state power losses. At a significant reverse bias, the SBD is no longer able to withhold the reverse current. This bias is therefore called the breakdown voltage (BV) in Figure 1.2(b). For high power devices, it is essential that this breakdown voltage be as large as possible.

The breakdown voltage is limited by the onset of avalanche breakdown, which occurs through the process of impact ionization. Impact ionization occurs when an electron or hole traveling through the depletion region in a reverse biased device has enough energy that a collision with an electron in the valence band can excite it up to the conduction band, creating a new electron-hole pair. Avalanche breakdown occurs when the electric fields in the depletion region are so large that these newly generated carriers also become energetic enough to create new electron-hole pairs, and the number of carriers in the depletion region increases rapidly, which then creates a significant reverse current.

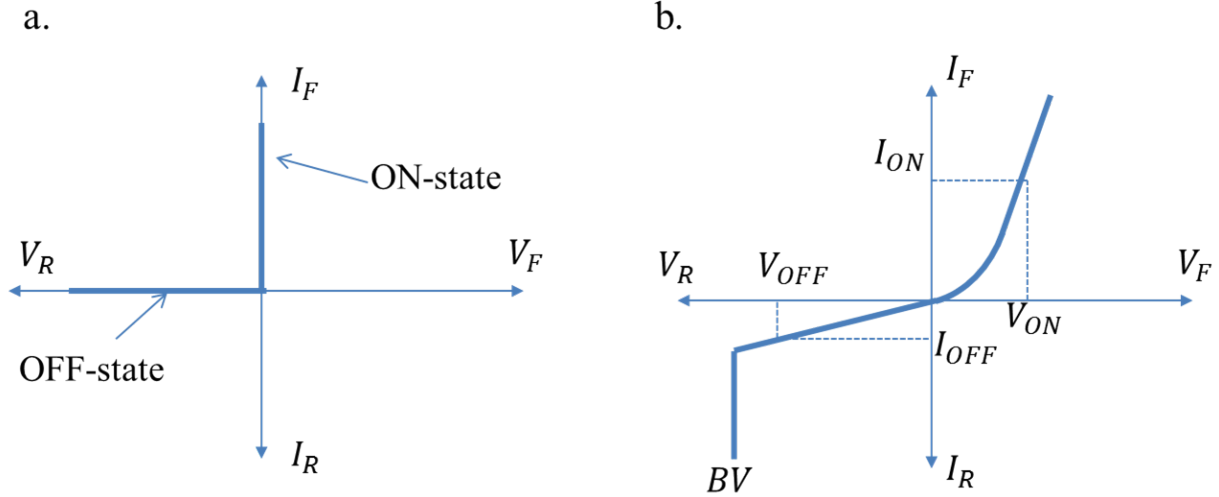


Figure 1.2 (a) Ideal I - V characteristics for a power rectifier. The device has zero on-voltage, zero leakage-current in the off-state and takes zero time to switch between the on- and off-states. (b) The I - V characteristics of a typical power rectifier, showing a finite on-state voltage and off-state leakage current, and a breakdown voltage (BV) at a high reverse bias voltage. *Adapted from [9]*

1.3.2 Vertical Schottky Barrier Diodes

Several SBD designs have been demonstrated in the literature. These designs fall into three broad categories: lateral, pseudo-vertical, and vertical. The most basic design is a lateral structure, where the ohmic and Schottky contacts are both deposited on the top surface of the diamond substrate [11]. An example of a planar SBD design is shown in Figure 1.3(a). The current in a planar diode travels primarily in the horizontal direction of the device, which causes a non-uniform current density, especially at the contact edges, that leads to a lower breakdown voltages due to the non-uniformity of the current. Additionally, although the formation of a Schottky contact to the p^- -layer can be achieved, a high quality ohmic contact is nearly impossible without a more heavily doped p^+ -layer, and the non-ideality of the ohmic contact further increases the R_{ON} of the device. However, this design is preferable for many applications because of its ease of fabrication, since no removal of the growth substrate or

additional diamond layers grown on top of the diamond substrate are required. This design is often preferred for the electrical characterization of a diamond film, or for a comparison of several types of contacts.

In order to improve the quality of the ohmic contact from the planar architecture, the pseudo-vertical structure, shown in Figure 1.3(b) can be used. In this structure, the ohmic contact is formed on p^+ -diamond and the Schottky contacts are deposited on p^- -diamond. As in the lateral structure, the current still must travel primarily in the horizontal direction, which again causes non-uniform current densities, which lead to lower breakdown voltages. The current travels primarily through the p^+ -layer however, which reduces the R_{ON} compared to planar diodes.

In a vertical device, as shown in Figure 1.3(c), the ohmic contact is deposited on p^+ -diamond while the Schottky contact is on p^- -diamond, and the current flows in a vertical direction. For high power applications, the vertical orientation would lead to significantly higher breakdown voltages than the planar configuration, due to the uniform current densities caused by the current moving in the vertical direction directly from one contact to the other. The vertical path in a well-designed vertical diode is also shorter than the path length that would be possible in a planar structure, leading to a significant reduction in R_{ON} , and therefore also in the power losses. The fabrication of a vertical architecture SBD is significantly more complicated than a planar structure however, due to the freestanding p^+ -layer of diamond. The p^+ - and p^- -layers must both be grown to controlled thicknesses, with well controlled and repeatable doping concentrations. Additionally, to allow contact deposition on the bottom surface, the HPHT seed, which is insulating, needs to be removed from the bottom of the structure after growth, which requires laser cutting and polishing, and therefore a p^+ -layer that is thick enough to be freestanding. The p^+ -layer must also

have a very high doping concentration, in order to keep R_{ON} as low as possible. As a result, a growth process that will consistently produce high quality, thick, heavily boron doped diamond is a necessary precondition for high breakdown voltage vertical SBDs.

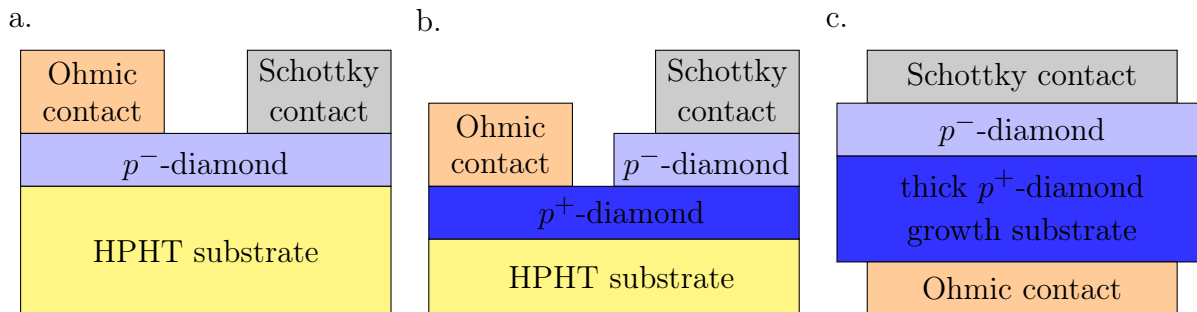


Figure 1.3 (a) Diagram of a planar architecture SBD (b) Diagram of a pseudo-vertical architecture SBD (c) Diagram of a vertical architecture SBD. For interpretation of the references to color in this and all other figures, the reader is referred to the electronic version of this thesis.

1.4 Chemical Structure of Diamond

This section will describe the atomic arrangement in the diamond crystal. Section 1.4.1 will describe the arrangement of atoms in a perfect diamond crystal, and Section 1.4.2 will describe dislocations that can disturb that arrangement in real diamond material.

1.4.1 Crystal Structure

A crystal is characterized by a symmetric, well-structured periodic placement of its molecular components. The crystalline structure can be represented by the repetition of a unit cell, which has a side length of lattice constant a . In diamond, the unit cell is composed to two interpenetrating face-centered cubic (f.c.c.) lattices, with the second offset from the first by $[1/4, 1/4, 1/4]$, as shown in Figure 1.4.

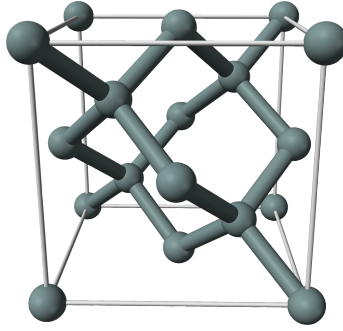


Figure 1.4 Diamond unit cell *via Wikimedia Commons*

In crystalline materials it is often convenient to refer to the planes of atoms within the crystalline structure. The convention in crystallography is to describe these planes by the intercepts they make with the crystal axes of the unit cell. The inverse of the fractions that represent the intercepts are known as the Miller Indices of the planes. In this dissertation work the (100) and (111) planes have particular significance. These, and several other example crystallographic plane orientations are shown in Figure 1.5.

The (111) and (100) principal planes have different atomic and bond densities, which results in differences in the chemistries of the two planes. The atomic density of a plane is the number of atoms per unit area. A hard sphere representation of the atomic packing on the (111) and (100) planes is shown in Figure 1.6. The atomic orientation in the (100) plane is a square array that is coincident with one of the sides of the primitive lattice unit cell. The sides of the dashed square shown in Figure 1.6 therefore have length a , the diamond lattice constant. With a lattice constant of 3.56683 \AA , the area of the square is 12.722 \AA^2 . There are two atoms enclosed in the square, the one in the center and the four atoms at the corners which each are $1/4$ enclosed inside the square. The atomic density is therefore 0.1572 \AA^{-2} on the (100) plane.

The (111) plane has atoms arranged hexagonal close-packed, as shown in Figure 1.6.

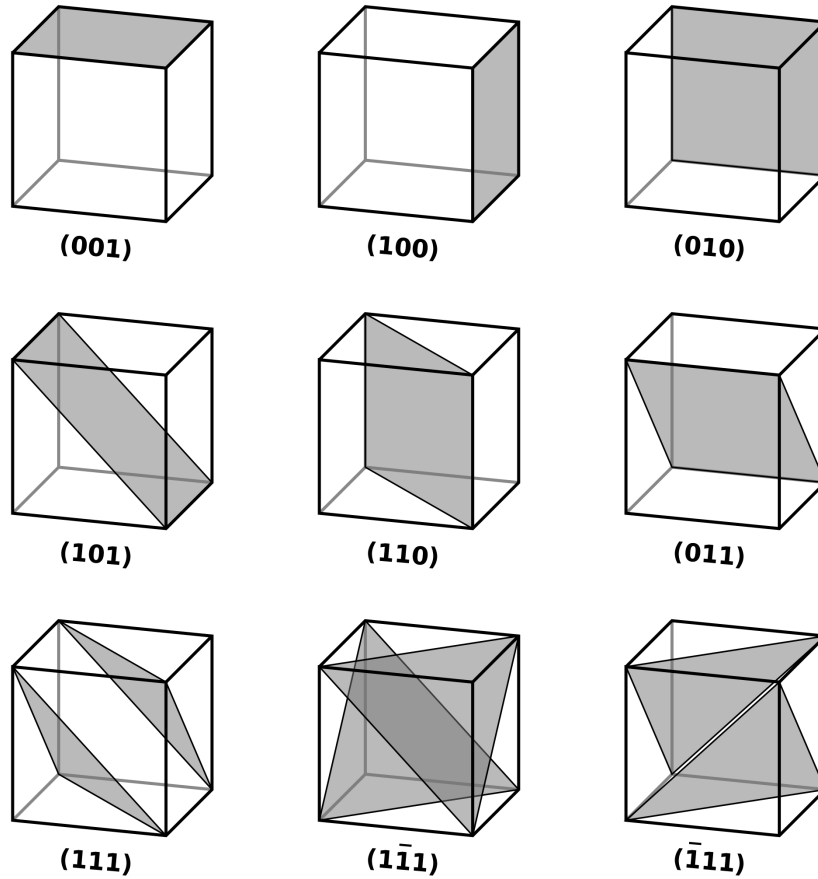


Figure 1.5 Examples of crystallographic planes and Miller indices in a cubic structure. *via Wikimedia Commons*

The (111) plane runs along the hypotenuse of the right triangle formed by two sides of the primitive unit cell. Therefore the length one of the sides of the hexagon shown in Figure 1.6, which is $1/2$ of that hypotenuse, is $\frac{a}{\sqrt{2}}$, which gives an area of 16.53 \AA^2 . There are three atoms within the hexagon: the one in the center and $1/3$, of each of the six atoms around the perimeter, which gives an atomic density of 0.1815 \AA^{-2} . The ratio of the atomic densities are therefore $100:111 = 1:1.1555$, which is true for all materials with diamond and zinc-blende crystal structures.

The coordination number of a crystal is a property which describes the number of nearest neighbors of an atom. Diamond, as shown in Figure 1.4, is tetragonally organized, and

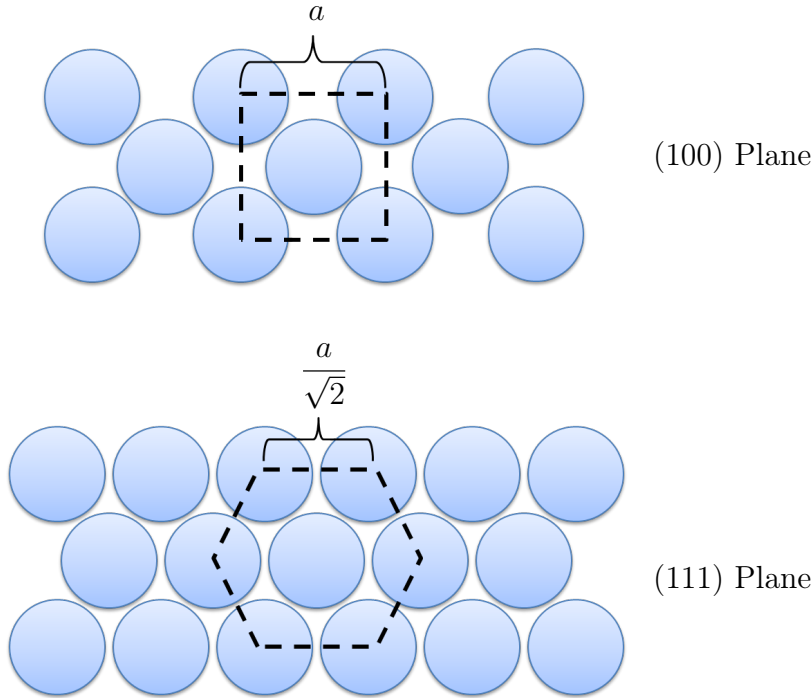


Figure 1.6 Hard sphere model depicting the appearance of the (100) and (111) crystal planes in a diamond lattice, with reference marks for the calculation of atomic density.

therefore has a coordination number of 4 for interior atoms. At the surface however, atoms have coordination numbers less than the bulk coordination number. Figure 1.7 shows a schematic representation of the top two layers of the (111) and (100) planes. In the (100) plane, the central atom of the top layer is bound to two atoms in the layer of bulk atoms below it. These atoms are shown in orange for clarity in Figure 1.7. In the (111) plane, the central top atom is bound to three atoms in the layer below it, which are also shown in orange. This means the surface coordination number of the (100) surface is 2, while for the (111) surface it is 3. This has consequences for the surface chemistry, since it means that the (100) surface has 2 dangling bonds per surface atom, whereas the (111) surface only has 1. This also means that the (100) surface has a greater density of dangling bonds than the (111) surface, with a ratio of $(100):(111) = 1:0.577$.

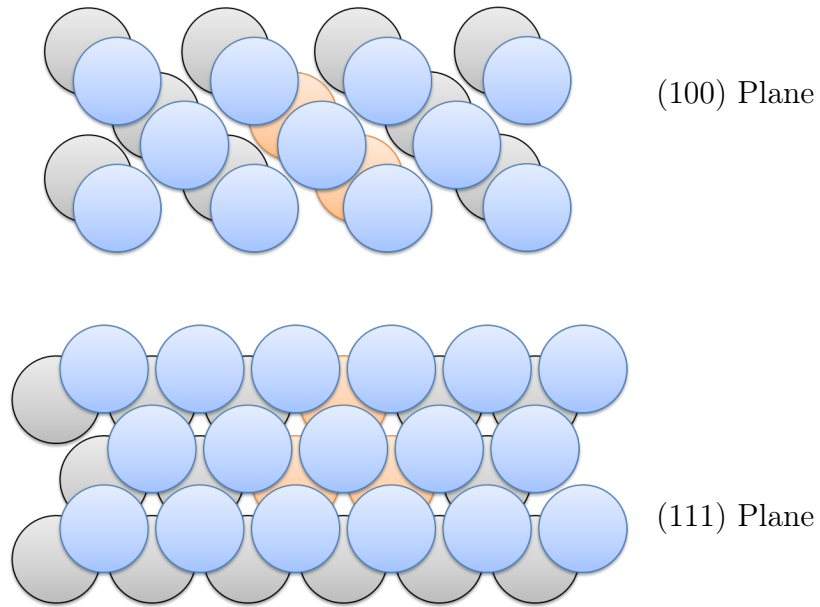


Figure 1.7 Illustration of the surface coordination number for the (111) and (100) planes. The surface layer of atoms is shown in blue, with the second layer, immediately below in the crystal structure, in gray. The atoms in the second layer that are bonded to the central top layer atom are shown in orange. There are two atoms bonded to the surface atom in the (100) plane, and three in the (111) plane.

1.4.2 Dislocations

A dislocation is a crystallographic defect where the atoms are out of the regular position in the crystal structure. In a line dislocation, a plane of atoms terminates in the middle of a crystal. The surrounding atoms bend around the line of the terminating plane, distorting the planes of atoms in the immediate vicinity of the dislocation. A dislocation has two defining properties, the line direction, which runs along the terminating plane, and the Burgers vector, which represents the magnitude and direction of the lattice distortion. There are two basic types of line dislocations, edge and screw type. So-called “mixed” dislocations types, which are a combination of both screw and edge defects, are also common.

1.4.2.1 Edge Dislocations

In an edge dislocation, the Burgers vector is perpendicular to the dislocation line direction. The result is shown schematically in Figure 1.8. The defective crystalline structure shown on the right can be imagined to be formed by altering the perfect crystalline structure on the left by moving the point labeled Q to be coincident with the point labeled M . The vector between Q and M in the perfect structure is the Burgers vector of the edge dislocation.

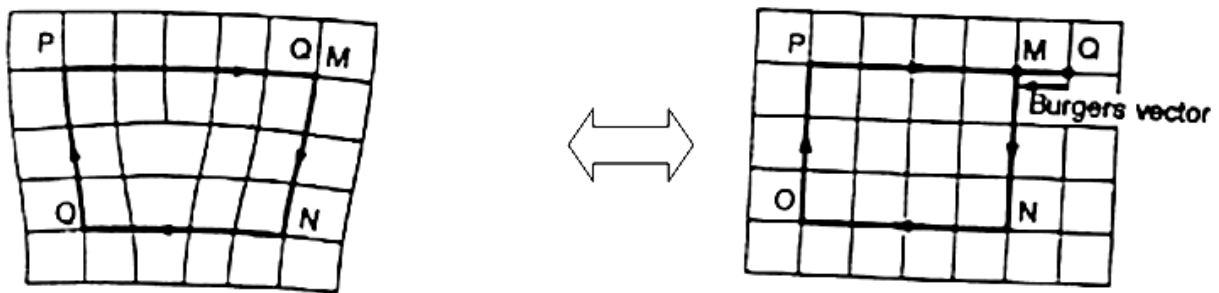


Figure 1.8 Schematic drawing showing an edge dislocation. *via Wikimedia Commons*

1.4.2.2 Screw Dislocations

In a pure screw dislocation, the Burgers vector is parallel to the dislocation line direction. The result is shown schematically in Figure 1.9. Again the defective crystalline structure shown on the right can be imagined to be formed by altering the perfect crystalline structure on the left by moving the point labeled Q to be coincident with the point labeled M . The vector between Q and M in the perfect structure is the Burgers vector of the screw dislocation.

1.4.2.3 Mixed Dislocations

In real crystalline structures the dislocation line direction and Burgers vectors are not always perfectly parallel or perpendicular. These dislocations composed of partly screw and partly edge character are known as mixed dislocations.

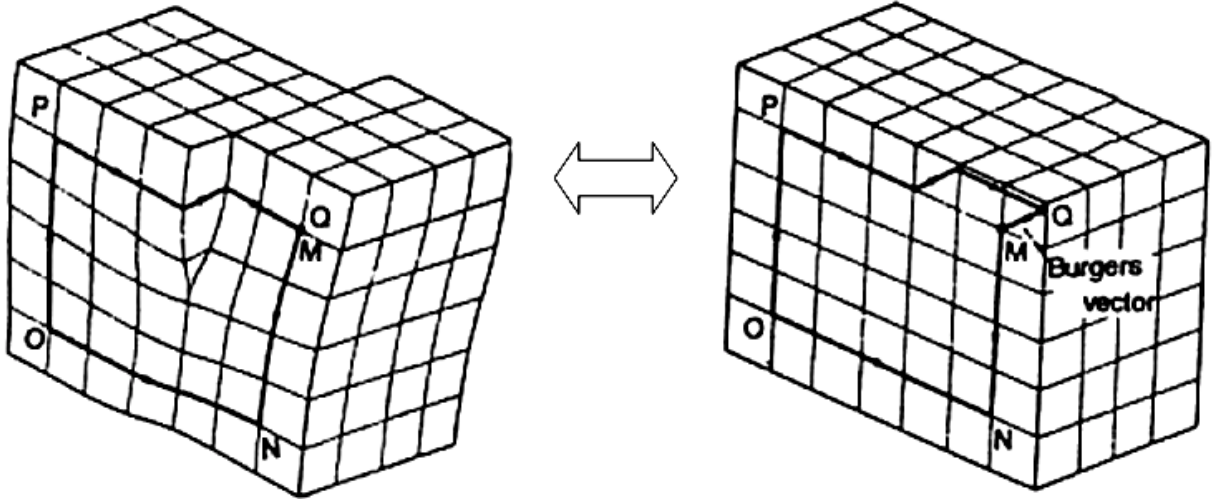


Figure 1.9 Schematic drawing showing a screw dislocation. *via Wikimedia Commons*

1.5 Electronic Structure of Diamond

Diamond has a wide bandgap (5.47 eV) [12], which makes intrinsic diamond a good insulator. Boron atoms can be substitutionally incorporated into the diamond lattice, and B-dopants cause acceptor levels at 0.37 eV above the valence band level. This would be considered an extremely deep dopant in silicon, however it is considerably more shallow than the approximately 0.5 - 0.6 eV phosphorus donor level [13, 14], or the nitrogen donor level at approximately 1.7 eV below the conduction band [15].

The deep levels of the dopants in diamond result in only a small percentage of the carriers activated at room temperature. The charge in a semiconductor is conserved, as given by the charge neutrality equation of Equation (1.4), where p , N_A^- , n , and N_D^+ are the concentrations of holes, ionized acceptor atoms, electrons and ionized donor atoms respectively.

$$p + N_D^+ = n + N_A^- \quad (1.4)$$

Equation (1.4) can be used to calculate the levels of activated holes or electrons diamond

doped to a given concentration with a given compensating donor or acceptor concentration. For diamond doped with a boron concentration of $1 \times 10^{16} \text{ cm}^{-3}$, the concentration of electrically active holes were calculated for an activation energy of 0.37 eV, as given in Figure 1.10, for compensating donor concentrations of 1% and 10%.

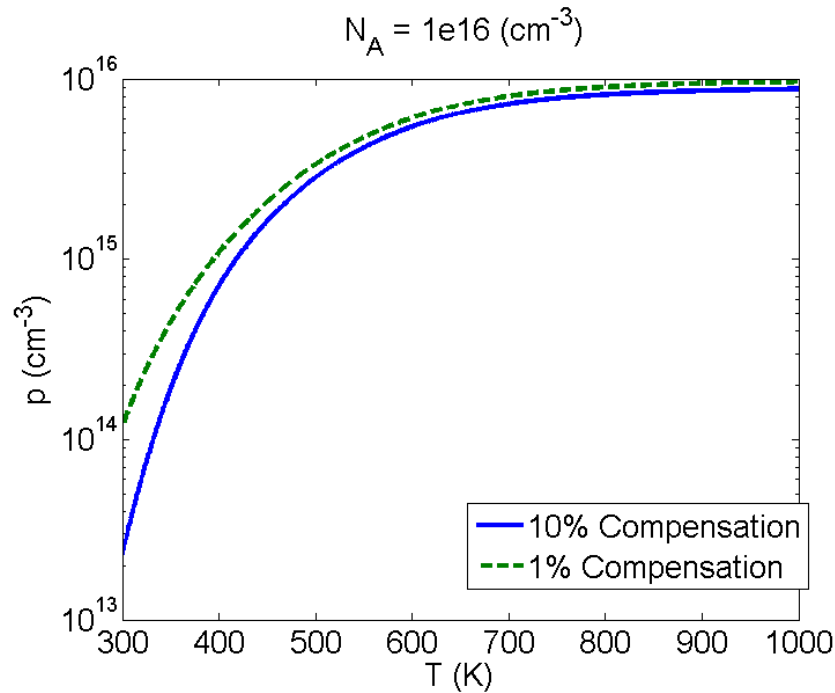


Figure 1.10 Electrically active holes from the 0.37 eV deep boron acceptor as a function of temperature, shown for 1% and 10% compensation

For diamond doped with a phosphorus concentration of $1 \times 10^{16} \text{ cm}^{-3}$, the concentration of electrically active electrons were calculated using Equation (1.4), as shown in Figure 1.11, for compensating acceptor concentrations of 1% and 10%.

1.6 Chemical Vapor Deposition of Diamond

This section will describe the method of diamond growth by Chemical Vapor Deposition (CVD). Section 1.6.1 will detail the evolution of the CVD method. The development of several

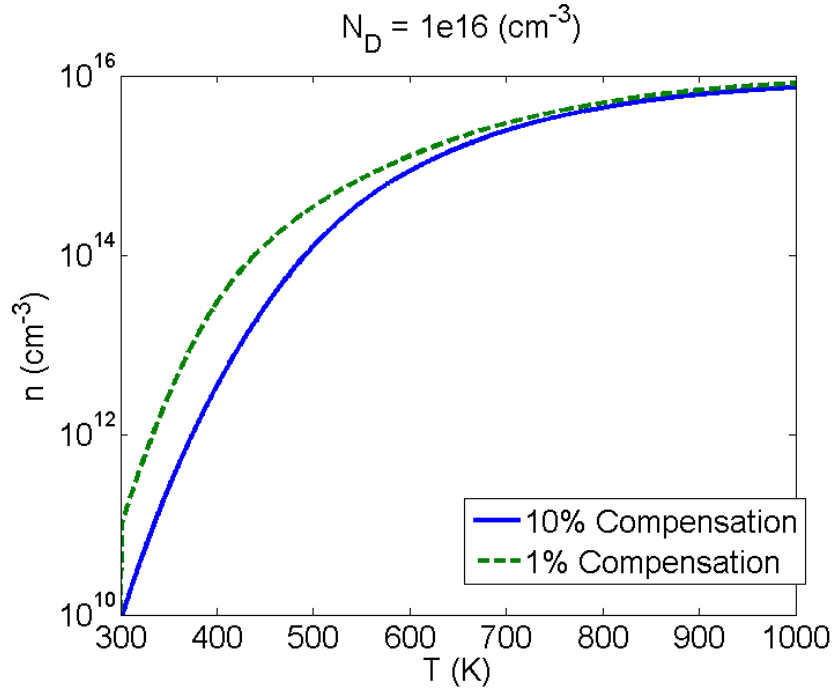


Figure 1.11 Electrically active electrons from the 0.58 eV deep phosphorus donor as a function of temperature, shown for 1% and 10% compensation

historically important reactors, including the deposition systems used in this dissertation research, will be described in Section 1.6.2.

1.6.1 The Historical Development of Chemical Vapor Deposition of Diamond

Early efforts to synthesize diamond attempted to mimic the intense heating and pressure conditions that occur where diamond crystals naturally form in the upper mantle on Earth, about 160 km below the surface. At standard ambient temperature and pressure (298 K, 100 kPa), graphite, rather than diamond, is the most thermodynamically stable form of carbon. Early failures in this field [16] often resulted in the conversion of diamond seeds into graphite, before the technological difficulties in achieving the extreme heat and pressure

required to move into the regime in which diamond is the thermodynamically stable allotrope of carbon were eventually overcome.

The first successful synthetic growth of diamond at these high pressures was reported in 1955 [17]. This diamond, referred to as the run 151 diamond, which was thought to have been the first diamond grown by the high pressure high temperature (HPHT) method, was later confirmed with modern spectrographic techniques to actually be a natural type Ia diamond that had inadvertently gotten into the run experiment [18]. Soon after, at slightly higher growth pressures on the same tapered piston belt apparatus and the same system involving carbonaceous material and molten metal, these authors did go on to demonstrate the first reproducible HPHT diamond synthesis, which they published in full details in 1959 [19] (after a US Department of Defense secrecy order had been lifted). The tapered piston apparatus used in these experiments is shown in Figure 1.12.

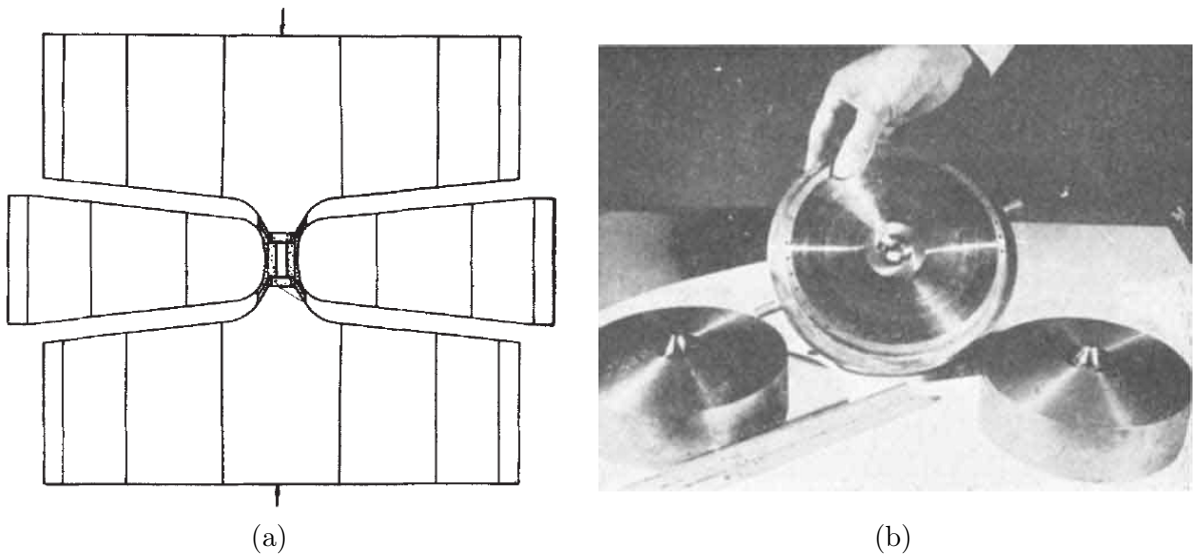


Figure 1.12 (a) Schematic of the tapered piston belt apparatus (b) Photo of the pieces of the HPHT assembly. *Reproduced from Bovenkerk et al. 1959 [19]*

Around this same time, a number of researchers in the nascent field of diamond growth reported on the possibility of exploiting kinetic factors in order to facilitate diamond growth

in a temperature-pressure regime where diamond is thermodynamically unstable with respect to graphite [20, 21]. The mobility of carbon atoms on the diamond surface was shown to be significant at 1000 °C [21], and an activation barrier limited the rate of the spontaneous transformation from diamond to graphite to an insignificant level for temperatures lower than about 1300 °C [22]. It was therefore possible that a diamond could grow epitaxially if it were placed in some environment supersaturated with carbon at temperatures in the approximate range of 1000 °C to 1300 °C.

One early claim of diamond growth in a thermodynamically metastable regime created a supersaturated carbon environment in a molten metal medium [23], an environment that closely resembled the HPHT method. Around that time it was reported that a supersaturated carbon environment could also be created by passing a carbon-containing gas over a diamond seed crystal under conditions which would permit its growth [24, 25]. These early experiments had low growth rates, and impure mixed phases resulted from graphite co-deposited with the diamond. The successful and convincing application of this gas-phase method to grow diamond material was reported for the first time in the scientific literature in 1968 [22], when John Angus's group reported that including hydrogen in the reactor feedgas would preferentially etch graphite, allowing diamond material (but not graphite) to remain on the growth surface. The growth chamber used in this report consisted of a vacuum chamber in which methane was thermally decomposed to provide the supersaturated carbon gas phase, as shown schematically in Figure 1.13. Depositions were attempted at pressures ranging from 0.15 to 458 Torr, with temperatures ranging from 980 °C to 1050 °C. The demonstration of the CVD method of diamond growth sparked considerable interest, and by the 1980s, researchers in the United States, Japan and the USSR were all preparing diamond films using CVD methods. Russian work at this time showed that the CVD technique could be used to grow

diamond heteroepitaxially, that is, on non-diamond substrates [26, 27]. Researchers at the Japanese National Institute for Research in Inorganic Materials (NIRIM) used these findings to develop first the hot filament reactor [28, 29], and then subsequently the first microwave plasma reactor [30, 31]. The hot filament reactor developed at NIRIM is shown schematically in Figure 1.14, and the microwave plasma reactor is shown schematically in Figure 1.15. These developments, which enabled high quality diamond film growth at reasonable growth rates (approximately $1 \mu\text{m h}^{-1}$), will be described in Section 1.6.2. These reactor designs are still in use in diamond growth research around the world, and their development marked the beginning of the modern era of CVD growth. This thesis is concerned with the CVD growth of doped, single crystal diamond in MSU-type reactors, which were also developed beginning in the late 1980s, and evolution of the MSU-type reactor design will also be described in Section 1.6.2.

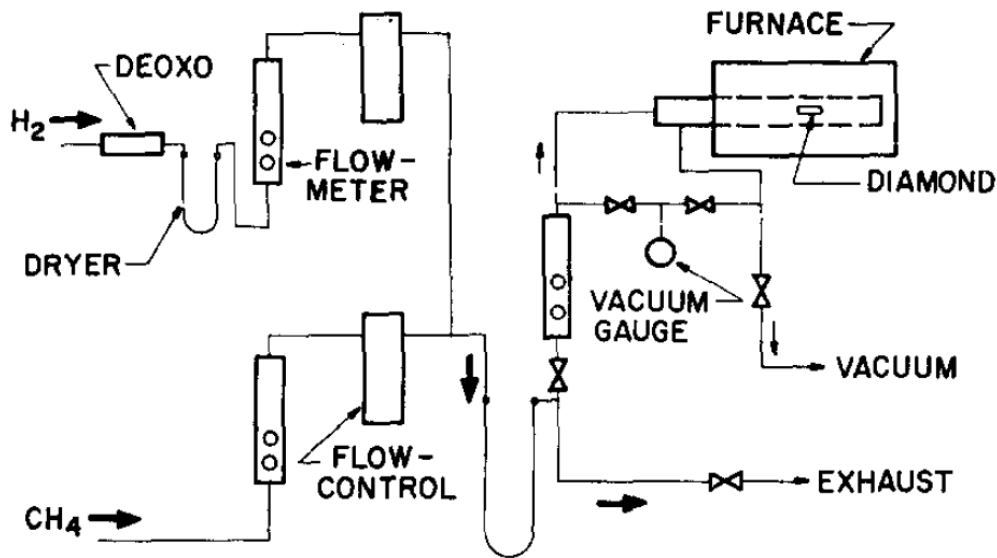


Figure 1.13 Schematic illustration of the reactor used by Angus's group *Reproduced from* [22]

1.6.2 Types of CVD Reactors

The CVD process relies on the reaction of volatile gas-phase precursors with a substrate surface to deposit a film of a desired material. In the case of diamond deposition, the carbon-containing precursor is typically methane, which is decomposed into reactive species (for example, CH_3), by some activation method. The first activation method employed in the CVD growth of diamond was thermal decomposition, accomplished using a furnace surrounding the growth cell [22], as shown schematically in Figure 1.13. A more sophisticated method of thermal decomposition is that of the hot filament reactor, which will be described in Section 1.6.2.1. There are several drawbacks to the hot filament reactor, and so electric discharges, such as direct current (DC), radio frequency (RF) or microwave power sources, are more commonly used as the activation method, particularly for high purity applications. This dissertation research is primarily concerned with microwave plasma reactors, which will be described in Section 1.6.2.2.

1.6.2.1 Hot Filament Reactors

The hot filament style of reactor, as shown in Figure 1.14, operates at lower than atmospheric pressure using a chamber that is continually evacuated by a vacuum pump. During deposition, hydrogen gas and a gaseous carbon source, typically methane, flow over the sample from the gas inlet at top of the chamber to the vacuum output port at the bottom. The input feedgas mixture is thermally activated as it passes over a filament of metal that is electrically heated to a very hot temperature, typically over 2000°C . A substrate, for example Si or Mo, sits on a heated substrate holder which is positioned a few mm below the filament. The filament is made of a metal that can withstand the high temperatures, such as tantalum or tungsten. The hot filament design is simple and inexpensive to operate, however there are a number of

drawbacks to this reactor style [2]. The filament metals react with the carbon containing precursor gas, forming metal-carbides, which make the filaments brittle and limits the useful lifetime of the filament. The filament is also very sensitive to corrosive and oxidizing gasses, which limits the possible gas chemistries that can be used in a hot filament reactor. The metal from the filament also tends to contaminate the grown diamond material, which is unacceptable for electrical and other high purity applications.

1.6.2.2 Microwave Plasma Reactors

Microwave plasma reactors generate a plasma by coupling microwaves into a resonant chamber through a dielectric window, most commonly made of quartz. Just as in the hot filament reactor design, the process gasses, typically hydrogen and methane, enter the reactor chamber from some gas inlet port, and are pumped out by a vacuum pump that continually keeps the chamber at lower than atmospheric pressure. The microwave energy couples to the gas-phase electrons, which transfer the energy to gas molecules, primarily through collisions. This causes the heating of the gas and the dissociation of gas molecules, creating a plasma.

1.6.2.2.1 NIRIM-type Reactors The first microwave plasma reactor for diamond deposition was demonstrated at NIRIM [30, 31], with the reactor design shown schematically in Figure 1.15. In this reactor, a fundamental mode 2.45 GHz microwave waveguide is modified by inserting a quartz tube, such that an electric field maxima occurs at the center of the quartz tube. A sample is placed just below the plasma ball that results (in what the authors referred to as the afterglow [31]). The position of the plasma ball can be fine-tuned with a sliding short at the end of the waveguide. The NIRIM-type reactor is also called a tubular microwave reactor, and this design is still widely used in research investigations due to the

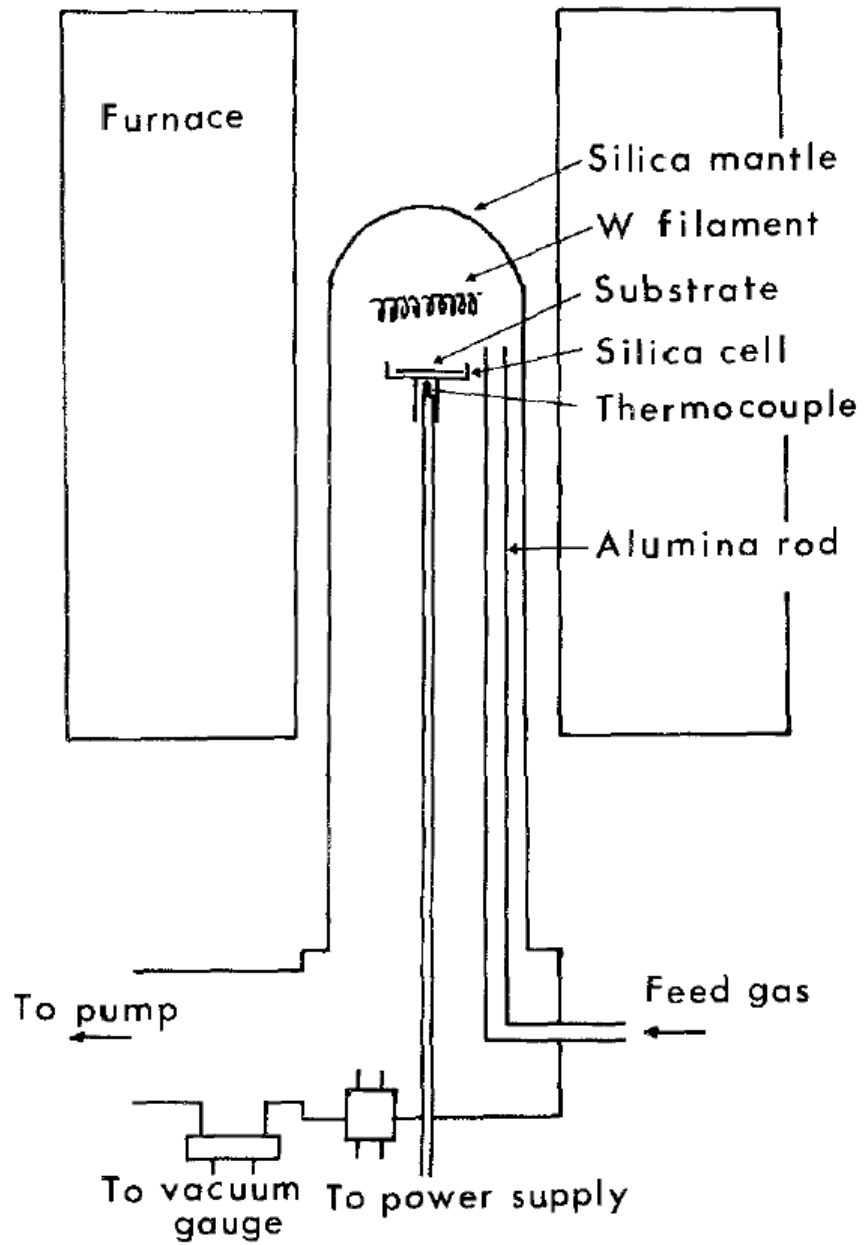


Figure 1.14 Schematic illustration of the hot filament reactor developed at NIRIM *Reproduced from [29]*

simple design and low construction costs compared to other microwave plasma reactors.

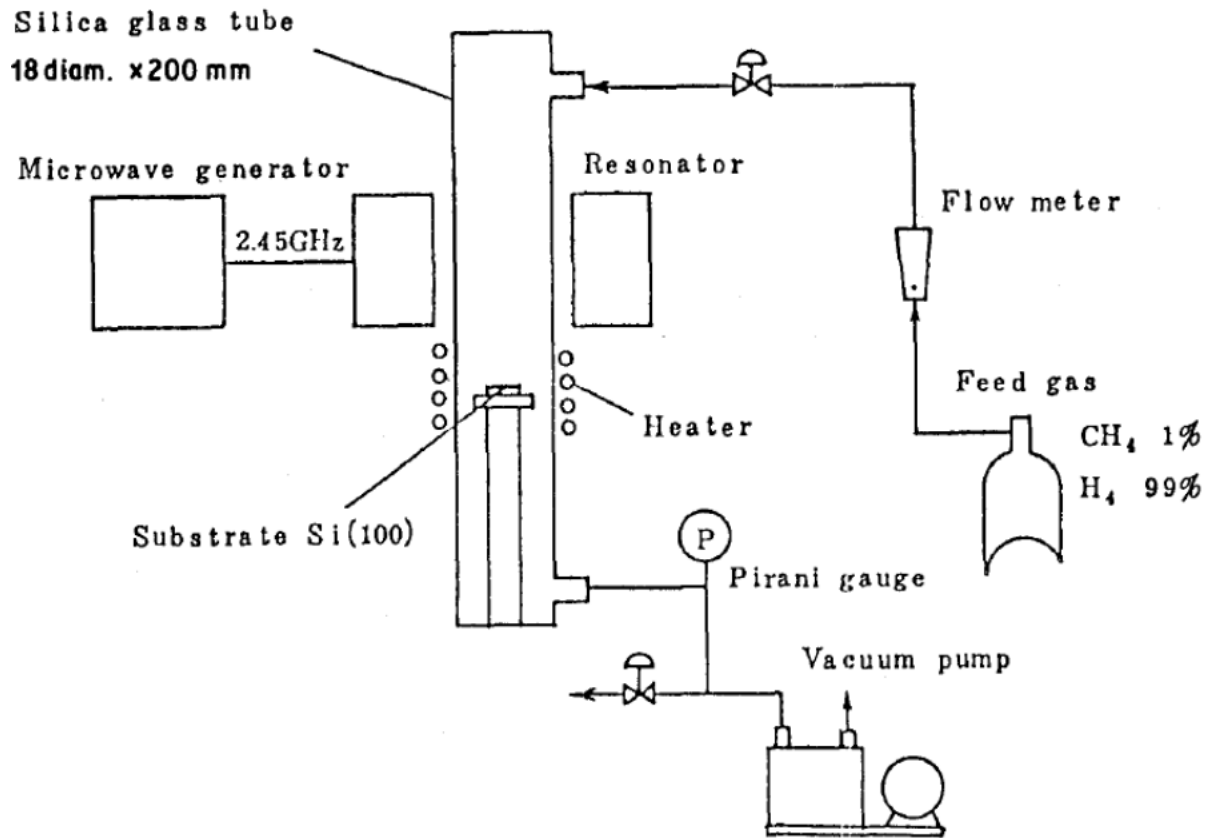


Figure 1.15 Schematic illustration of the microwave plasma reactor developed at NIRIM. Reproduced from Saito *et al.* 1986 [31]

The NIRIM-type reactor has several drawbacks, however, that can be significant for some applications. Bachmann *et al.* outlined several significant disadvantages to this design [32], which are:

1. The size of the reactor tube limits the possible substrate size, typically to less than 20 mm
2. The quartz walls of the reactor tube are in close proximity to the plasma, which results in the likelihood of contamination of growing samples with silica material etched from the tube walls.

3. Many of the deposition parameters are linked, since pressure changes and microwave power changes both cause variations in the temperature, etc. This prohibits the independent investigation of individual experimental parameters.

Attempting to overcome these drawbacks, Bachmann *et al.* designed the ASTeX style reactor [32], which will be described in the next section.

1.6.2.2.2 ASTeX-type Bell-Jar Reactors The original ASTeX-type reactor was the first bell-jar style microwave plasma CVD reactor for diamond growth, which was designed by Peter Bachmann and his coworkers [32], and then commercialized by Applied Science and Technology, Inc. (ASTeX). This reactor is shown schematically in Figure 1.16. The bell-jar contains the process gasses, and is pumped continuously by a vacuum roughing pump to below atmospheric pressure. The bell-jar sits inside a cylindrical 2.45 GHz microwave resonant cavity, and encloses a single electric field maxima, which couples the microwave power into the process gasses to generate the growth plasma. The ball-shaped plasma is located just above the substrate, which is placed on a substrate holder.

1.6.2.2.3 MSU-type Reactors The MSU-type reactor is a bell-jar style reactor that evolved out of the microwave plasma disk ion source (MPDS) that was developed and patented at Michigan State University (MSU) in the 1980s [34, 35, 36, 37, 38, 39, 40]. The MPDS was originally developed for applications as an ion source for large processing area etching and thin film deposition [41, 42, 43, 44]. The advantages of the disk shaped plasma, such as a large processing-surface-area-to-discharge-volume ratio compared to other microwave plasma reactors, make reactors based on the MPDS concept attractive for diamond deposition as well. The first microwave cavity plasma reactor (MCPR) designed for diamond growth and based

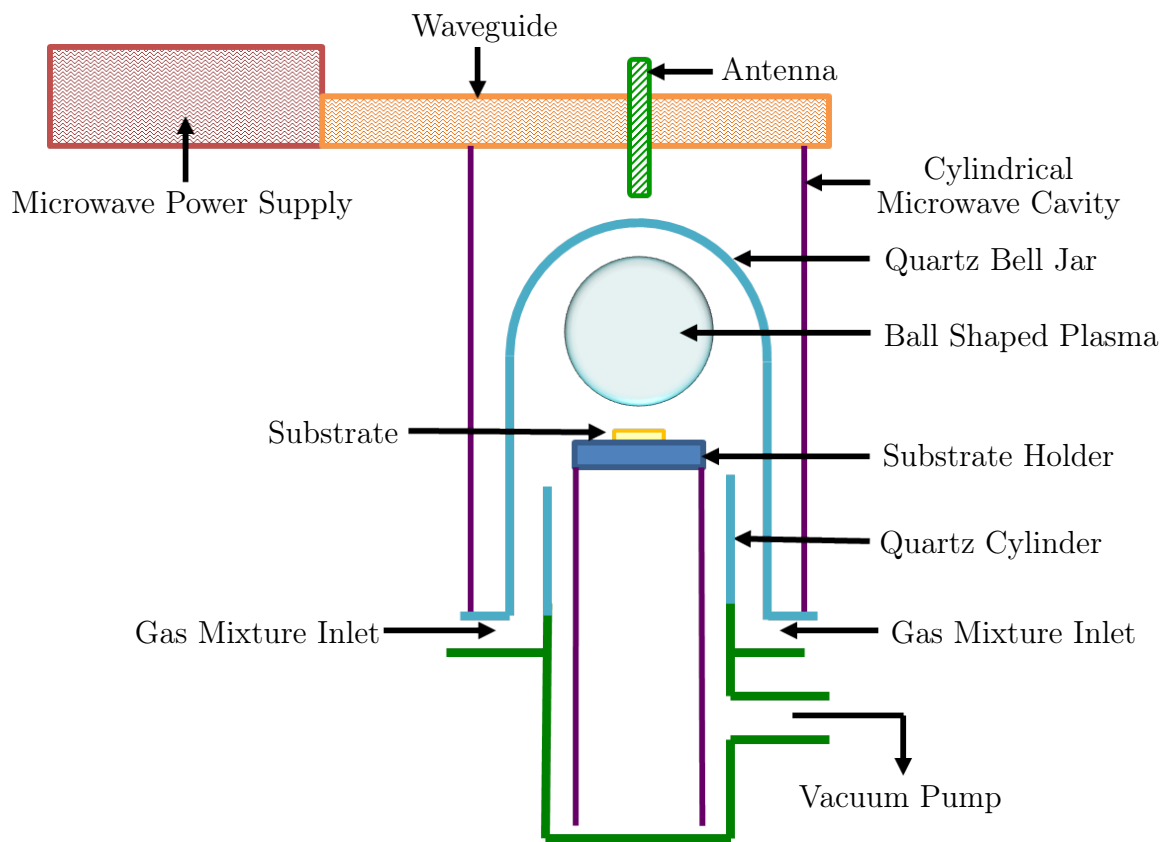


Figure 1.16 Schematic illustration of the ASTeX-type microwave plasma CVD reactor. *Adapted from [33].*

on the MPDS concept was built for Norton Co. at Michigan State University (MSU) by Jes Asmussen in 1986. It was subsequently evaluated by Norton Co. in Salt Lake City, Utah, in 1987, where the successful deposition of diamond was demonstrated. The MSU-patented technology was then licensed exclusively to Norton Co. through Wavemat Inc. A commercial version of the reactor was subsequently developed at Wavemat, and one of these reactors was put into operation at MSU in 1988. The current MSU-type diamond deposition reactor design evolved out of several generations of MCPR reactors, which were investigated in the dissertation work of Jie Zhang [45].

The first generation 7-inch MCPR reactor (MCPR7-1) is shown schematically in Figure 1.17. The resonant cavity is formed from a 7-inch-wide inside diameter, open-ended metallic cylinder. The top of the cavity is bounded by a water cooled sliding short, which can tune the cavity length. The sliding short is connected electrically to the cavity walls via the finger stock along the inside of the cavity. The bottom surface of the cavity is formed by the water cooled baseplate. 2.45 GHz microwave radiation is coupled into the side of the resonant chamber by the adjustable coaxial power-input port formed by the power coupling probe and its outer conductor. The plasma discharge can be viewed through the top screened window, and the substrate temperature can be measured through this top window by optical pyrometer. This reactor is operated in the TM_{011} single cavity electromagnetic mode for diamond deposition. In this mode, the discharge hovers over and is in direct contact with the substrate [46]. Although Zhang [45] succeeded in producing good quality diamond with the MCPR7-1 reactor, he noted two major limitations to this design.

1. The vacuum O-ring that seals the interface between the quartz dome and the chamber baseplate is located close to the hot plasma/substrate region of the reactor. This requires limiting the absorbed power level and substrate size for any given operating

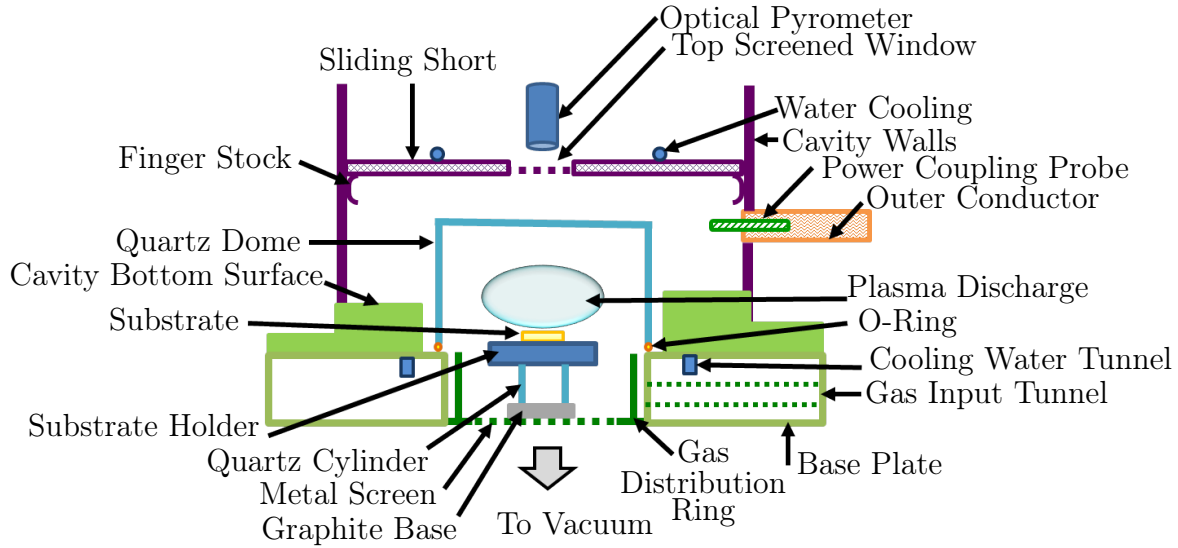


Figure 1.17 Schematic illustration of the first generation MSU MCPR CVD reactor. *Adapted from [45].*

pressure to prevent O-ring failure due to excessive heating.

2. The power is input through the side of the cavity wall, which produces a non-uniform electromagnetic ‘near-field’ close to the excitation probe. As the substrate area and/or input power are increased, this effect gets worse, and the plasma discharge is attracted toward the quartz dome walls. This results in non-uniform deposition on the substrate, and heating and deposition on the quartz walls, possibly resulting in melting the walls if the effect is too strong.

To overcome the near-field effects of the MCPR7-1, Zhang [45] investigated a second generation of the 7-inch MCPR reactor (MCPR7-2), shown schematically in Figure 1.18. This reactor uses a power-coupling input through the top of the cavity, rather than through the side as in the MCPR7-1. The probe and the sliding short are independently adjustable, allowing the tuning of the internal cavity impedance to reduce the reflected power. The new cavity of the MCPR7-2 was designed to be longer than the MCPR7-1, which allows

the TM_{012} and TM_{013} modes to be excited as well, in addition to the TM_{011} mode which was possible in the MCPR7-1. The new placement of the excitation probe requires that the pyrometer measurements be performed through a side-port screened viewing window, rather than directly overhead as in the MCPR7-1. The viewing window also serves as the outlet for the cooling air from a cooling inlet that was installed in the cavity sidewall. Air cooling is provided by a 100 cfm Dayton (model No. 4C443A) air blower, through the 2-inch diameter cooling air input. The cooling air is necessary for cooling the cavity walls and the quartz dome at higher input power conditions. Zhang [45] was able to deposit reasonable quality diamond material with the MCPR7-2, and the end feed design solved the issue of the non-uniformity caused by the near-field effects seen in MCPR7-1. However, the O-ring heating caused by the proximity of the vacuum sealing O-ring to the plasma and substrate continued to be an issue in this design.

The third and final 7-inch MCPR design (MCPR7-3) Zhang [45] investigated is shown schematically in Figure 1.19. The MCPR7-3 also uses the end feed design employed in the MCPR7-2, and overcomes the issue of the O-ring heating through a redesign of the quartz bell jar. The quartz dome is enlarged in both diameter and height over the previous MCPR generations, and utilizes a wide flange to create a greater separation between the bell-jar vacuum sealing O-ring and the hottest parts of the reactor. The gas mixtures are injected through a tunnel in the baseplate and distributed around the substrate through an annular dispersion ring. The reactor is mounted on top of a vacuum chamber with a chamber outlet leading to a vacuum roughing pump that provides the outlet flow for the process gasses. The MCPR7-3 creates a large symmetric, disk-to-hemispherical shaped plasma discharge volume that allows uniform deposition over large surface areas. The MCPR7-3 was further characterized in the dissertation work of Saeid Khatami [47], who studied the effect of reactor

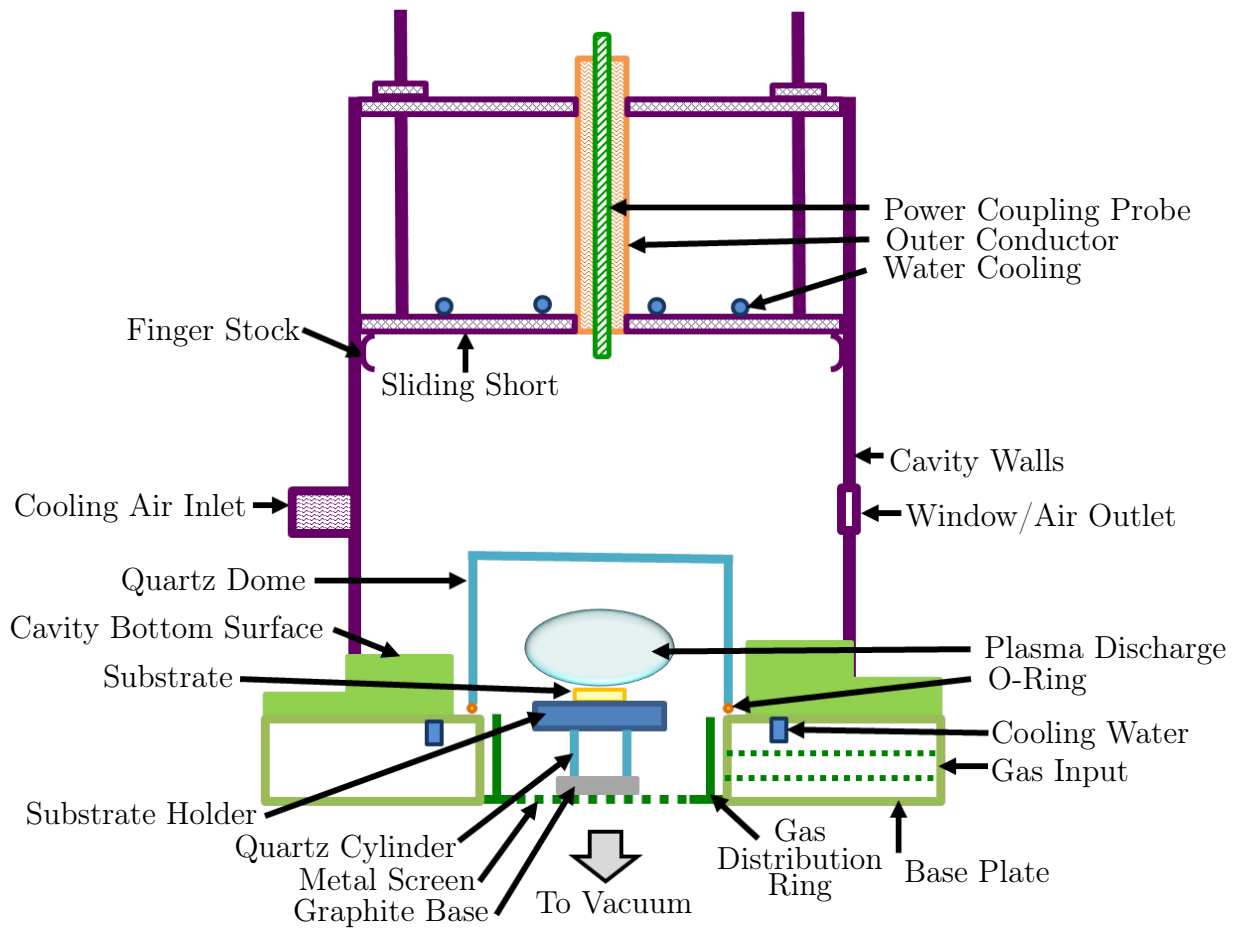


Figure 1.18 Schematic illustration of the second generation MSU MCPR CVD reactor. Adapted from [45].

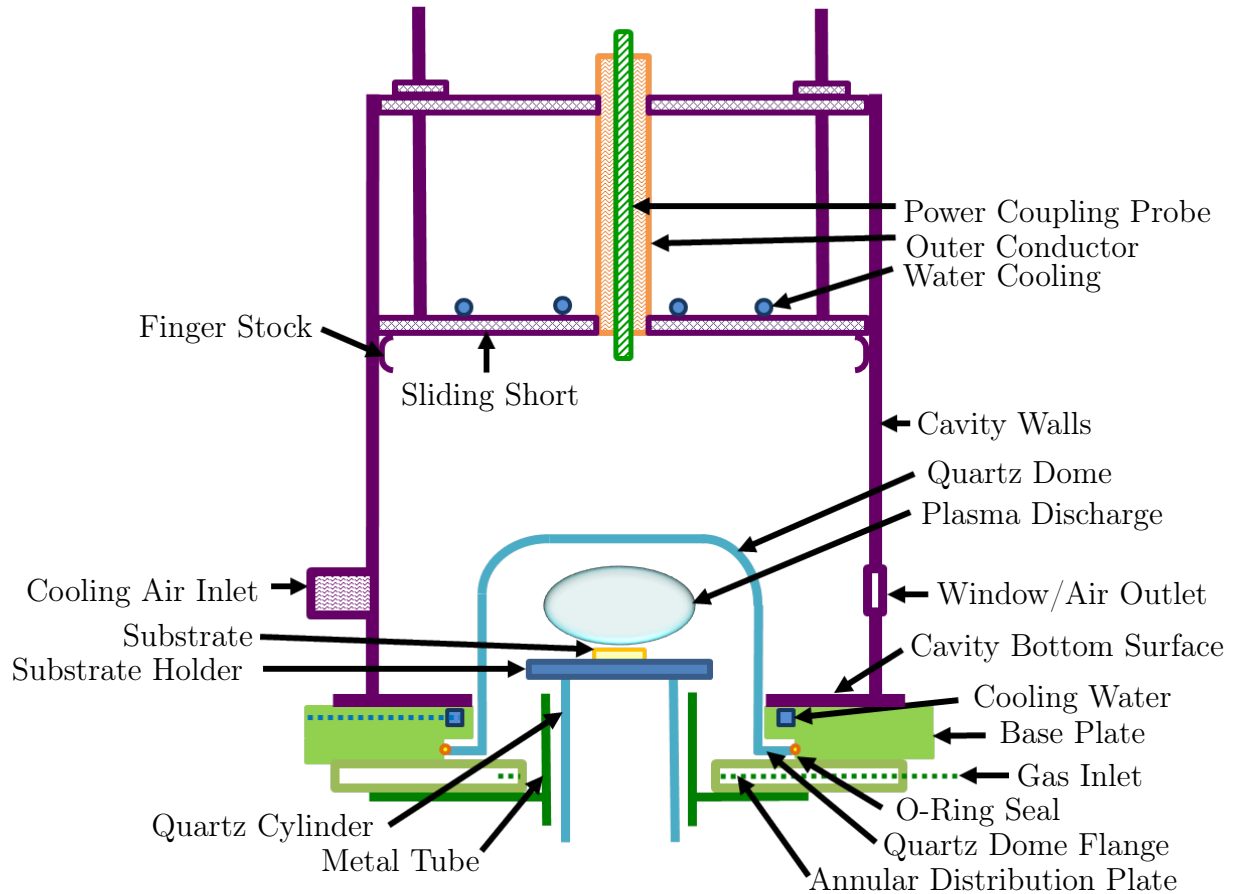


Figure 1.19 Schematic illustration of the third generation MSU MCPR CVD reactor. *Adapted from [45].*

variables on grown film properties for polycrystalline films grown at reactor pressures from 20-80 Torr.

Kuo-Ping Kuo, in his dissertation research [48], modified the MCPR7-3 to allow for better thermal management to enable depositions in the “high pressure” 80-150 Torr range. These improvements included a water-cooled substrate holder and a better air cooling system. The modified reactor is shown schematically in Figure 1.20. This modified high pressure MCPR reactor is now referred to as Diamond System 1 (DS1), and is still in operation at MSU. (This reactor is of significant importance to this dissertation, since much of the low boron doping work reported in Chapter 3 and all of the high boron doping work in Chapter 4 was

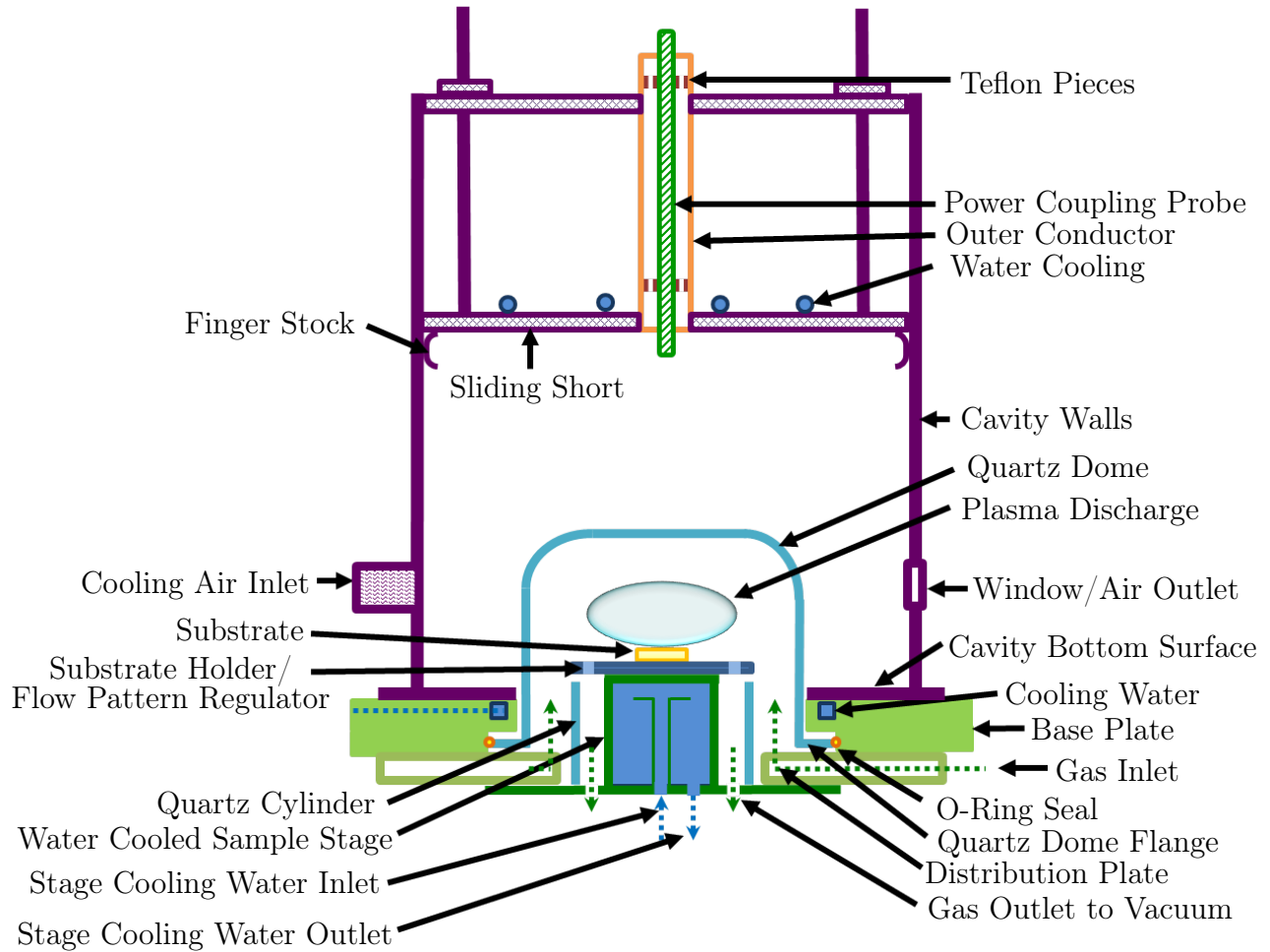


Figure 1.20 Schematic illustration of the modified high pressure MCPR CVD reactor. *Adapted from [49, 48].*

performed in DS1.)

DS1 was used for many years in the high pressure configuration as described by Kuo [49] until Rahul Ramamurti, a postdoctoral researcher at MSU, modified DS1 by adding B_2H_6 diluted in H_2 to the gas inputs [50, 51, 52]. The modified reactor gas flow path is the present configuration of DS1. DS1 will be described in detail in Section 2.1. The initial boron doping experiments performed on DS1 by Ramamurti *et al.* were doped polycrystalline film depositions [50]. With the confirmation of boron incorporation in the polycrystalline films, homoepitaxial growth of single crystal boron doped diamond was also subsequently

demonstrated [51, 52]. This dissertation expands on those results, exploring the deposition of diamond with both heavy and light boron doping levels for electronic applications.

During this dissertation research, the problem of the reactor memory effect, which will be described further in Section 1.7.2 and Chapter 3, complicated the deposition of high quality lightly boron doped diamond in DS1, which was also used for heavily boron doped diamond growth. As a result, a second 2.45 GHz system was purpose-built for the growth of lightly boron doped electronic grade SCD. This system was constructed as a part of this dissertation research, and is called Diamond System 6 (DS6). This system will be described in detail in Section 2.1.

1.7 Boron Doping of Single Crystal Diamond

The growth of BDD by CVD has a number of significant challenges which have so far limited its usefulness in generating samples of high enough quality with good enough repeatability to be commercially viable. Several of these issues will be described in this section. Section 1.7.1 will describe the issue of defects, Section 1.7.2 will describe unintentional doping, Section 1.7.3 will describe compensation, Section 1.7.4 will describe soot formation, Section 1.7.5 will describe the issue of decreasing doping efficiency, and the growth rate will be discussed in Section 1.7.6.

1.7.1 Defects

CVD growth of single crystal diamond tends to produce various types of crystal defects at the surface of growth. The most important types of these defects for this dissertation work are described in this subsection.

Pyramidal hillocks are defects that occur at the epitaxial surface of diamond grown on the (100) plane. Pyramidal hillocks grow as pyramids, with outward (111) faces from the (100) surface of growth, as shown in Figure 1.21

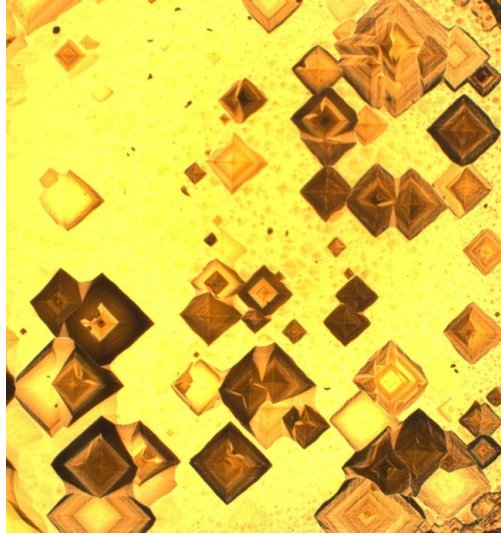


Figure 1.21 Example of pyramidal hillock type defects

Flat topped Hillocks are similar to pyramidal hillocks, except that instead of reaching an apex with (111) planed sides, the flat topped hillock retains a flat (100) top surface. Flat topped hillocks can occur with pyramidal hillocks, or separately without the presence of pyramids, such as those in the example of Figure 1.22

Unepitaxial crystallites are crystalline diamond defects that form at the growth surface that do not form structures which show planes related to the Miller indices of the growth substrate. They are typically small in size compared to hillock-type defects, and are often dark in color. They tend to form preferentially along lines of polishing damage in the homoepitaxial diamond surface, as shown in Figure 1.23

Threading dislocations are mixed dislocations, as previously discussed in Section 1.4.2, that result from dislocations that exist in the homoepitaxial substrate which extend up through the epitaxial plane and continue on into the newly grown diamond. They propagate in the

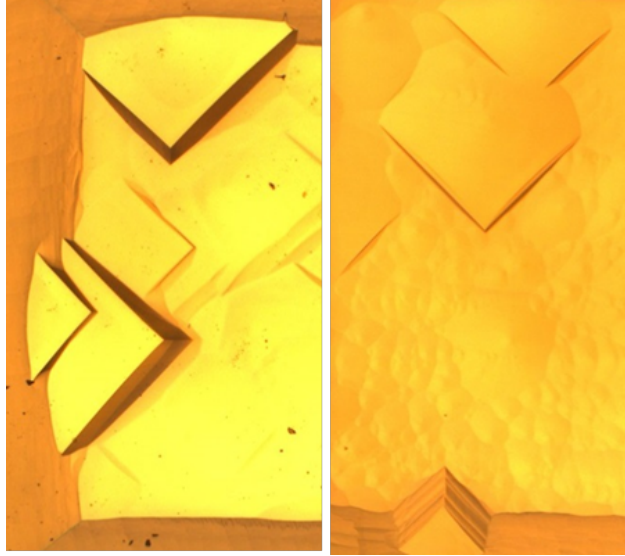


Figure 1.22 Example of flat topped hillock type defects

growth direction, and form thread-like defect structures in the diamond crystal. Threading dislocations can be particularly problematic in vertical architecture SBDs, as they have been found to be a significant cause of leakage current and lowered breakdown voltages [53]. Threading dislocation densities can be determined by etch-pit studies, in which the growth surface of the diamond is exposed to a H_2/O_2 plasma, and the resulting etch pits are presumed to be the termination of threading dislocations. The threading dislocations can also be visualized by x-ray topography, such as is shown in Figure 1.24, from the work of Friel *et al.* [54], which demonstrated that growing homoepitaxial diamond in a direction perpendicular to the direction of previous epitaxial growth leads to a reduction of screw- and edge-type threading dislocations in the resulting CVD diamond film.

1.7.2 Unintentional Doping

For lightly doped BDD, growing CVD diamond in a reactor that was previously used for boron doping, even during deposition runs in which no boron source intentionally added, will

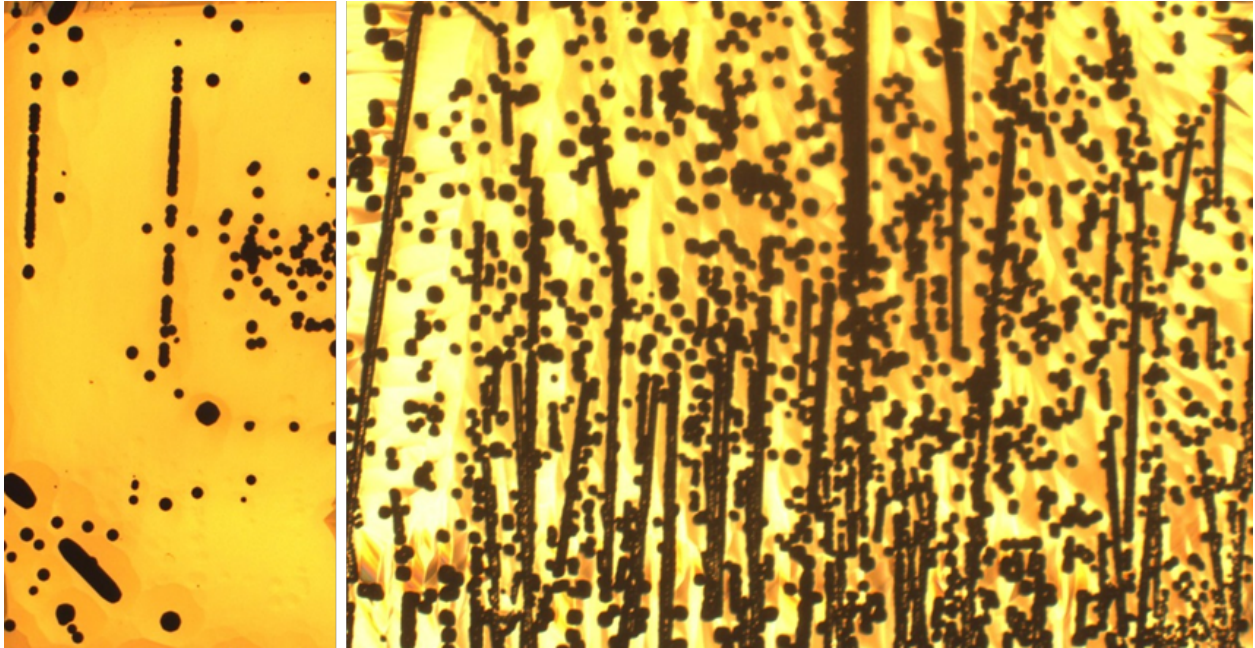


Figure 1.23 Example of unepitaxial crystallite type defects

result in a samples that still show some level of boron doping, typically on the order of 10^{16} cm^{-3} to 10^{17} cm^{-3} . This unintentional doping, also known as the "reactor memory effect," is a considerable problem for reliably controlling the boron levels in very lightly doped samples.

1.7.3 Compensation

As previously discussed in Section 1.5, boron doped diamond has a deep acceptor activation level of approximately 0.37 eV. This results in only a small percentage of holes electrically active at room temperature, and the number is reduced significantly if a compensating donor concentration is present. For boron doped diamond where a donor level from N or P is present in an appreciable concentration, the percentage of boron available for conduction is very low. It is therefore critical to minimize the concentration of N and P present in the reactor during growth to prevent the conduction properties from being adversely affected by a compensating donor concentration.

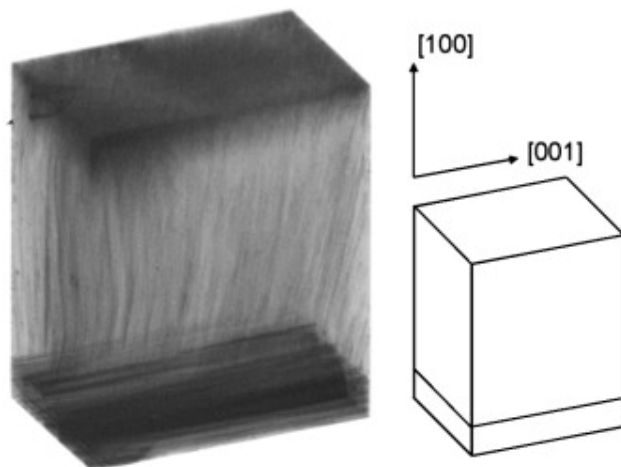


Figure 1.24 X-ray topography image, showing threading dislocations in two generations of diamond growth. *Reproduced from Friel et al.* [54]

1.7.4 Soot Formation

A major problem in the growth of single crystal diamond with high levels of boron is the unintentional deposition on the reactor walls of a material commonly referred to as ‘soot.’ Soot deposition on the quartz bell jar can cause excess reflected microwave power and heating, resulting in melting of the quartz bell jar and possible reactor damage and safety concerns, and therefore is a very serious problem. Soot deposition is not entirely understood, however it is known to be correlated to higher methane and boron concentrations, and higher microwave power density (MWPD) [55]. Soot is particularly problematic for the growth of thick, heavily doped layers, like what would be required for vertical Schottky barrier diodes, as discussed in Section 1.3.2. As an example, in the work of Achard *et al.* [55], to increase the growth rate of their boron doped diamond, and therefore decrease the total reactor time needed for the growth of a thick layer, they increased the reactor pressure. However, the new plasma chemistries, likely resulting from the necessary increase in MWPD to achieve the same substrate temperature, caused increased soot deposition inside the reactor. The result was to reduce the maximum possible deposition time before the deposition had to be

stopped to clean the reactor. Although the growth rate increased, the resulting decrease in the total deposition time therefore actually decreased the total grown diamond thickness. As a result, investigations of heavily boron doped, high growth rate chemistries must be of limited duration to prevent the excessive deposition of soot.

1.7.5 Doping Efficiency

Another area of current research interest is the decreasing doping efficiency from the concentration in the plasma feedgas to the solid phase grown diamond, which has been reported by several groups. Tokuda *et al.* [56] attributed this decrease to the modification of the plasma chemistry, or a change in the growth mode. Achard *et al.* [57] observed a similar trend, however they cite an optical emission spectroscopic study [58] showing that increasing diborane concentration up to 20,000 ppm in the plasma feedgas does not affect the gas temperature (T_g), the electron temperature (T_e), nor the electron number density (n_e), which are the parameters that principally govern the plasma chemistry. Achard *et al.* instead postulate that at higher boron-to-carbon ratios in the gas phase ($([B]/[C])_{\text{gas}}$), the boron incorporation mechanism changes, for example by a reduction in the number of available incorporation sites. They suggest that this is possibly due to a change in the surface morphology resulting in a reduction in defect sites, which preferentially incorporate boron [57]. The factors affecting the doping efficiency are not well understood, and are an area of current research interest.

1.7.6 Growth Rate

Vertical architecture diode structures, as previously described in Section 1.3.2, require a freestanding p^+ -substrate. To produce such a substrate by CVD, a layer of heavily boron

doped diamond must be grown to a thickness such that it is mechanically handleable after laser cutting and polishing, which effectively means it must be grown to at least 300 μm thick. To achieve this thickness, it is therefore necessary to increase the growth rate as much as possible to reduce the total reactor time required for the growth, since typical growth rates are approximately $10 \mu\text{m h}^{-1}$ for heavily boron doped diamond [55]. This needs to be balanced against the doping efficiency and soot formation however, as will be further discussed in Chapter 4.

1.8 Surface Conductivity

In a semiconductor material, an electron excited up to the conduction band minimum (CBM) is not typically free to leave the material, because it encounters a small energy barrier at the interface, which is known as the electron affinity, χ . When the electron is not free to leave the material due to this barrier, the material is said to have positive electron affinity (PEA). Diamond, however, is unusual in this respect. When the surface of diamond is terminated with hydrogen, the C-H bonds form a dipole layer at the surface. Hydrogen termination is common, as it is the state of an untreated diamond surface grown by hydrogen-plasma CVD.

A negative electron affinity (NEA) indicates that the vacuum level energy lies below the CBM, and therefore the emission of electrons into vacuum is possible without overcoming an energy barrier. The most obvious consequence of the NEA surface is a high photoelectron yield from hydrogen terminated diamond surfaces [59, 60]. The ease with which electrons in the conduction band can be emitted has sparked considerable interest in diamond devices for electron source applications [61].

A hydrogen terminated diamond surface also causes the formation of a surface layer of

conductivity. The role of hydrogen in the conductivity of diamond was first described by Landstrass and Ravi [62], who attributed the unstable carrier properties of diamond films after annealing to the hydrogen passivation of defect states. Albin and Watkins [63] confirmed the observation that the conductivity of diamond samples increases by several orders of magnitude after exposure to hydrogen plasma, and also attributed the resulting increase in conductivity to the passivation of deep levels. Maki *et al.* [64] instead attributed the generation of holes to the formation of shallow acceptor levels as hydrogen incorporated near the surface region. Hall effect measurements confirmed the carriers were *p*-type, and SIMS results showed that the presence of hydrogen near the surface was greater for hydrogenated surfaces than oxidized ones, which gave credibility to the model of the generation of holes from acceptor levels caused by incorporated hydrogen [65, 66, 67].

A different mechanism for the origin of the surface conductivity was proposed by Kowarada *et al.* [68]. They reported scanning tunneling spectroscopy (STS) results that showed a negative charge at the surface, which they attributed to the presence of hydrogen terminating the dangling carbon bonds. They suggested a model where the negative charge causes the formation of an accumulation region of holes near the surface, due to charge neutrality. This observation of the negatively charged surface state then raised the question of whether the conduction method was due to the presence of hydrogen within the film as was originally believed, or due to the hydrogen termination on the surface.

The location of the hydrogen participating in the surface conductivity was clarified when Maier *et al.* [69] described conclusively the mechanism by which the accumulation layer forms. Expanding upon a qualitative explanation first proposed by Ri *et al.* [70], Maier *et al.* described a redox reaction in which a layer of water adsorbed on the diamond surface forms from contact with the atmosphere. This water layer provides an electron sink for the layer of

holes that accumulates at the surface.

The dipole layer formed by the C-H bonds induces a negative electron affinity (NEA). In diamond, χ is a function of hydrogen coverage, and on the (111) surface ranges from -1.27 eV for a fully covered surface to $+0.38$ eV for a hydrogen free surface [71]. The surface conductivity can be removed by dehydrogenating the surface. This can be practically accomplished by oxygen terminating the surface, for example by UV-ozone treatment [72], or by exposure to an oxygen plasma. Maier *et al.* [69] also found that acid treatment with $\text{HNO}_3 + \text{H}_2\text{SO}_4$ is sufficient to oxidize a sample to a level necessary to remove surface conductivity. All of the samples electrically characterized in this work were at minimum acid treated to remove the effects of surface conductivity. This is critical, since the room temperature surface conductivity is on the order of 10^{-4} to $10^{-5} \Omega^{-1}$ [73].

Chapter 2

Experimental Methodology

This chapter describes the experimental methods used to grow and characterize the samples used in this dissertation research. The reactors used in the growth experiments of this dissertation are described in Section 2.1.

A number of characterization methods are required to determine the electronic and physical properties of the grown samples. The development of improvements in doping efficiency and electrical properties require knowledge of the boron doping level and methods of electrical characterization. Comparisons between samples grown under different conditions are necessary for the interpretation of growth experiments.

The determination of the concentration of boron in *p*-type semiconducting diamond is important for a number of reasons, including the determination of doping efficiency for highly doped samples and as a quantification of the reactor memory effect for unintentionally doped samples. Methods for the determination of the boron concentration in single crystal diamond are somewhat limited, and include Hall Effect, SIMS and FTIR measurements. Compared to Hall Effect, FTIR measurements are much faster and do not require contact deposition. Compared to SIMS, FTIR is non-destructive, takes only minutes, and the instrumentation required is significantly less expensive. The FTIR techniques that are used for the determination of boron concentration are summarized in Section 2.2, and SIMS is

described in Section 2.3.

The determination of the conductivity and the conductivity activation energy of boron doped diamond samples allows for the characterization and improvement of the electrical properties of doped diamond. Temperature dependent four point probe measurements will be described in detail in Section 2.4.

The control of the surface termination is important to separate the effect of surface conductivity from the bulk conductivity of the grown sample. Contact angle measurements for the determination of the surface termination will be described in Section 2.5.

A final characterization method, X-Ray Diffraction, for the determination of the miscut angle of the growth surface from the diamond lattice orientation, will be described in Section 2.6.

2.1 Experimental Diamond Deposition Reactor Systems

This section will describe the two experimental diamond deposition systems used in this dissertation research. Diamond System 1 (DS1) was previously described in its current configuration in the dissertation work of Kuo-Ping Kuo [48], with the exception of the addition of a diborane gas source to the gas flow control and vacuum system. For brevity, only that system will be described in Section 2.1.1.

Diamond System 6 (DS6) was purpose built during this dissertation research for the deposition of lightly boron doped, high quality single crystal diamond. As this reactor has never been previously described, its design and system configurations will be treated in detail in Section 2.1.2.

2.1.1 Diamond System 1 (DS1)

Diamond System 1 (DS1) is a MSU-type diamond deposition reactor, as previously described in Section 1.6.2.2. Its current configuration was described elsewhere [49, 48], except for the modification of the gas flow control and vacuum system to include diborane gas as the boron source. The current configuration of this system will be presented in Section 2.1.1.1.

2.1.1.1 Gas Flow Control and Vacuum Systems

The DS1 gas flow control and vacuum systems used for this dissertation research are shown in Figure 2.1. In this configuration, diluted diborane is used as a source gas for the reactor, from a tank of either 1000 ppm or 25 ppm B_2H_6 in H_2 , (1). The source gas bottle is kept in a gas safety cabinet (5), due to the health hazard posed by the diborane gas. The other source gasses are H_2 (2), CH_4 (3), and CO_2 (4). CO_2 was only connected to the system for some of the experiments performed in this work, which will be described in greater detail in Chapter 3. The flow rates of these gasses are controlled by MKS type 11159A mass flow controllers (6), which are operated by the 4-Channel MKS 247C Mass Flow Controller readout (7). The individual gas lines each have isolation valves (8) to isolate the lines before mixing, and then flow through a main isolation valve (8) which can isolate all of the gas lines from the reactor. The gasses enter the reactor through the baseplate (9), which then passes the gas through an annular gas plate and then through the gas distribution plate, which distributes the source gasses over the sample surface in a uniform ring. The exhaust gas is then pulled down into the reactor vacuum chamber (10) by the ALCATEL 2033 mechanical roughing pump (11). The roughing pump exhaust (12) leaves the laboratory through a chimney vent. To prevent the concentration of H_2 or B_2H_6 from reaching dangerous levels, N_2 (13) is used to dilute the exhaust gas mixture, with a flow rate controlled by the exhaust purge mass

flow controller (14). The N₂ tank (13) is also the source of the venting gas used to bring the vacuum chamber (10) up to atmospheric pressure after a deposition run. Two manual venting valves (15) control the flow of N₂ into the chamber, and the redundancy ensures there are no N₂ leaks during depositions. An oil trap (16) is attached to the inlet of the mechanical roughing pump (11) to ensure that no oil can backflow into the reactor chamber. The pump can also be isolated from the reactor by means of a roughing valve (17), which can be closed to permit the chamber to be vented to atmosphere while the roughing pump is still running. During depositions, the pressure in the chamber is controlled by a throttle valve (18). The reactor pressure is read by the high pressure gauge (19), and the MKS Type 651 Pressure Controller uses this input to control the throttle valve (18) to achieve a desired set-point pressure. Before deposition runs, the vacuum chamber is pumped down to a maximum of 1 mTorr base pressure, which is read by the low pressure gauge (21). The low pressure gauge is protected from overpressure by an isolation valve (22).

2.1.2 Diamond System 6 (DS6)

Diamond System 6 (DS6), like DS1, is a MSU-type diamond deposition reactor, as previously described in Section 1.6.2.2. DS6 was built during this dissertation research, with planning and construction that began in the spring of 2012. The reactor memory effect, which causes unintentional doping, as described in Section 1.7.2, was a significant issue in early low boron doping results of this work, which will be presented in Chapter 3. It was determined that it would be problematic to obtain diamond material of high enough quality with a low enough level of doping from DS1, as it was also used for heavily boron doped diamond deposition. As a result, this new diamond deposition system was planned and built for low level boron doping. The result is DS6, which has been used for this dissertation research to successfully

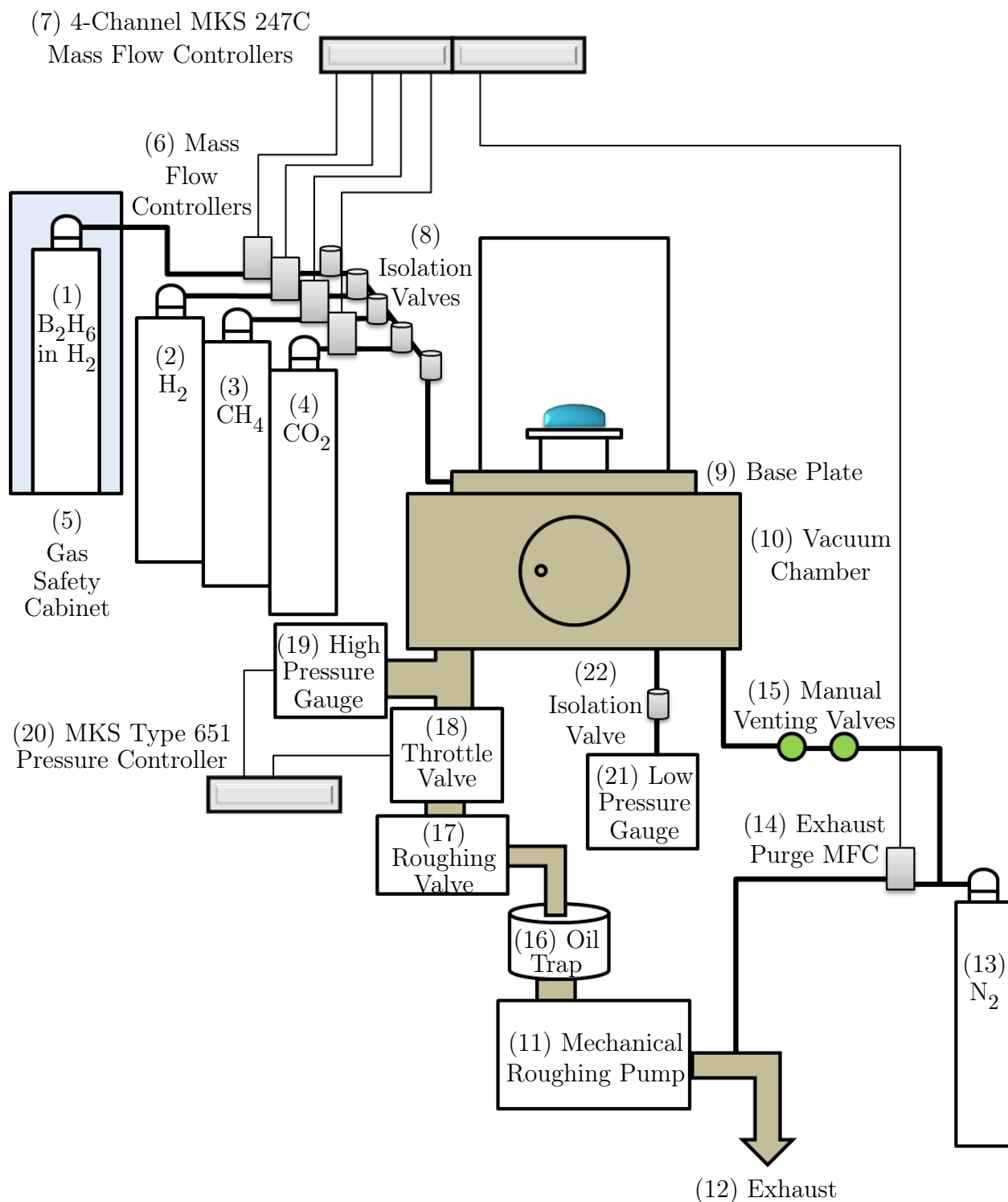


Figure 2.1 Schematic illustration of the current configuration of the gas flow path in DS1

grow lightly doped SCD for electronic applications, as will be presented in Chapter 3 and Chapter 5. This section will describe the design and construction of DS6, broken down into the main systems of the reactor.

2.1.2.1 Gas Flow Control and Vacuum Systems

The gas flow and vacuum system designed for DS6 is shown in Figure 2.2. Just as in DS1, diluted diborane is used as the boron source. DS6 was purpose built for low level boron doping, and so a 25 ppm B_2H_6 in H_2 tank (1) is used (unlike DS1, where a 1000 ppm tank is used for heavy boron doping experiments). The diborane source gas bottle is kept in a gas safety cabinet (5), due to the health hazard posed by the diborane gas. This diborane bottle and safely cabinet were already present in the lab prior to beginning building DS6. They had originally been purposed for Diamond System 5 (DS5), which is presently used exclusively for *n*-type doping, using phosphine gas from an adjacent safety cabinet. As the installation of a gas safety cabinet is a significant expense in the construction of a doped diamond system, the location of the existing cabinet determined the location of DS6 within the laboratory. As a hazardous gas, connections to gas lines running diborane have been designed to be VCR connectors where connectors cannot be avoided. As each VCR connection requires a welded end, it is desirable to minimize the number of connectors, as well as the distance between the gas cabinet and the system. Where connections are necessary, such as the connections to the mass flow controller, it is preferable that the connection be in a ventilated safety box, such as the gas safety cabinet where the gas lines connect to the source gas tank. For this reason, the mass flow controllers and isolation valves were mounted inside a ventilated stainless steel box, as shown in Figure 2.3. The ventilation box was constructed from a 24" \times 24" \times 12" steel enclosure (Omega Engineering Part Number SCE-24N2412LP). A removable 24" \times 24" sub

panel (Omega Engineering Part Number SCE-24N24MP) allowed for the installation of the mass flow controllers (5) and isolation valves (7). The ventilation box was mounted above the heat exchanger (which will be described in Section 2.1.2.3), at a height that would permit the top lid of the heat exchanger to be opened for servicing while still in place. The ventilation outlet is on the side of the ventilation box rather than the top, as an original design had the ventilation tubing running into the ventilation system from the gas safety cabinet, at the height at which the outlet was installed. A later design instead ran the ventilation to join the ventilation system above and beyond the wall on which the box is mounted, but uses the same outlet port for convenience, as the ventilation flow was still sufficient for the application.

The other process gasses are H_2 (2) and CH_4 (3). Ultra-high purity (UHP) gas cylinders are used, with 99.999% purity (H_2) and 99.99% purity (CH_4). They are secured to a gas cylinder rack (USA Safety Part Number PR477FS), as shown in Figure 2.4. The laboratory floor space available for the construction of DS6 was limited, and so the system is limited to four gas cylinders. (The other two cylinders shown in Figure 2.4 are N_2 bottles (12), for exhaust purging.) The process gasses (H_2 and CH_4) are attached to pressure regulators with rack mounted brass manifold protocol stations (Airgas Part Number AAX1100). The use of the protocol stations, rather than attaching the pressure regulators directly to the cylinders, simplifies the gas bottle changing process.

The gas lines for the process gasses were installed by Karl Dersch of MSU, who was significantly involved in the final steps of the system construction. The gas lines were bent and cut from 20 ft long, 1/4-inch OD by 0.035-inch wall thickness stainless steel tubing (H.E. Lenon Part Number SS-T4-S-035-20). The gas flows are controlled by MKS 1479A mass flow controllers (5), and each line can individually be isolated using the isolation valves

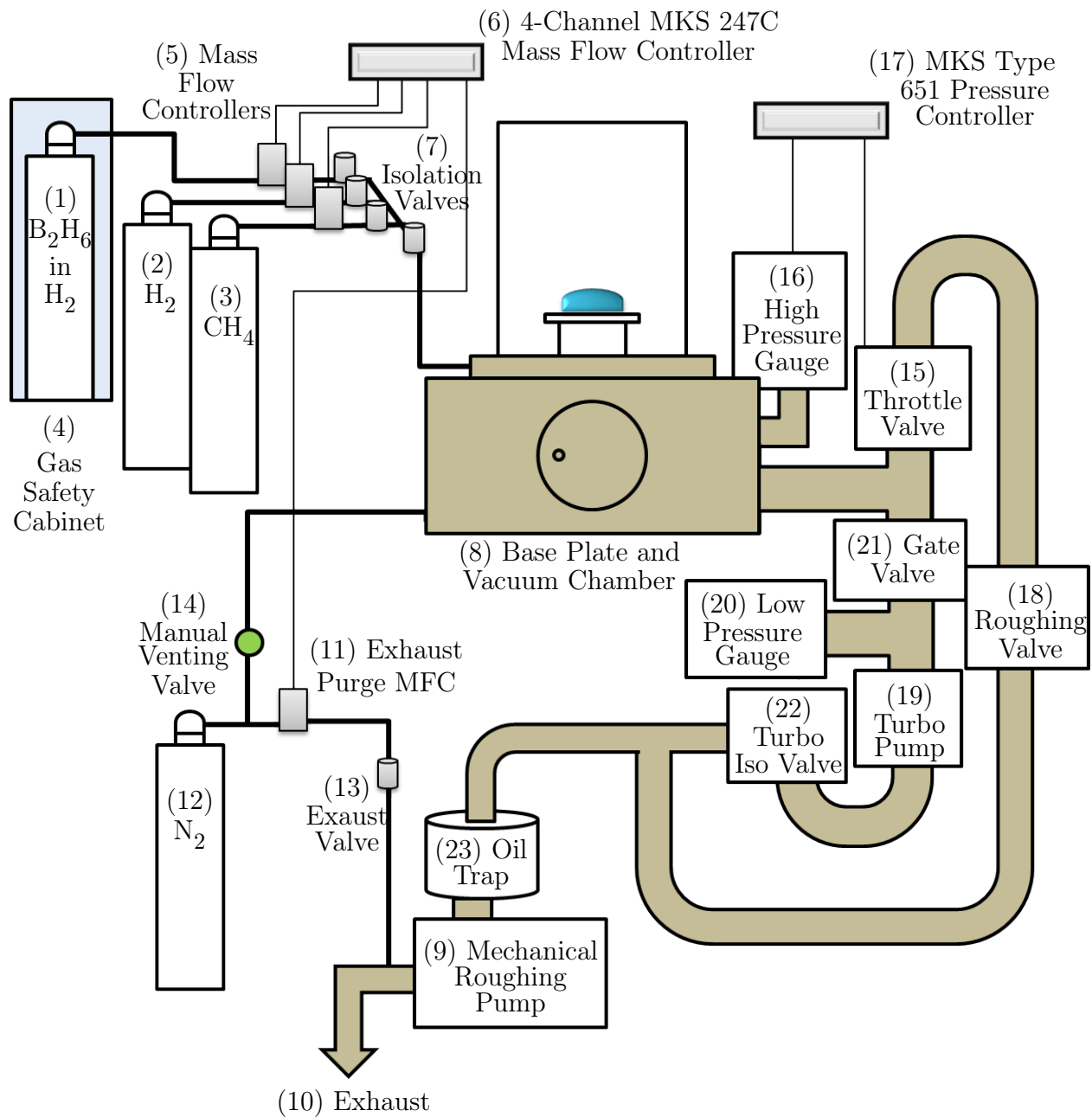


Figure 2.2 Schematic illustration of the gas flow path designed for DS6



Figure 2.3 (a) Photo of the DS6 gas line connection ventilation box, with the front door closed (b) Photo of the DS6 gas line connection ventilation box, with the front door open, showing the mass flow controllers and isolation valves inside.

(7). Two of the normally closed 316L stainless steel high-purity bellows-sealed valves were salvaged from a previously existing system. The remaining gas line isolation valve and the main isolation valve were selected to also be 316L bellows sealed valves (H.E. Lenon Part Number SS-BNV51-CM). The main isolation valve is connected to the mixed gas line, and can stop the flow of the total process gases. The mass flow controllers (5) and the isolation valves (7) are housed within the previously described venting box. The mass flow controllers are operated by a 4-Channel MKS 247C Mass Flow Controller (6), salvaged from a previously existing setup.

The gasses enter the reactor through the baseplate (8), which was built for DS6 by the MSU Physics Shop. The gas then passes through an annular gas plate and then into the gas distribution plate, which distributes the source gasses over the sample surface in a uniform ring. The exhaust gas is pulled down into the vacuum system by the mechanical roughing pump (9). A 14.8 cubic foot per minute (CFM) remanufactured Alcatel/Adixen 2021SD standard series rotary vane Pascal-series vacuum pump (Kurt Lesker Part Number



Figure 2.4 DS6 Gas Bottle Rack

AV-UM2021SDR), was selected as the mechanical roughing pump.

The roughing pump exhaust (10) leaves the laboratory through a previously existing chimney vent. To prevent the concentration of H_2 or B_2H_6 from reaching dangerous levels, purging N_2 (13) is added to the exhaust to dilute the exhaust gas mixture, with a flow rate controlled by the exhaust purge mass flow controller (11). The mass flow controller was selected to be a 10,000 sccm N_2 1479A Mass-Flo Analog, Metal-Sealed Mass Flow Controller (MKS Part Number 1479A01314CR1BM). The high flow rate ensures that the reactor flow rate will not be limited by the rate at which the exhaust can be diluted. The exhaust purge rate does not need to be highly accurate, and so more precise control is not needed. The N_2 tank (13) is a standard gas tank with 99.97% purity. A normally open bellows sealed exhaust valve (13) can be used to isolate the exhaust purge line. Both the exhaust mass flow controller (11) and valve (13) are located in the safety ventilation box shown Figure 2.3. The N_2 tank (12) is also the source of the venting gas used to bring the vacuum chamber (8) up

to atmospheric pressure after a deposition run. A manual venting valve (14) controls the flow of N₂ into the chamber.

During depositions, the pressure in the reactor is controlled by a throttle valve (15), shown in Figure 2.5. The throttle valve was salvaged from a previously existing experimental setup. The reactor pressure is read by the high pressure gauge (16), which was selected to be a MKS 626B capacitance manometer, with a maximum rating of 500 torr (MKS Part Number 626B52TLF). The high pressure gauge attaches to a 2-3/4" CF flanged connection directly out of the vacuum chamber (8). The close proximity of the high pressure gauge (16) to the reactor volume ensures a reliable reading of the pressure. The throttle valve is controlled by a MKS Type 651 Pressure Controller (17), which uses the input from the high pressure gauge (16) to achieve a desired set-point pressure. The throttle valve can be isolated from the roughing pump (9) by the roughing valve (18). The roughing valve was selected to be an O-Ring Flapper Angle Stainless Steel Valve (Kurt Lesker Part Number SA0100PVQF).



Figure 2.5 DS6 Throttle Valve

DS6 was designed for high purity applications, and therefore a turbo pump (19) is included in the system to reduce the pre-deposition reactor base pressure to increase the gas purity of the reactor environment. A Leybold TMP 50 Turbo Pump (Kurt Lesker Part Number LH-85402) was selected as the turbo pump, as shown in Figure 2.6. The turbo pump is connected to an NT10 Controller (Kurt Lesker Part Number LH-85901), which is operated by the user before depositions (and not during the growth runs). To measure the pre-deposition base pressure, a KJLC 423 Series Cold Cathode Gauge (Kurt Lesker Part Number K4232) was selected as the low pressure gauge (20). The low pressure gauge is controlled by a Torr readout Gauge Controller (Kurt Lesker Part Number K9431206T), which allows the user to read out the base pressure before depositions start.



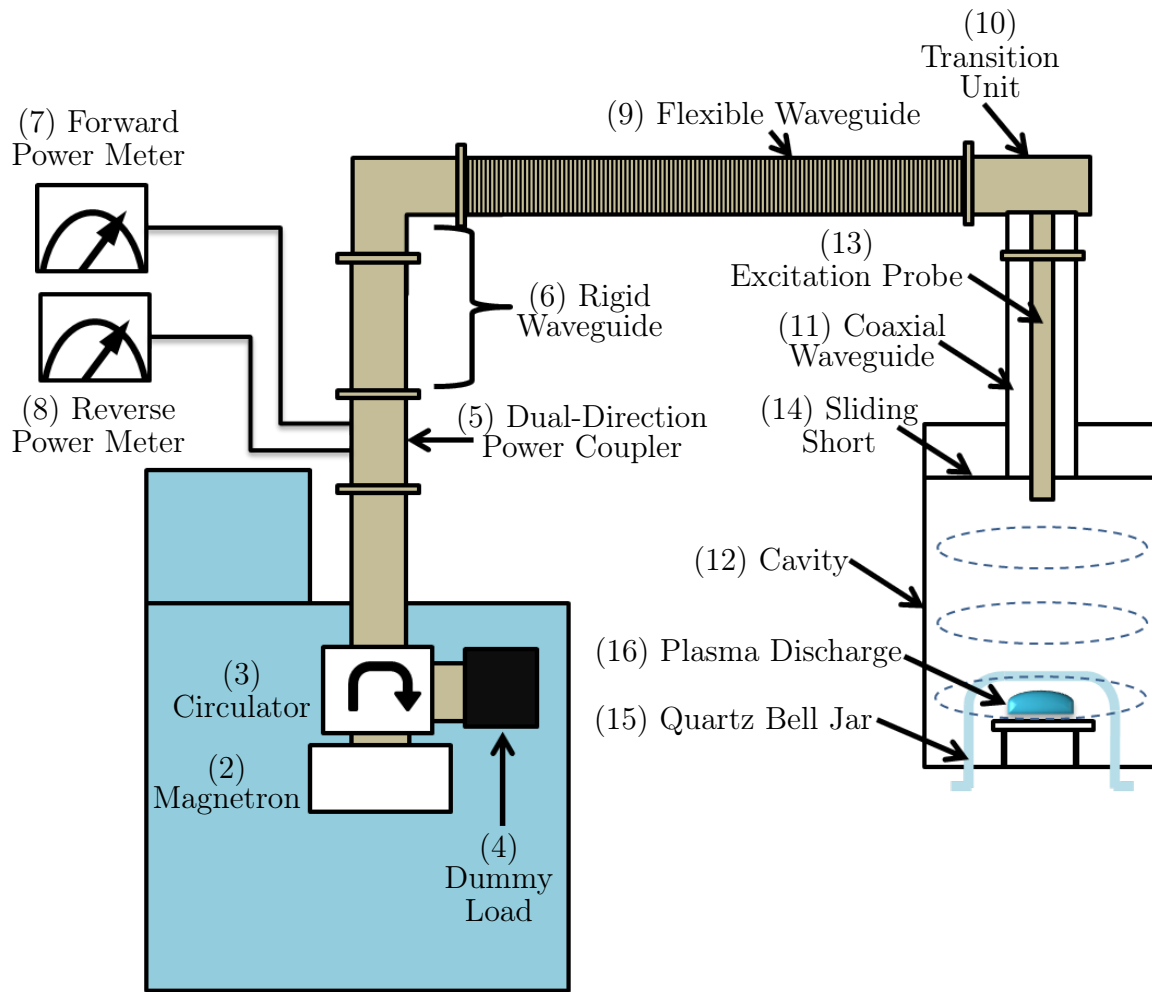
Figure 2.6 DS6 Turbo Pump

The vacuum pumping lines form a circular loop to allow for appropriate turbo pump operation. Both the turbo pump (19) and the low pressure gauge (20) should be protected from the reactor gas chemistries during depositions, even though they are turned off during depositions. The system was designed to have a standard stainless steel gate valve (Kurt Lesker Part Number SG0250PCCF) that can isolate these sensitive components. An O-Ring

flapper angle stainless steel valve (Kurt Lesker Part Number SA0075PVQF) was also included, to serve as a turbo pump isolation valve (22). During turbo pump operation, the roughing valve (18) should be closed, to form a direct path from the reactor out through the turbo pump (19), which connects to the roughing pump, and then out to the exhaust (10). By closing both the turbo pump isolation valve (22) and the roughing valve (18) with the turbo pump turned off, the chamber can be isolated from the roughing pump (9) permitting the chamber to be vented to atmosphere while the roughing pump is still running. A metal wool foreline trap (Kurt Lesker Part Number TAR4CS100QF) was selected as an oil trap (23). The oil trap is attached to the inlet of the mechanical roughing pump (9) to prevent pump oil backflow into the reactor chamber.

2.1.2.2 Microwave Power Supply and Waveguide/Transmission System

The microwave power system designed for DS6 is shown schematically in Figure 2.7. A Cober S6F 2.45 GHz, 6 kW microwave power supply (1) was salvaged from a previous experimental setup. The microwave power supply houses a magnetron (2), circulator (3) and a dummy load (4). The 2.45 GHz microwave radiation passes through a dual-direction power coupler (5) and into rigid single mode microwave waveguide (6). The dual-direction power coupler (5) senses the forward power level, which is measured by the forward power meter (7). In the case of a tuning mismatch, power reflected back is also sensed and measured by the reverse power meter (8). The reverse power incident on the circulator (3) is directed into the dummy load (4), where it is dissipated as thermal energy. The forward power leaving the rigid waveguide (6) passes through a flexible waveguide piece (9) (Gerling Applied Engineering Part Number GA2104), and then enters the transition unit (10). The transition unit is a waveguide adapter that transitions from WR284 to EIA 1-5/8-inch coaxial, with a UG584/U



(1) Cober 2.45 GHz, 6 kW Microwave Power Supply

Figure 2.7 Schematic illustration of the microwave power supply and waveguide/transmission system designed for DS6

flange (Gerling Applied Engineering Part Number GM4028-184). The coaxial waveguide (11) attaches to the transition unit with a 1-5/8-inch silver solder swivel flange (Electronics Research Part Number RLA100-27). A TM_{013} mode is excited in the cavity (12), by the excitation probe (13), which can be tuned to minimize the reflected power by the sliding short (14) and by adjusting the height of the excitation probe. The cavity was custom built by the MSU Physics shop. The adjustable sliding short/ excitation probe/ coaxial waveguide assembly was custom built by Brian Wright of the MSU ECE Shop for this system. The bottom node of the excited TM_{013} mode is enclosed inside a quartz bell jar (15). This allows only one hemispherical-to-disk-shaped microwave plasma discharge (16) to be generated, directly above the sample stage. The quartz bell jar design is the same as is used in DS1 and other 2.45 GHz MSU-type diamond systems, and was custom made by Technical Glass Products, Inc., from the design shown in Figure 2.8.

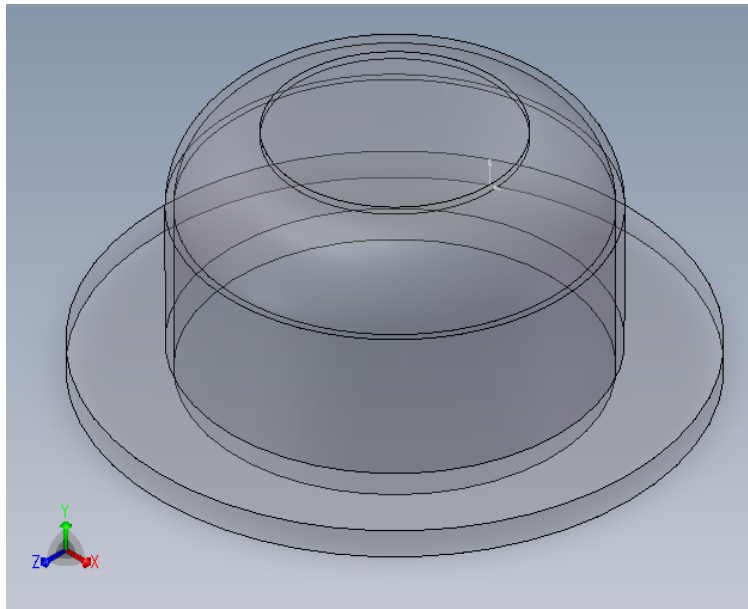


Figure 2.8 DS6 Quartz Dome

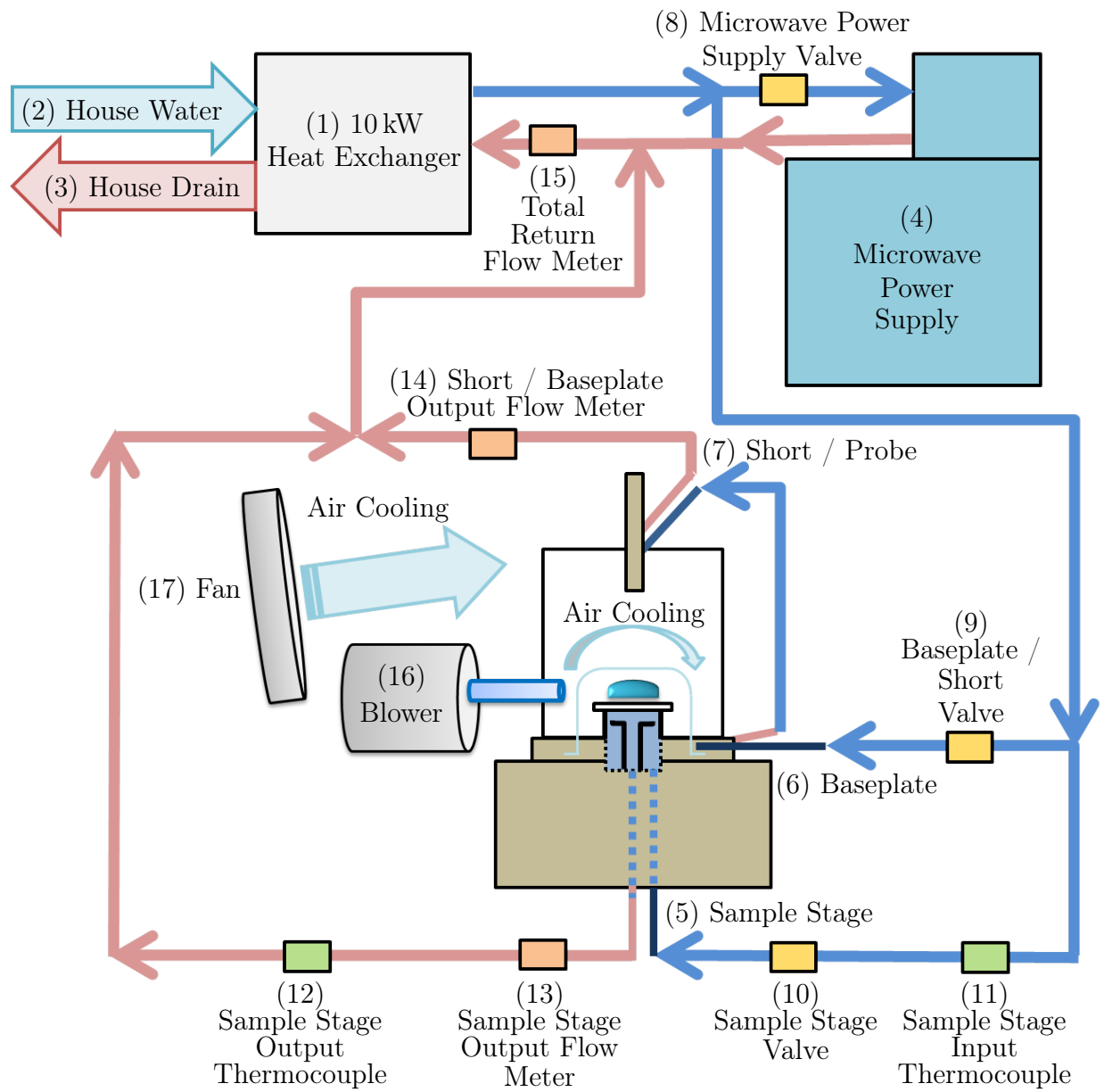


Figure 2.9 Schematic illustration of the cooling system designed for DS6

2.1.2.3 Cooling System

DS6 has been designed to allow for homoepitaxial diamond deposition in the high pressure regime above 150 Torr. The thermal load generated in this range requires a significant design effort to cool the system, which will be described in this section. The resulting cooling system for DS6 is shown schematically in Figure 2.9.

A Neslab HX300 recirculating process chiller (1) with a 10 kW cooling capacity at 20 °C was salvaged from a previous experimental setup. An already high load on the HVAC system in the laboratory necessitated that the thermal load be dissipated to a heat sink other than to the ambient air. The Neslab HX300 is a heat exchanger that uses an external coolant loop as the heat sink to cool a recirculating process loop. The current facility amenities in the laboratory do not include building-wide cooling water recirculation, so for this application house water (2) and the sewer drain (3) are substituted. The HX300 uses solenoid control to minimize wasted heat sink water. It is critical that the heat sink water be turned on and supplying adequate pressure to the HX300 before it is powered on. An attempt to recirculate the process loop without pressure from the house water supply results in an interlock that shuts down the compressor. If this interlock is triggered, the error can only be cleared by pressing a small black button on the back of the unit. The button can be accessed via a circular hole in the ventilation paneling, which is shown in Figure 2.10.

The Neslab 10 kW heat exchanger (1) supplies the cooling for both the microwave power supply (4) and the reactor. In the reactor, the critical components requiring cooling are the sample stage (5), the baseplate (6) and the microwave antenna short/probe assembly (7). The cooling loop splits into three separate branches, cooling the microwave power supply (4) and sample stage (5) individually, and the baseplate (6) and short/probe (7) in series. Each



Figure 2.10 This photograph, taken looking down the back of the Neslab HX300, shows the location of the reset button, circled in red, that will clear the interlock that is triggered if the heat exchanger is run without sufficient water pressure from the house water line.

of these branches can be individually throttled or shut off completely, using the microwave power supply valve (8), baseplate/short valve (9) or sample stage valve (10). The cooling water temperature is measured before and after the sample stage (5) by the sample stage input thermocouple (11) and sample stage output thermocouple (12). This allows for the possibility of setting interlocks, and for monitoring the thermal load of the sample stage. Three flow meters are also included, the sample stage output flow meter (13), short/baseplate output flow meter and total return flow meter (15). These were also included in the design to allow for monitoring, to ensure that the reactor and sample stage flow rates are sufficient and that the cooling water is returning to the heat exchanger (1), and not, for example, being lost to a large leak or broken connection. The microwave power supply (4) has its own internal cooling water flow interlocks and therefore does not need a separate flow meter for the microwave power supply branch.

Additional cooling is provided by the blower (16) and the fan (17). The blower supplies

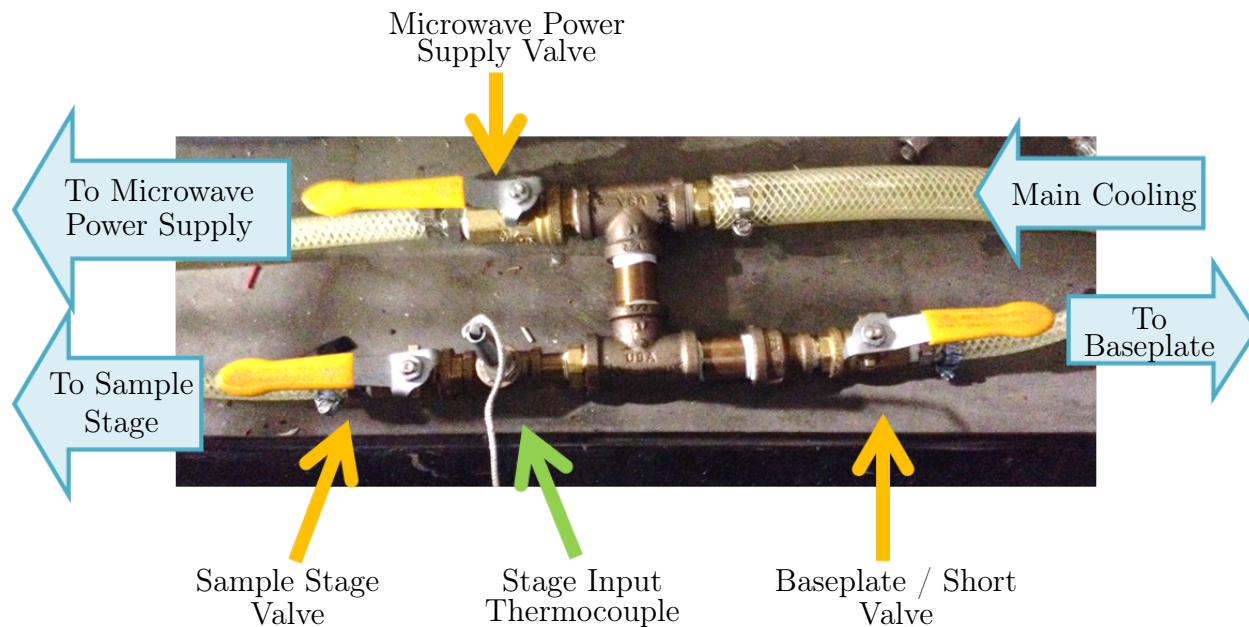


Figure 2.11 Input connections of the cooling system designed for DS6

cooling air over and around the quartz dome. The fan is a large industrial fan, such as a 20-inch 3,670 cubic foot per minute (CFM) Air King model. It supplies additional cooling air to the outside of the reactor cavity.

The microwave power supply (4) uses 1/2-inch inner diameter (ID) cooling lines, and the reactor cooling branches use 1/4-inch ID lines. To minimize the number of pipe fitting connections, the input and output connections were each grouped into a single rigid connection unit joined by NPT connections. The input connections are shown in Figure 2.11 and the output connections are shown in Figure 2.12. The cooling lines that run into these connection units are clear, high-pressure tygothane polyurethane tubing lines (McMaster Carr Part Numbers 5439K23, 5439K21), connected to the NPT fitted elements by barbed fittings. The valves in the input connection unit are brass ball valves (McMaster Carr Part Numbers 47865K41 and 47865K43). The stage input and output thermocouples are immersion pipe probes (Omega Engineering Part Number TC-K-NPT-G-72). The flow meters are extended

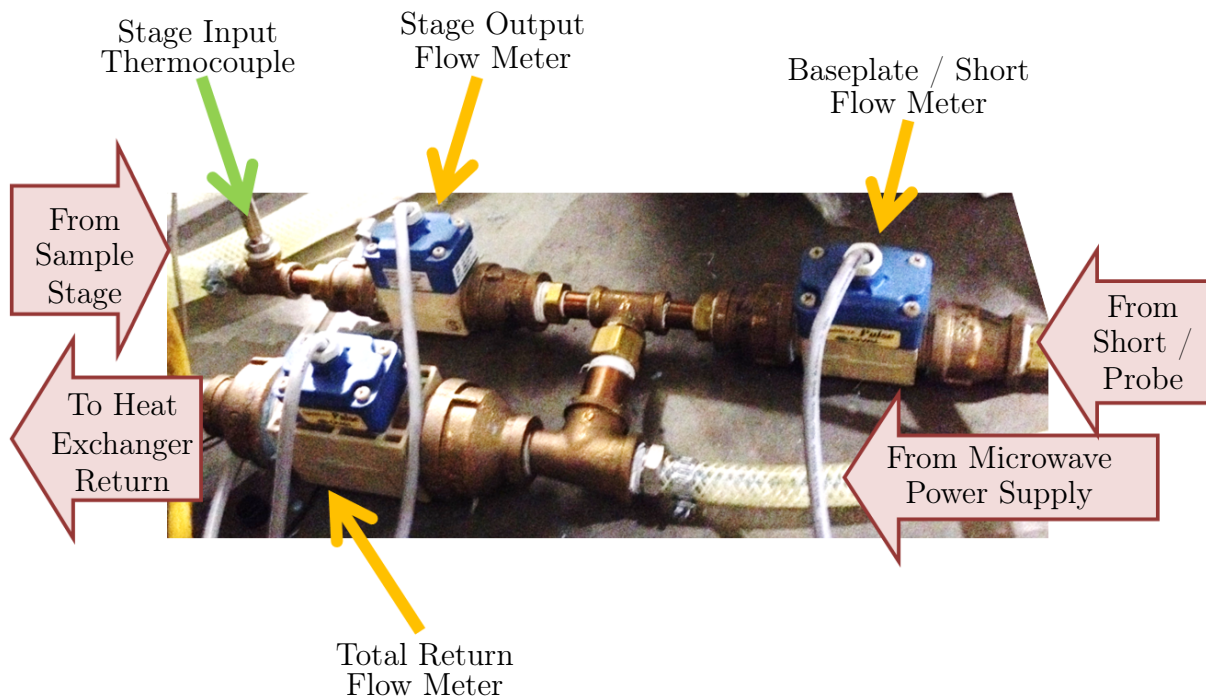


Figure 2.12 Output connections of the cooling system designed for DS6

life flow meters that work by creating vortices proportional to the velocity of the cooling water. The total return flow meter has a maximum 35.1 gallon per minute (GPM) flow rating (McMaster Carr Part Number 3437K64), and the other two flow meters have maxima of 11.4 GPM (McMaster Carr Part Number 3437K63).

The cooling stage was fabricated by the MSU Physics machine shop, using the same design as in DS1 [48]. The cooling stage design is shown in Figure 2.13. A quartz ring sits in the channel in the cooling stage, and the diameter of the channel was selected to match the quartz rings that were custom cut from a longer quartz cylinder for DS6 by the MSU Chemistry glass blowing shop. The quartz tube design is shown in Figure 2.14.

To allow for an optimized gas return path, a molybdenum substrate holder with a circular gas flow regulation pattern around the perimeter was fabricated. The MSU Physics machine shop fabricated the four-inch diameter molybdenum piece according to the design shown

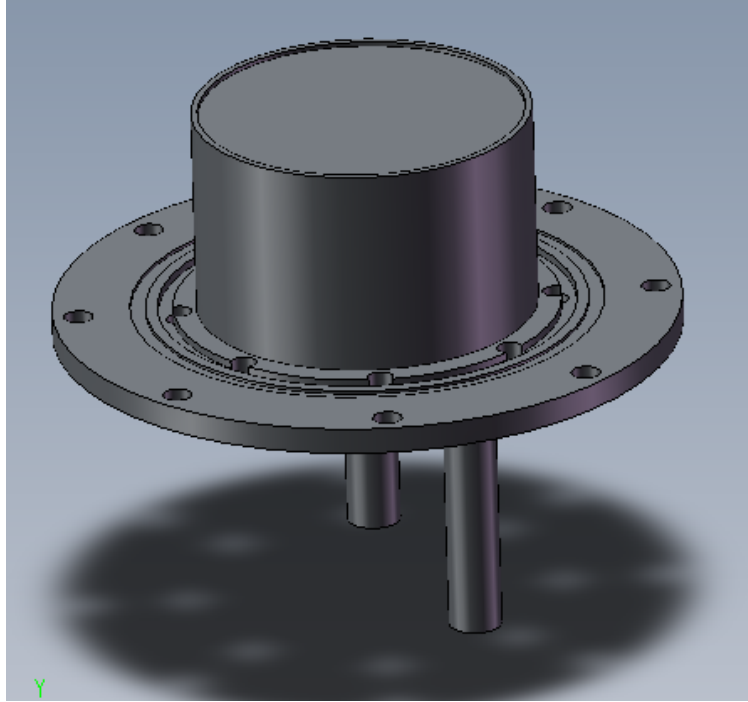


Figure 2.13 DS6 Water Cooled Stage

in Figure 2.15. The piece was fabricated from a $0.1875'' \times 12'' \times 4''$ molybdenum plate, purchased from Ed Fagan. The design of this large substrate holder piece is the same as the one used in DS1. This holder piece sits directly on top of the cooling stage, preventing the stainless steel cooling stage surface from being directly exposed to the growth plasma, and acts as a thermal interface layer.

2.1.3 Measurement of Experimental Output Variables

The sample temperature during deposition and the grown diamond thickness are both important output variables of the CVD process. The method for the measurement of the sample temperature will be described in Section 2.1.3.1. The determination of the grown thickness will be discussed in Section 2.1.3.2.

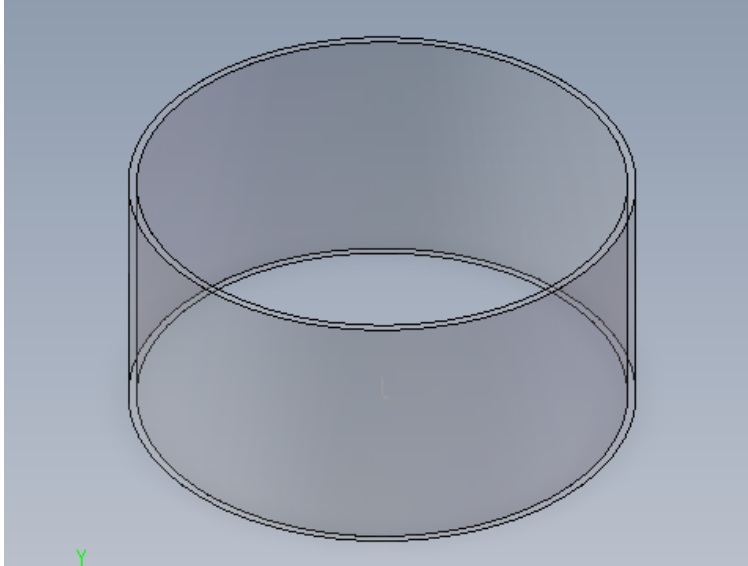


Figure 2.14 DS6 Quartz Tube

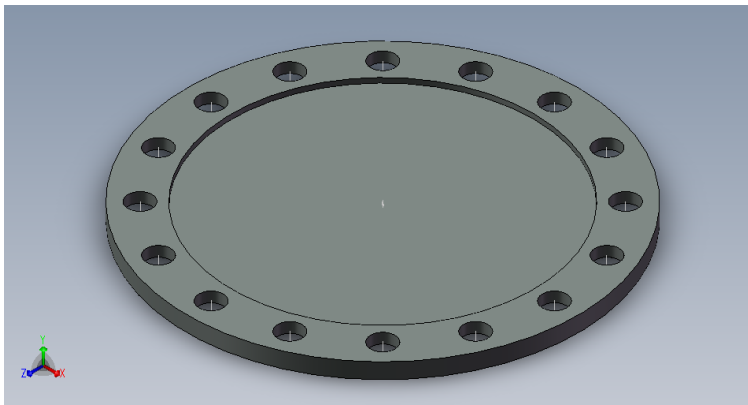


Figure 2.15 DS6 Molybdenum 4 inch Sample Holder

2.1.3.1 Sample Temperature During Deposition

Sample temperature during deposition is measured by one-color optical pyrometer. During the temperature measurement, the handheld pyrometer is focused across many points on the sample surface, and a number of readings are taken. The highest repeatable measurement taken while in focus on the sample surface is used as the temperature result. Measurements taken this way show good stability and repeatability, and are not subject to the inconsistencies associated with a fixed pyrometer that can sometimes move or lose focus during a long

deposition. It is expected that the effect of taking the measurement partly through the bottom edge of the plasma ball does not contribute significantly to the measured temperature, since measuring the temperature of the holder next to the sample through the plasma ball yields a temperature below the detection threshold.

2.1.3.2 Grown Thickness and Growth Rate

Sample thickness is measured using a Solartron Metrology Linear Encoder (Model DR600) at several locations in the sample center. This is the most relevant thickness, since the center is the region exposed for Fourier Transformed Infrared (FTIR) transmission spectroscopy characterization, which is used for boron concentration determination, as will be described in Section 2.2. The thickness at the corners is measured at several spots at each corner and given as an average over all four corners. When a total thickness is given, it is measured as an average over several measurements at the center and several at each of the four corners.

To determine the growth rate, the grown thickness, typically at the center, is divided by the total reactor growth time. The growth time is counted from the point when the reactor has reached deposition pressure, and the CH₄ flow is started.

Depending on the roughness of the sample surface, there can be a significant uncertainty in the thickness measurement. The error can be minimized by taking multiple measurements, however this method of thickness determination still has an error of approximately $\pm 2 \mu\text{m}$.

2.2 Fourier Transformed Infrared Spectroscopy

The infrared transmission spectra of a number of films grown in this work, over a range of B/C ratios in the plasma feedgas are shown in Figure 2.17. The transmittance, T , on

the y -axis in Figure 2.17 is the percentage of incident light that is transmitted through the sample. Transmittance is therefore given by $T = I/I_0$, where I_0 is the incident radiation and I is the radiation transmitted through the sample. The upper limit of the transmission is not 100% as might be assumed, since some of the incident light is reflected. The Fresnel equations give the reflectivity of a surface from the refractive indices and the incidence angle. For normal incidence this reduces to the relationship given in Equation (2.1), where R is the reflectivity (or percentage reflected), n_1 is the index of refraction of material the light passes from and n_2 is the index of refraction of the material the light passes into (if it is not reflected). For diamond, which has a high refractive index of approximately 2.38 in the IR range, this gives a reflectivity of $R = 0.1667$ for light entering from air.

$$R = \left| \frac{n_1 - n_2}{n_1 + n_2} \right|^2 \quad (2.1)$$

The value of 16.67% reflection obtained from Equation (2.1) would seem to indicate that the maximum transmission value would be $T = 1 - R = 83.33\%$, however there is another diamond/air interface the light must pass through before passing into a detector, as shown in Figure 2.16. Equation (2.1) also holds at this interface, and an additional 13.89% is reflected back into the sample, and only 69.44% is transmitted. The actual maximum T value is actually over 71% however, as shown in Figure 2.16, because of repeated reflection and transmission at the two interfaces. After the 13.89% is reflected from the back interface, an additional 11.58% is transmitted through the front interface, and the remaining 2.32% is reflected back. The 2.32% transmits an additional 1.93% through the back interface, which contributes to the transmission from the first pass through the sample. This continues, and the repeated reflection and transmission contributions become negligibly small. These total

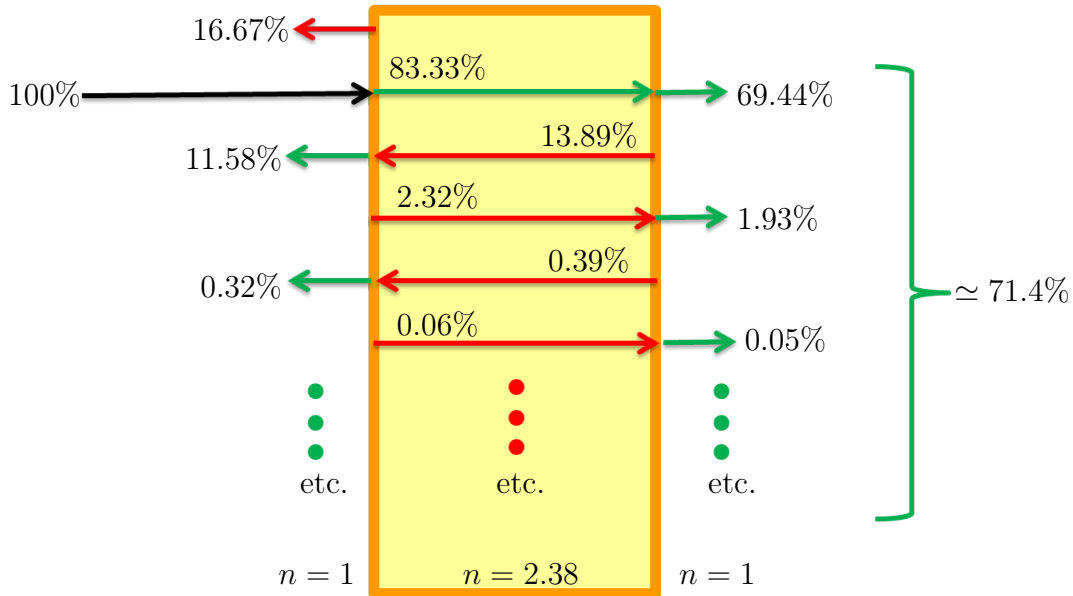


Figure 2.16 Illustration of the total transmission percentage through diamond, with an index of refraction $n = 2.38$, in air with $n = 1$

contributions to the transmission sum to approximately 71.4%, which is why the maximum transmission percentage on the y -axis of an IR transmission spectrum for a diamond sample is approximately 71%.

The 71.4% obtained in the preceding analysis can also be more expediently computed using the relationship of Equation (2.2), which gives the total transmission for a plate in air for the case of multiple reflections.

$$T_{\%} = \frac{2n}{n^2 + 1} \cdot 100\% \quad (2.2)$$

2.2.1 Infrared Analysis of Lightly Boron Doped Diamond

The analysis of diamond by infrared spectroscopy began shortly after Custers [74] first discovered in 1952 that some type II diamonds were also semiconductors, and classified this

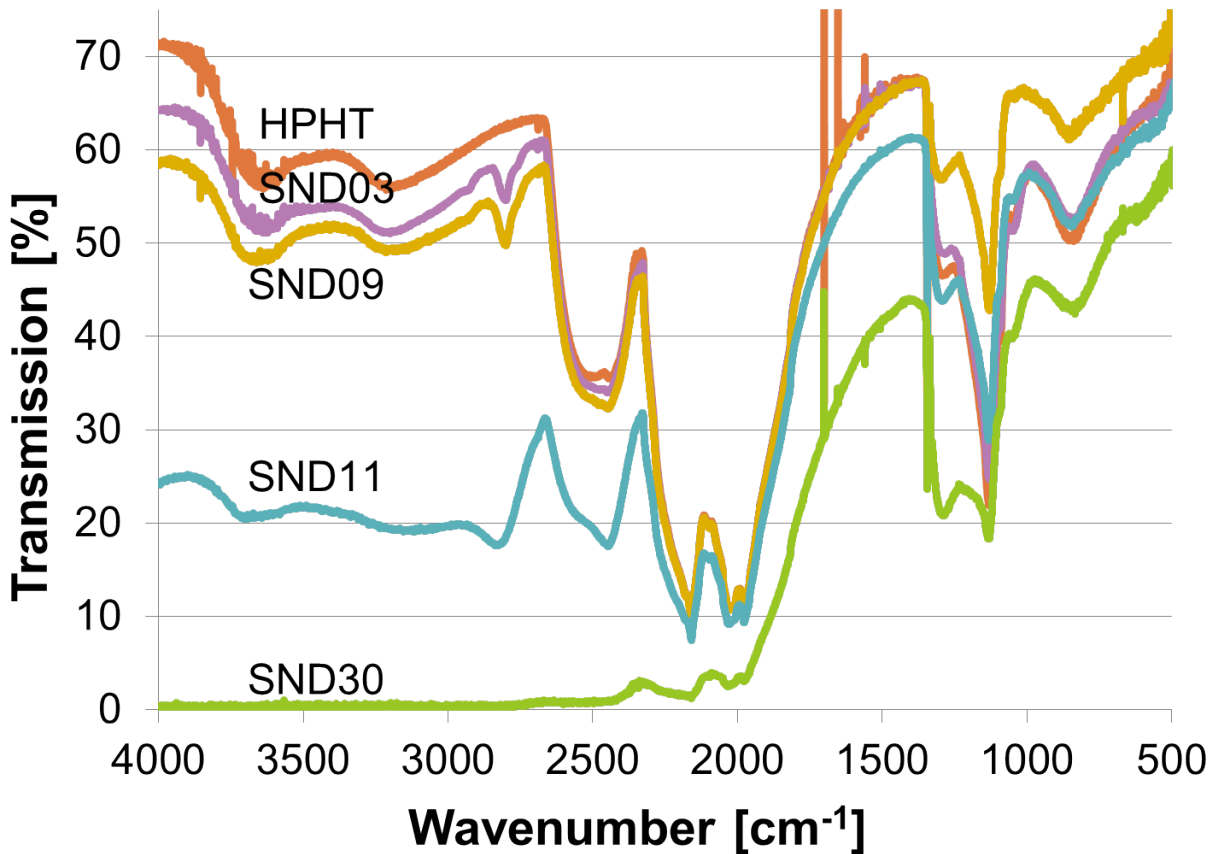


Figure 2.17 Fourier transformed infrared transmission spectrum of doped diamond films on HPHT substrates. The top sample is an HPHT substrate prior to boron doped diamond deposition, the remaining samples were deposited in DS1, with the following B/C concentrations in the plasma feedgas: SND03 - 2.5 ppm, SND09 - 12.5 ppm, SND11 - 500 ppm, and SND30 - 2000 ppm. The deposition conditions for these samples are discussed in greater detail in Chapters 3 and 4.

new group of diamonds as “type IIb.” Following this discovery, the electrical and optical properties of these type IIb natural diamonds were studied by several groups in the 1950s [75, 76, 77, 78, 79, 80] . For example, Clark, Ditchburn, and Dyer [79] were among the first to find and classify a number of peaks in the infrared absorption spectrum of Earth-mined type IIb diamonds that did not appear in type I or type IIa diamond samples. A series of three absorption features at 0.305, 0.347 and 0.363 eV were found to be associated with the acceptor center in these naturally semiconducting diamonds by Wedepohl [80], who found a

particularly strong correlation between the feature at 0.347 eV and the number of vacant acceptor levels.

The electrical activation energy of lightly boron doped diamond, as will be discussed in greater detail in Section 2.4, is close to the energy corresponding to the strongest infrared absorption feature in type IIb diamonds, at 0.347 eV. The implication of this correlation is that the absorption is due to the excitation of electrons from discrete levels just above the valence band into vacant acceptor levels. For this to be the case, the total amount of absorption occurring would be proportional to the total number of vacant acceptors. The vacant acceptors are those that are unionized and uncompensated by donor atoms. For such a high activation energy, only a negligible fraction of acceptors are ionized at room temperature in lightly boron doped diamond. Therefore at room temperature the density of vacant acceptors can be taken to be $N_A - N_D$. Austin and Wolfe [77] and Wedepohl [80] both studied the temperature dependent integrated area of the 0.347 eV absorption peak and the temperature dependent density of vacant acceptor levels. If the transition probability were constant, then the integrated absorption would be directly proportional to the number of vacant acceptor levels (given by $N_A - N_D - p$) at any temperature. Both studies found that at room temperature the integrated absorption could approximate $N_A - N_D$. At higher temperatures however, these early studies found that the absorption was more temperature dependent than the density of vacant acceptor levels, and so the temperature dependence of the absorption is more complicated than just a simple model based on constant transition probability. (The FTIR measurements taken in this work, however, are all taken at room temperature ($\sim 25^\circ\text{C}$), and so the correlation between integrated area and $N_A - N_D$ is valid for lightly doped samples.)

Collins and Williams [81] investigated the integrated area and uncompensated acceptor

concentration of five natural diamonds as a part of a study that proved conclusively that it was boron and not aluminum that was responsible for the semiconducting activity in natural type IIb diamonds. The vacant acceptor concentrations and the integrated areas of the 2800 cm^{-1} ($\simeq 0.347\text{ eV}$) absorption peaks, I_{2800} , are shown in Figure 2.18. Fitting a line to this data, as shown in Figure 2.18, gives a relation between I_{2800} and $N_A - N_D$, measured at room temperature on type IIb samples. For peaks integrated on a wavenumber (cm^{-1}) energy axis and an absorption coefficient axis in cm^{-1} , this relationship is given by Equation (2.3).

$$[N_A - N_D](\text{cm}^{-3}) = 8 \times 10^{17} I(2800\text{ cm}^{-1}). \quad (2.3)$$

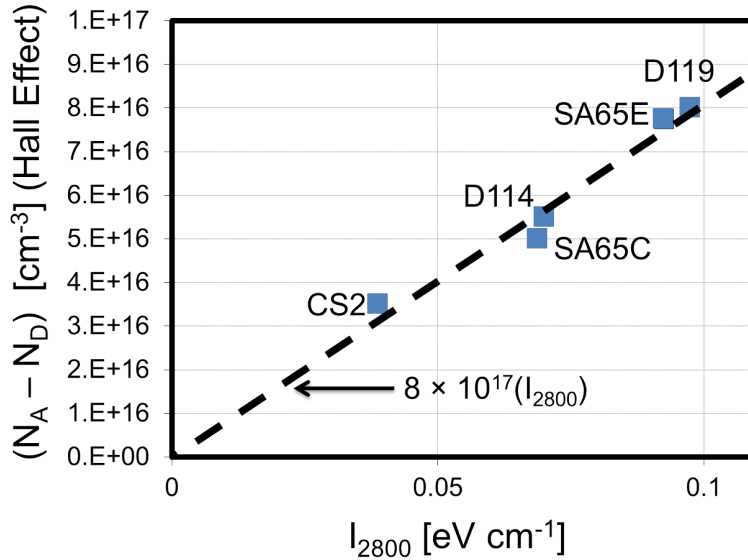


Figure 2.18 Collins and Williams [81] studied the integrated area under the 2800 cm^{-1} absorption feature (I_{2800}) and hall effect data to determine the vacant acceptor concentrations in natural type IIb diamonds. The sample numbers given in that work are shown next to the relevant data points. A linear fit to this data, as shown on this plot, gives $N_A - N_D = 8 \times 10^{17}(I_{2800})$

The Beer-Lambert law describes the relationship between the transmission T and the

base- e (Napierian) absorption coefficient α , as given in Equation (2.4), where t is the distance into the material, which in the case of transmission spectroscopy is taken to be the sample thickness.

$$T = e^{-\alpha t} \quad (2.4)$$

The calculation of the integrated area in Equation (2.3) requires selecting an appropriate baseline from which to calculate the area of the absorption feature. In this work the baseline is drawn in the transmission spectrum, and then the absorption coefficient is determined using Equation (2.5), where α is the absorption coefficient, T_{doped} is the transmission spectrum of the boron doped diamond, T_{baseline} is the straight line baseline drawn on the doped spectrum under the 2800 cm^{-1} absorption feature, and t is the thickness in cm. The thickness is taken to be the grown thickness of the boron doped layer, since the relevant absorption by the boron acceptors is assumed to take place only in this layer, and not in the undoped homoepitaxial substrate.

$$\alpha = \frac{-\ln\left(\frac{T_{\text{doped}}}{T_{\text{baseline}}}\right)}{t} \quad (2.5)$$

Figure 2.19 shows the conversion from the transmission spectrum to absorption coefficient for sample SND03. The integrated area under the resulting absorption coefficient vs. energy curve is then used to determine the uncompensated acceptor concentration in the sample using the relationship in Equation (2.3) [81].

The estimation of the boron concentration using Equation (2.3) has several limitations. The resolution of the 2800 cm^{-1} peak in the absorption coefficient spectrum sets a lower limit on the detectable boron concentration as a function of the thickness of the grown

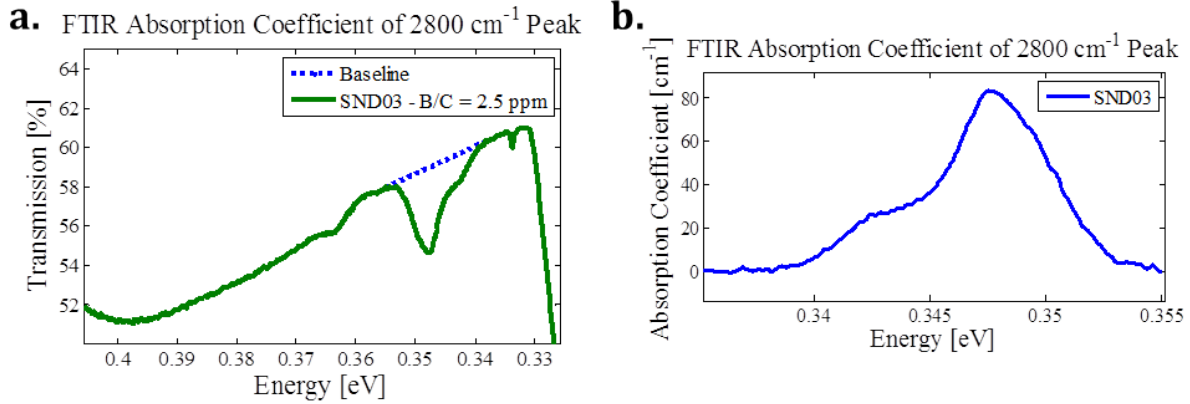


Figure 2.19 Baseline calculation for the determination of the integrated area of the 2800 cm^{-1} feature. (a) the baseline drawn on the transmission spectrum of sample SND03 (b) the resulting absorption coefficient vs. energy plot obtained using Equation (2.3)

film, due to the film thickness dependence in Equation (2.5). If the 2800 cm^{-1} peak is not resolvable, a sample's boron concentration can only be estimated to the upper limit of the boron concentration based on the thickness of the film. That limit is estimated in Figure 2.20.

There is also an upper limit on the boron concentration measurable with the calibration of equation Equation (2.3), which is given at the extreme upper limit by the increasing absorption due to photoionization, which causes the transmission to drop toward zero. Samples such as SND30, as shown in Figure 2.17, are therefore above the detection limits by this method. Before this extreme is reached, however, the absorption feature broadens, as seen in the example of SND11, making baseline determination increasingly inaccurate. The widening of the 2800 cm^{-1} peak has been attributed to overlapping of the wave functions of neighboring centers that induce a broadening of the impurity band energy [82]. As a consequence, the calibration of Equation (2.3) is best applied for boron concentrations in the range of 10^{16} to 10^{18} cm^{-3} .

The use of infrared spectroscopy to estimate the boron concentration of diamond samples outside of the concentration range of 10^{16} to 10^{18} cm^{-3} has unfortunately resulted in some

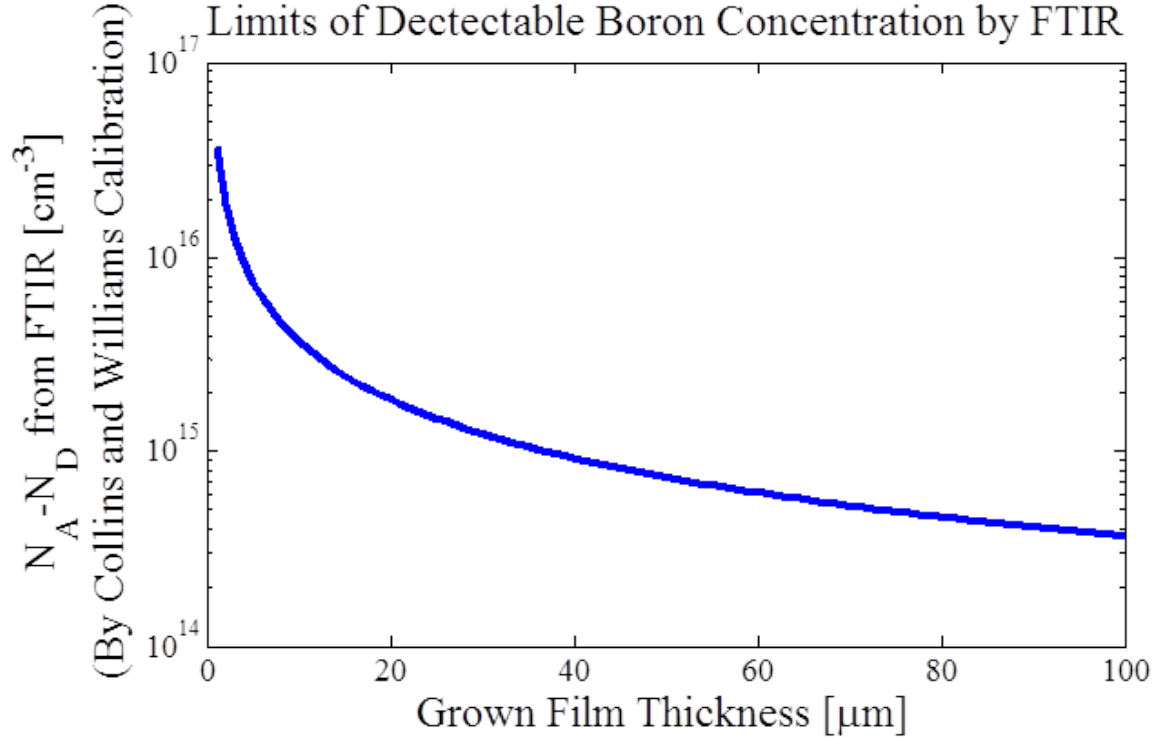


Figure 2.20 An estimate of the thickness dependent lower limit resolvable for measuring the integrated area I_{2800} in Equation (2.3)

confusing relationships in the literature. In this work, the calibration of Davies, which will be described in Section 2.2.2.4, is used to estimate the boron concentrations of heavily doped samples. This calibration and other methods that have been used in the literature to measure samples with boron concentrations above 10^{18}cm^{-3} will be reviewed in Section 2.2.2.

2.2.2 Infrared Analysis of Heavily Boron Doped Diamond

2.2.2.1 Chrenko Calibration

The advent of laboratory grown diamonds made it possible to study diamonds with higher concentrations of boron than what naturally occurs in the extremely rare Earth-mined type IIb diamonds. In 1973 Chrenko [83] published a study of laboratory grown diamonds, including more heavily doped ones, in which the infrared absorption characteristics were related to the

uncompensated acceptor concentrations. Chrenko used a method of determining the value of I_{2800} that differed from the method of integrating an area under the absorption coefficient vs. wavenumber graph that Collins and Williams [81] had reported. The spectrometer Chrenko used output the absorbance A plotted onto paper. The difficulties in working with a paper plot made it more convenient to simply measure the height of the absorption peak and use this to approximate the integrated absorption, rather than calculating the actual area under the peak. The relationship between the absorbance A and the transmission T is given in Equation (2.6).

$$A = -\log_{10}(T) \quad (2.6)$$

To use Collins and William's calibration, as given in Equation (2.3), Chrenko needed to find the equivalent of the integrated area I_{2800} from a plot of absorption coefficient α , not absorbance A . As given in Equation (2.4), $\ln(T) = -\alpha t = \log_e(T)$. A logarithmic base conversion was therefore needed, as given in Equation (2.7)

$$\log_e(T) = \frac{\log_{10}(T)}{\log_{10}(e)} = \frac{\log_{10}(T)}{0.43429} = 2.302(\log_{10}(T)) = 2.302A \quad (2.7)$$

Using the base conversion in Equation (2.7) gives Chrenko's conversion of $\Delta\alpha = 2.3\Delta A/t$, where t is the thickness of the crystal. Having converted from absorbance to absorption coefficient, Chrenko then used an approximation to estimate I_{2800} . Chrenko claimed that $I/\Delta\alpha = 0.85 \times 10^{-2} \pm 20\%$, and used this conversion to obtain an approximate value for I_{2800} .

For some of the crystals Chrenko examined, the boron concentration was too high to accurately determine a baseline, a problem that was previously described in Section 2.2.1. For

these samples, Chrenko instead examined a “correlated band” at 1290 cm^{-1} , and converted the $\Delta\alpha$ measured at 1290 cm^{-1} (α_{1290}), to an equivalent $\Delta\alpha$ at 2800 cm^{-1} (α_{2800}) which Chrenko claimed could be done with the relationship given in Equation (2.8).

$$(\alpha_{2800})/(\alpha_{1290}) = 22 \pm 20\% \quad (2.8)$$

With a method to determine I_{2800} for both lightly doped and heavily doped samples, Chrenko then claimed to use the calibration curve in Collins and Williams, presumably the same calibration as given in Equation (2.3). Combining the terms from this method, the total conversion factor Chrenko has then reported to have used to get from α_{1290} to the approximate boron concentration is therefore given by Equation (2.9). This is actually quite close to the calibration of Davies, which will be discussed in Section 2.2.2.4.

$$\begin{aligned} [B](\text{cm}^{-3}) &= (8 \times 10^{17})I_{2800} = (8 \times 10^{17})\left((0.85 \times 10^{-2})(\alpha_{2800})\right) \\ &= (8 \times 10^{17})(0.85 \times 10^{-2})\left((22)(\alpha_{1290})\right) = 1.496 \times 10^{17}\alpha_{1290} \quad (2.9) \end{aligned}$$

One issue in interpreting the usage of Chrenko’s calibration of Equation (2.9) is that in [83], Chrenko reported the value of the equivalent I_{2800} in a confusing way. The interpretation of the values reported in Chrenko’s work requires a conversion factor, since Chrenko uses atomic [ppm] rather than the more common $[\text{cm}^{-3}]$ as the unit for the acceptor concentration. With a lattice constant of 3.56683 \AA , and 8 atoms per unit cell, diamond has an atomic density of $1.76296 \times 10^{23}\text{ cm}^{-3}$, and so the conversion factor from [ppm] to $[\text{cm}^{-3}]$ is therefore given by Equation (2.10).

$$(N_A - N_D)[\text{cm}^{-3}] = ((N_A - N_D)[\text{ppm}])(1.76296 \times 10^{17} \text{ cm}^{-3}/\text{ppm}) \quad (2.10)$$

Chrenko [83] reports in a table the integrated area I_{2800} in $[\text{eV cm}^{-1}]$ and the estimated $(N_A - N_D)$ in [ppm]. This data is shown for four of their samples in the third and fourth columns of Table 2.1. Using the conversion factor in Equation (2.10), the $N_A - N_D$ values in [ppm] in the fourth column of Table 2.1 have been converted to cm^{-3} in the second column of that table. By contrast, if the I_{2800} values had been multiplied by the 8×10^{17} calibration of Collins and Williams, as given in Equation (2.3), the values given in the fifth column of Table 2.1 would have been obtained instead.

Sample	$(N_A - N_D)$ [cm^{-3}]	I_{2800} [eVcm^{-1}]	$(N_A - N_D)$ [ppm]	8×10^{17} cal. [cm^{-3}]
Chrenko				
52	7.4×10^{15}	0.94×10^{-2}	0.04	7.52×10^{15}
48	6.52×10^{16}	6.5	0.37	5.2×10^{18}
43	6.7×10^{17}	78	3.80	6.24×10^{19}
60	8.11×10^{17}	87	4.60	6.96×10^{19}

Table 2.1 $N_A - N_D$ data reported in Chrenko [83] compared to the 8×10^{17} relationship derived from Collins and Williams [81]. The data in the third (I_{2800}) and fourth ($N_A - N_D$ [ppm]) columns are given exactly as presented in a table in [83]. The second column ($N_A - N_D$ [cm^{-3}]) is calculated using Equation (2.10). For comparison, if the I_{2800} values as given in [83] had been multiplied by the 8×10^{17} calibration from Collins and Williams, the values in the fifth column (8×10^{17} cal.) would have been obtained for these samples instead.

Table 2.1 shows that the $N_A - N_D$ [ppm] values, as they are reported in Chrenko's work [83], were not obtained by multiplying the reported I_{2800} values by the calibration of Equation (2.3) and then converting the $N_A - N_D$ [cm^{-3}] values to [ppm] using Equation (2.10). The confusion seems to have been caused by the " $\times 10^{-2}$ " that appears after the I_{2800} value for Chrenko's sample 52, but not for any of the other samples. Assuming that the values for the other samples should also have been multiplied by 10^{-2} , however, does give the expected

relationship. The I_{2800} values, modified by multiplying all of the samples by the 10^{-2} factor, then fall onto the 8×10^{17} calibration line, as shown in Figure 2.21.

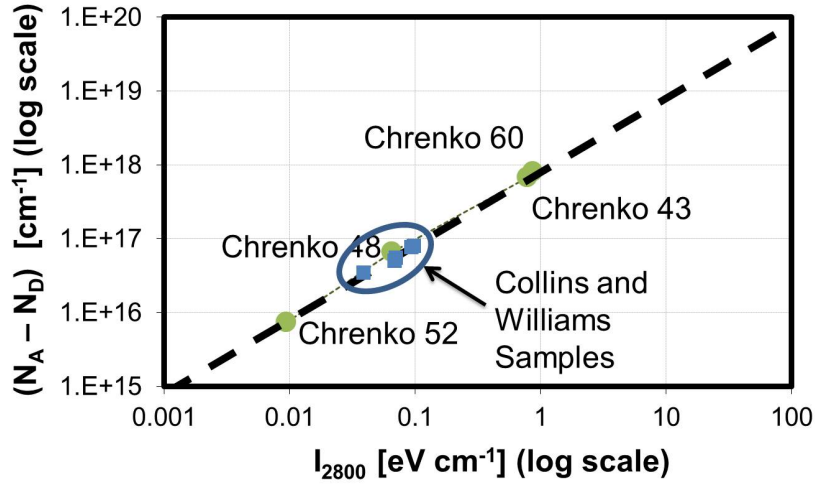


Figure 2.21 The $N_A - N_D$ [cm⁻³] and I_{2800} data from Table 2.1 has been modified by multiplying the reported I_{2800} data by 10^{-2} for all of the samples, and not just sample 52, as discussed in the text. The extrapolated calibration curve line of $N_A - N_D = 8 \times 10^{17}(I_{2800})$ and the samples from Collins and Williams [81] are also shown for reference.

Due to initial difficulties in interpreting Chrenko's confusing presentation of the I_{2800} data and because a survey of the literature has not yielded any confirmation of their method with other methods of boron concentration determination, the Chrenko calibration will not be used in this dissertation work.

2.2.2.2 Burns Calibration

In an investigation of the different optical properties of growth sectors with $\{110\}$, $\{113\}$, $\{100\}$ and $\{111\}$ orientations, Burns *et al.* [84] also examined the infrared absorption related the boron acceptor. Burns *et al.* used the Collins and Williams calibration of Equation (2.3) to estimate the boron concentration for regions of their samples where an appropriate baseline could be drawn on the 2800 cm^{-1} feature. However, as described in Section 2.2.1, the feature

broadens with increasing boron concentration, and the determination of a baseline becomes increasingly inaccurate.

Burns *et al.* determined a fit between the absorption coefficient at 3050 cm^{-1} (α_{3050}) and I_{2800} for their samples that were less highly doped. The relationship they found is given in Equation (2.11).

$$N_A - N_D = \frac{\alpha_{3050}}{21.4 \left[\frac{\text{cm}^{-1}}{\text{ppm}} \right]} = 0.047 \left[\frac{\text{ppm}}{\text{cm}^{-1}} \right] \alpha_{3050} = 8.24 \times 10^{15} \left[\frac{\text{cm}^{-3}}{\text{cm}^{-1}} \right] \alpha_{3050} \quad (2.11)$$

Gheeraert *et al.* found similar results to the calibration of Equation (2.11) for boron concentrations lower than $4.6 \times 10^{18} \text{ cm}^{-3}$. The absorption coefficient at 3050 cm^{-1} is in essence a measure of the photoionization, which is related to the boron content. However, for samples doped above about 10^{19} cm^{-3} , the transmission T around 3050 cm^{-1} drops toward zero due to this photoionization, as previously discussed in Section 2.2.1. This makes the useful range for the calibration of Burns *et al.* extremely narrow, perhaps in the range of $5 \times 10^{17} \text{ cm}^{-3}$ to $5 \times 10^{18} \text{ cm}^{-3}$. The calibration of Equation (2.11) will therefore not be used in this dissertation work.

2.2.2.3 Novikov Calibration

In a 2007 publication investigating heavily boron doped HPHT grown diamonds, Blank *et al.* [85] estimated the uncompensated acceptor concentration ($N_A - N_D$) using infrared absorption spectroscopy. As previously discussed in Section 2.2.1, the transmission T drops toward zero around the 2800 cm^{-1} absorption feature as the doping increases, and so a calibration involving a measurable part of the infrared spectrum is needed to analyze heavily

doped samples. Blank *et al.*, like Chrenko [83], as previously discussed in Section 2.2.2.1, used a calibration with the absorption coefficient at 1290 cm^{-1} . The calibration they used is given in Equation (2.12).

$$[N_A - N_D] \approx 1.6 \times 10^{17} \alpha_{1290} \quad (2.12)$$

The calibration of Equation (2.12) was cited in Blank *et al.* [85] to the source, “N. V. Novikov et al., Physical Properties of Diamond, Naukova Dumka, Kiev, 1987 in Russian.” A search for that work found [86], a 188 page handbook written in Russian, titled “Физические свойства алмаза” which translates to “Physical Properties of Diamond.” It was published in 1987 in Kiev, by Naukova Dumka, and was edited by N.V. Novikov. On pg. 117 of that work, in a section on type IIb diamond, the relationship of Equation (2.13) is given with a citation to the work of Malogolovets [87]. The work of Malogolovets, a conference submission titled “Примесный бор в монокристаллах синтетического алмаза,” which translates to “Boron impurity in synthetic diamond monocrystals,” was presented at the International Workshop “Superhard Materials” that took place in Kiev June 17-21, 1981. Presumably data was presented in that work that led to the calibration of Equation (2.13), however it is extremely difficult to obtain a copy of it.

$$N_A - N_D = 0.70 \times 10^{16} \alpha_{2810} \simeq 1.6 \times 10^{17} \alpha_{1290} \pm 20\% \quad (2.13)$$

Assuming that $\alpha_{2810} \simeq \alpha_{2800}$, the Novikov calibration of $(N_A - N_D) = 0.70 \times 10^{16} \alpha_{2810}$ is very close to the relationship given by Chrenko [83] as discussed in Section 2.2.2.1 (which is $(N_A - N_D) = 0.68 \times 10^{16} \alpha_{2800}$, assuming that Chrenko used 8×10^{17} for the extrapolation of the calibration curve of Collins and Williams). The relationship in the Novikov calibration for the

α_{1290} absorption is also very close to that reported by Chrenko, which was $\simeq 1.5 \times 10^{17} \alpha_{1290}$, as given in Equation (2.9). This calibration is also quite close to the Davies calibration, which will be discussed in Section 2.2.2.4.

The Novikov calibration has been used for the estimation of the uncompensated acceptor concentration for heavily doped diamonds by other researchers in the literature, for example by Ramamurti *et al.* [51]. A search of the literature has not provided any studies confirming the Novikov calibration with another method of determining the acceptor concentration, such as Hall Effect or SIMS results, and therefore it will not be used in this dissertation work.

2.2.2.4 Davies Calibration

In a 1977 review of the optical properties of diamond, Gordon Davies [88] discussed the absorption of type IIb diamonds, dividing the infrared spectrum into three spectral regions:

1. Up to 165 meV ($= 1332 \text{ cm}^{-1}$, the Raman energy of pure diamond), where one-phonon absorption takes place.
2. From 300 to 370 meV ($= 2417$ to 2980 cm^{-1}) where the electronic states of the acceptor cause sharp line absorption features.
3. Above 370 meV where photoionization is the dominant effect.

The absorption feature at 1290 cm^{-1} is in the one phonon absorption range, and therefore caused by impurities which break the symmetry of the diamond lattice. Above boron concentrations of approximately 10^{18} cm^{-3} , the signal-to-noise ratio of the contribution due to the boron in the grown film becomes strong enough that an analysis of the 1290 cm^{-1} feature can be performed with an appropriate calibration to determine the boron content

of highly doped samples. The absorption coefficient at 1290 cm^{-1} is related to the boron concentration by the relationship in Equation (2.14) as given in [88].

$$[\text{B}](\text{cm}^{-3}) = 2.13 \times 10^{17} \alpha(1290\text{ cm}^{-1})(\text{units: cm}^{-1}) \quad (2.14)$$

In a study of the infrared absorption of $3\text{ }\mu\text{m}$ thick homoepitaxial diamond films grown on type Ib (100) substrates, Gheeraert *et al.* [82] confirmed that for boron doped diamond films with $[\text{B}] > 10^{18}\text{ cm}^{-3}$, the Davies relationship of Equation (2.14) gives boron concentrations very close to SIMS measurements. In a more recent work, Achard *et al.* [55] also found excellent correspondence between SIMS measurements and the relationship of Equation (2.14) for their freestanding heavily boron doped single crystal diamond samples.

As the heavily doped samples grown in this work have boron concentrations over $1 \times 10^{18}\text{ cm}^{-3}$, Equation (2.14) is expected to give an accurate estimate of the boron content, as has been demonstrated by these other groups [82, 55] for heavily boron doped samples. The FTIR transmission spectrum is first taken from the growth substrate prior to deposition, and then for the grown diamond film on the substrate after deposition. The absorption coefficient α is then determined using Equation (2.5), where T_{doped} is the transmission spectrum of the sample after growth, T_{baseline} is the transmission spectrum of that sample's undoped HPHT seed prior to deposition, and t is the film thickness, measured in cm. The assumption implicit in this method of calculating the absorption coefficient is that any change in the transmission spectrum is due to the grown diamond film, and therefore any new absorption takes place within the grown thickness.

2.3 Secondary Ion Mass Spectroscopy (SIMS)

Secondary Ion Mass Spectroscopy (SIMS) is a method for determining the atomic composition of a material. The sample under analysis is bombarded with ions, which sputters off the material. These ejected secondary ions are collected and then measured by a mass spectrometer. The concentration of impurities such as boron were measured by SIMS for several samples as a part of this work. These measurements were all performed in a commercial laboratory, EAG labs (www.eag.com).

2.4 Temperature Dependent Four Point Probe Measurements

Four point probe measurements are a convenient and straight-forward method of measuring resistivities. In a standard two-wire, or two point probe resistivity measurement, the voltage drop associated with the wiring and contact resistances are included in the measurement of the voltage drop across the sample. These contributions can be significant, and can be avoided by separating the current supplied and the voltage measured into two different pairs of electrodes, as shown in Figure 2.22. The outer two electrodes supply a current (I_{source}) and the inner two electrodes measure the resultant voltage drop (V_{sense}). The current in the voltage sensing electrodes is nearly zero, so the voltage measurement includes only the voltage dropped by the sample itself, which leads to very accurate measurements when correctly implemented.

Boundary conditions affect the measured ratio of the source current (I_{source}) and the interior voltage (V_{sense}). The effect can be compensated by a correction factor (C), to give

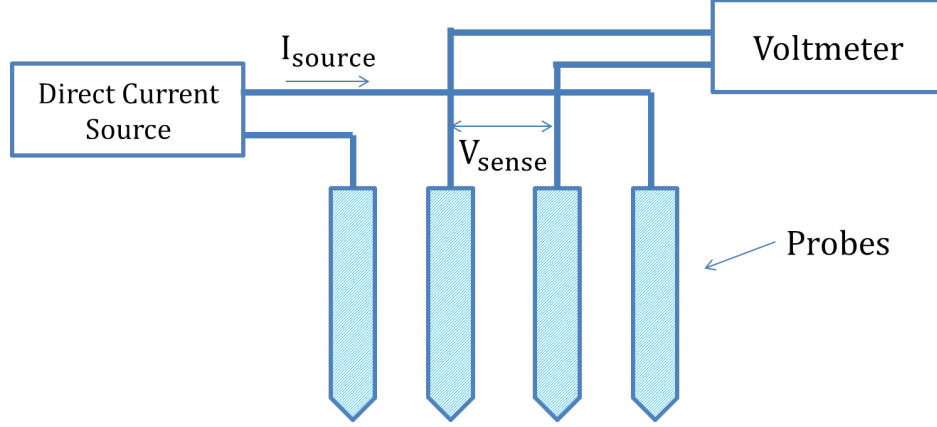


Figure 2.22 Diagram of a standard four point probe setup. *Adapted from [89]*

the correct sheet resistivity (ρ_{sheet}) for a given sample geometry according to Equation (2.15).

$$\rho_{\text{sheet}} = \frac{V_{\text{sense}}}{I_{\text{source}}} C \quad (2.15)$$

These correction factors (C) can be computed, and for most samples the correction factors can be estimated from the work of Smits [90], which gives a table of calculated correction factors for some common geometries.

The resistivity is a function of temperature, and the temperature dependent resistivity curve of a semiconductor sample gives additional information about dopants, including the activation energy, E_A [91]. Equation (2.16) gives the temperature dependence of the hole concentration p , where N_D is the total compensating donor concentration, N_A is the total acceptor concentration, k is the Boltzmann constant, A is a constant, T is the absolute temperature, and g_a is the degeneracy factor for the acceptor [92].

$$p^2 + pN_D = \frac{A}{g_a} T^{3/2} (N_A - N_D - p) \exp\left(\frac{-E_A}{kT}\right) \quad (2.16)$$

A low temperature approximation allows Equation (2.16) to be further simplified to the

relationship given in Equation (2.17).

$$p = \frac{A}{g_a} T^{3/2} \frac{N_A - N_D}{N_D} \exp\left(\frac{-E_A}{k T}\right) \quad (2.17)$$

To arrive at the relationship between T and the resistivity ρ , the relationship between ρ and the hole concentration p , given in Equation (2.18), can be used [92], where q is the electronic charge, and μ is the conductivity mobility.

$$\rho = \frac{1}{p q \mu} = \frac{1}{\sigma} \quad (2.18)$$

Equation (2.18) also includes the reciprocal relationship of the resistivity to the conductivity, σ . To follow the method of Lagrange *et al.* [91], using the conductivity relationship of Equation (2.18), Equation (2.17) can be rewritten, as given in Equation (2.19).

$$\sigma = q \mu \frac{A}{g_a} T^{3/2} \frac{N_A - N_D}{N_D} \exp\left(\frac{-E_A}{k T}\right) \quad (2.19)$$

For comparison with Lagrange *et al.* [91] let $A T^{3/2} = N_0 T^{3/2} = N_V$. N_V is the density of states in the valence band, given by Equation (2.20), where \hbar is the reduced Plank constant, and m^* is the effective mass which for diamond can be taken as $0.74m_0$ [93].

$$N_V = 2 \left(\frac{m^* k T}{\hbar^2} \right)^{2/3} \quad (2.20)$$

Note that T will be assumed to be low, which gives $\sigma = \sigma_1$ in the notation of Lagrange *et al.*. This gives Equation (2.21), which is the same relationship that is given in Lagrange *et al.*.

$$\sigma_1 = q \mu \frac{N_V}{g_a} \frac{N_A - N_D}{N_D} \exp\left(\frac{-E_A}{k T}\right) \quad (2.21)$$

Since the dependence on T is very small in N_V , Equation (2.21) can be approximated by Equation (2.22), where C is a constant.

$$\sigma_1 = C \exp\left(\frac{-E_A}{kT}\right) \quad (2.22)$$

By taking the natural log of Equation (2.22), the relationship takes the form of Equation (2.23).

$$\ln \sigma_1 = -\frac{E_A}{k} \frac{1}{T} + \ln(C) \quad (2.23)$$

Using the form of Equation (2.23), four-point probe conductivity data can be used to determine the conductivity activation energy E_A , from the slope of a plot of $\ln \sigma_1$ vs. $1/T$.

2.5 Contact Angle for Surface Termination

The surface termination of a diamond sample can affect the conduction properties, as previously discussed in Section 1.8. A sample with a hydrogen terminated surface will show the effects of surface conductivity, whereas oxygen terminating a diamond surface will eliminate the surface conductivity. The surface termination can be altered by exposure to a hydrogen or oxygen plasma, and the resulting surface termination can be investigated using the contact angle between the diamond surface and a small drop (on the order of 1 μ L) of deionized water. High contact angles indicate a hydrogen terminated surface, as shown in Figure 2.23 for a hydrogen plasma treated surface. Low contact angles indicate an oxygen terminated surface, as shown in Figure 2.24 for an oxygen plasma treated diamond surface.

The surface termination of a diamond sample can also be modified by acid treatment.

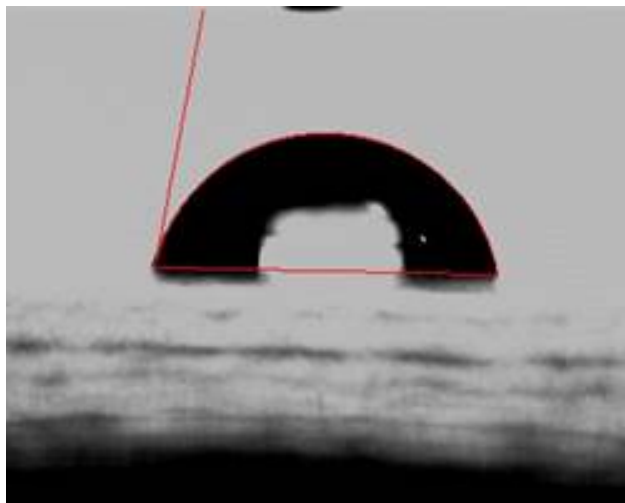


Figure 2.23 Exposure to a hydrogen plasma results in a high contact angle, like the 80.5° shown here for sample SND04

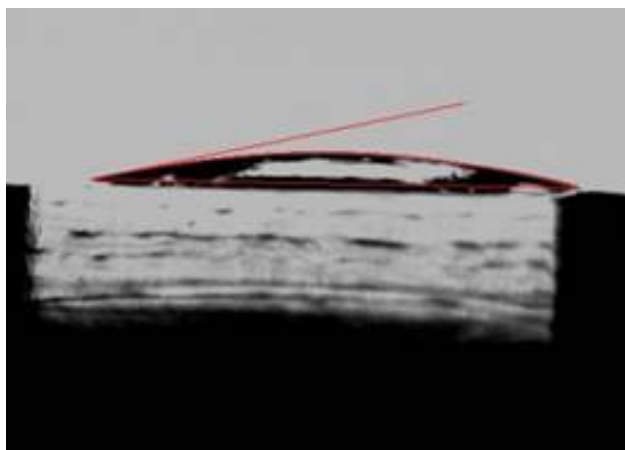


Figure 2.24 Exposure to an oxygen plasma results in a low contact angle, like the 12.7° shown here for sample SND05

The results of a study performed on SND09 on the effects of the post-deposition acid cleaning process are shown in Figure 2.25. The sample was originally hydrogen terminated after CVD growth, as indicated by a high contact angle. This is the expected result since diamond CVD growth is performed in a hydrogen plasma. The conductivity and contact angle were measured following each step in the acid treatment. After boiling in 1:1 nitric and sulfuric acid at 235°C for 20 minutes, the hydrogen terminated layer was partially removed, as indicated by a lower contact angle, and lower conductivity, indicating the removal of the surface conductivity,

as discussed previously in Section 1.8. The last two steps in the acid cleaning process, a boiling step in hydrochloric acid and a boiling step in ammonium hydroxide, had little effect on the surface termination. The surface termination was also not significantly affected by being left in the ambient air in the laboratory overnight.

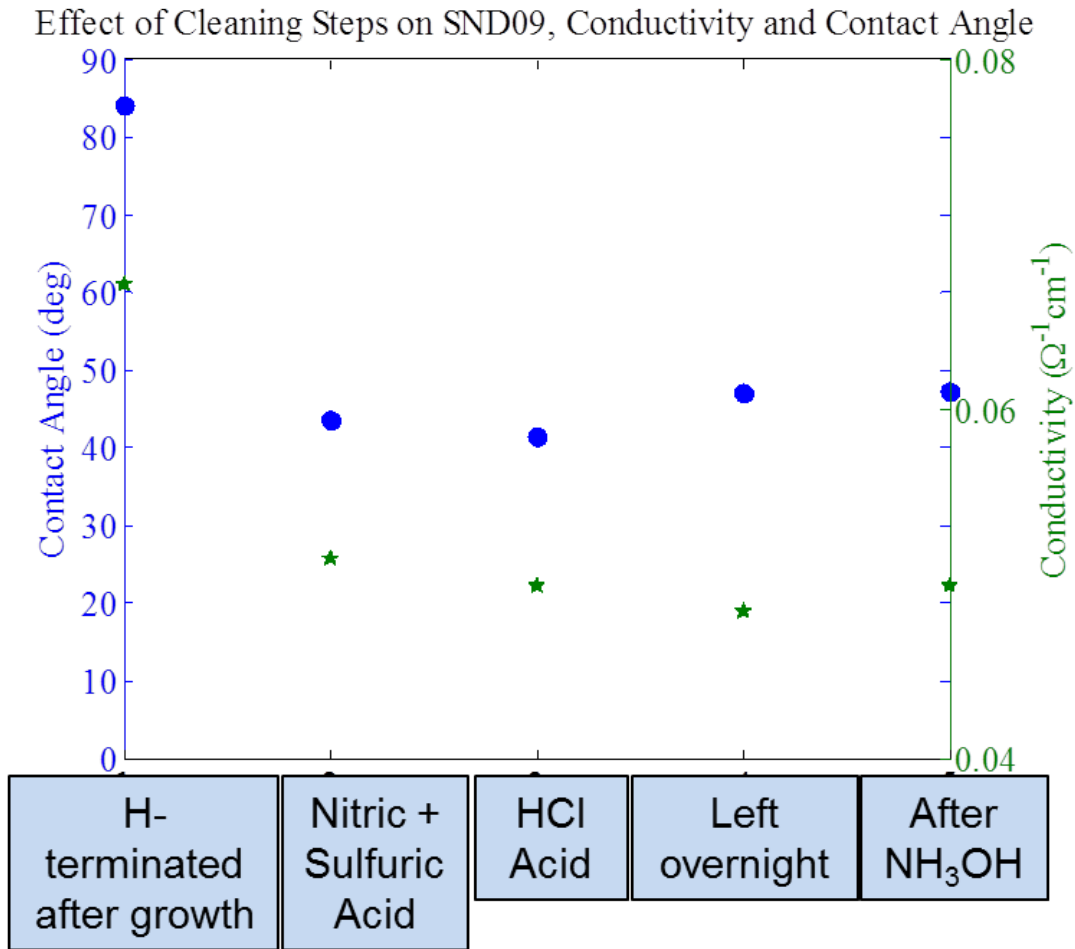


Figure 2.25 The effect of acid cleaning steps on the contact angle and conductivity of sample SND09

The contact angle of an oxygen terminated diamond surface will tend to increase over a period of days, as shown in Figure 2.26, where sample SND02 was oxygen terminated in an oxygen plasma, and then characterized over the course of a month, as its contact angle

continued to increase. The conductivity was also measured during this period, however no significant change over the study period was found, likely because the surface remained oxygen terminated enough to suppress the surface conductivity, as previously described in Section 1.8.

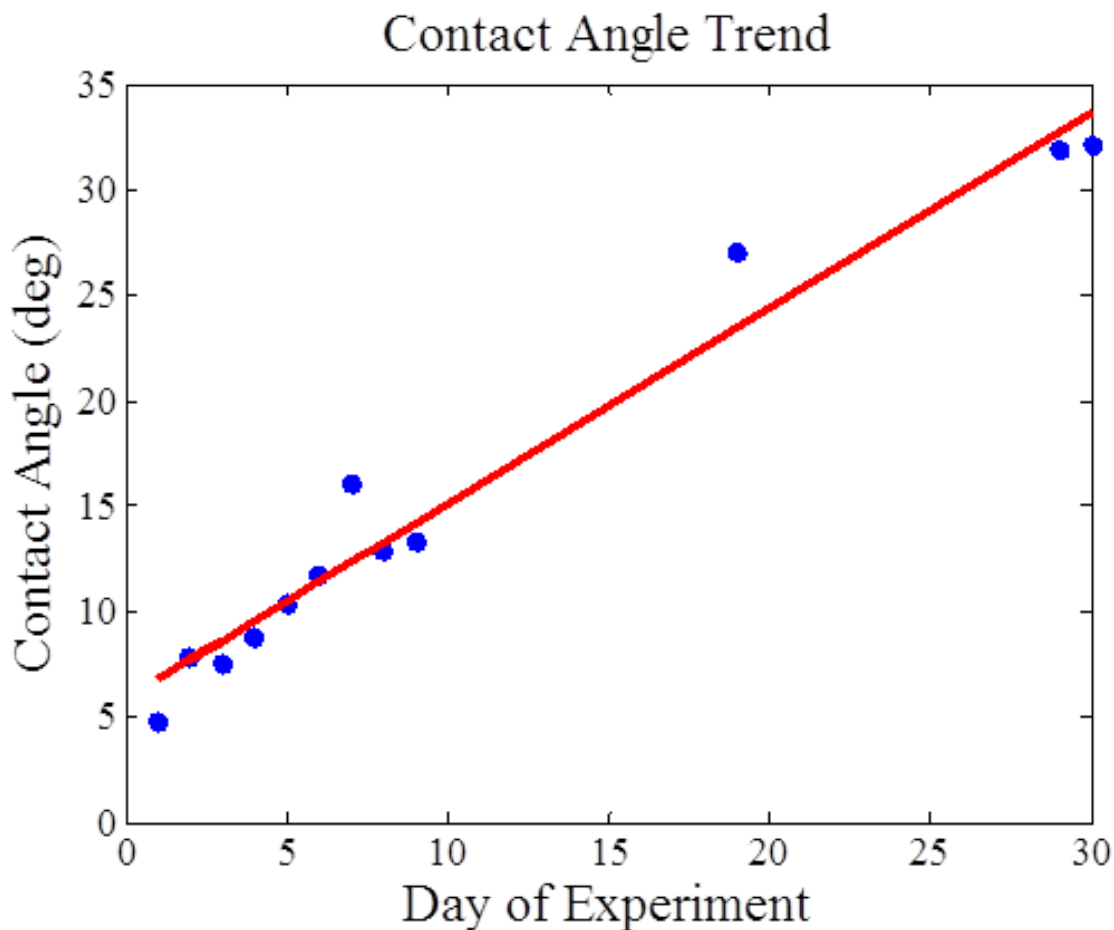


Figure 2.26 The contact angle of an oxygen terminated sample, such as for SND02 shown here, increases significantly over a period of days, indicating the O-termination is slowly lost.

2.6 X-Ray Diffraction (XRD) for Miscut Angle Determination

X-Ray Diffraction (XRD) measurements were performed as a part of this work to determine the miscut angle for HPHT substrates prior to deposition. These measurements were performed on a Bruker AXS instrument with the help of Dr. Richard Staples of the Department of Chemistry at MSU.

Samples were measured with $\phi = 15, 45, 120^\circ$ with 12° sweep. After obtaining a diamond lattice, the sample is photographed as it is rotated through 360° , and based on analysis of the images which are correlated with the obtained crystallographic orientation data, the miscut angle of a desired surface can be obtained.

Chapter 3

Low Level Boron Doping

The depletion region in diode structures, as discussed in Section 1.3, is formed in the active layer of the device, which for high power applications requires a high quality lightly boron doped diamond layer. A high quality lightly boron doped layer has a well-controlled level of the boron dopant, and for electronic applications, the optimized concentration is about $1 \times 10^{16} \text{ cm}^{-3}$ to $1 \times 10^{17} \text{ cm}^{-3}$ depending on the device structure.

This chapter reports on the results of experimental investigations on the growth and characterization of boron doped diamond with the aim of achieving high quality films with low boron concentrations for high power electronic applications. Section 3.1 describes the results of early investigations into growing lightly boron doped diamond in DS1. Section 3.2 describes the effect of adding carbon dioxide to the plasma feedgas in an effort to reduce the incorporated concentration of boron at low doping levels. Section 3.3 describes the electrical characterization for activation energy of a number of boron doped SCD samples grown in DS1. Section 3.4 describes investigations of the role of defects in dopant uniformity. Section 3.5 describes the successful deposition of lightly boron doped diamond in DS6, the new dedicated low level doping reactor that was built during this dissertation research.

3.1 Lightly Boron Doped Diamond Growth in DS1

Prior to the beginning of this dissertation work, Rahul Ramamurti, a postdoctoral researcher in the MSU-Fraunhofer lab, had researched boron doped diamond growth on DS1, a MPACVD reactor that was described in Section 2.1.1. These investigations included boron doped polycrystalline diamond [50], and heavily boron doped single crystal diamond [51]. An investigation of thick films of boron doped single crystal diamond at moderate doping levels also explored the intentional addition of nitrogen to improve the growth rate [52].

Early in this dissertation research, a series of growth experiments was performed in DS1 to determine if high quality lightly boron doped diamond could be grown in this reactor. The deposition conditions for this investigation are given in Table 3.1.

Sample	Pressure [Torr]	CH ₄ [%]	Total flow rate [sccm]	B/C gas phase [ppm]	Intentional H ₂ etching [min]	Sample temperature during growth [°C]
151	160	4.7	638	13.33	53	1100
152	130	4.7	634	6.67	30	800
153	140	3.9	416	12.5	60	990
154	140	3.9	416	50	60	950

Table 3.1 Deposition characteristics for samples 151-154, grown in DS1.

The samples of this investigation were characterized for the grown thickness of the layers and the boron concentration in the film, using the calibration of Equation (2.3) as described in Section 2.2.1. The results of this characterization are given in Table 3.2.

The results of Table 3.2 show that the doping concentrations obtained in these early growth experiments were on the range of $6 \times 10^{17} \text{ cm}^{-3}$ to $2 \times 10^{18} \text{ cm}^{-3}$. This is higher than is desirable for the active layer in a high power diode device, which is the aim of the lightly boron doped deposition work performed in this dissertation.

Sample	Grown film thickness [μm]	Time of deposition [h]	Growth rate [$\mu\text{m h}^{-1}$]	$N_A - N_D$ estimate (FTIR) [cm^{-3}]
151	10	2.0	7.7	1.2×10^{18}
152	28	2.0	4.3	7.7×10^{17}
153	9	4.0	5.5	6.0×10^{17}
154	16	4.0	3.6	2.0×10^{18}

Table 3.2 Characterization results for the samples of Table 3.1

3.2 Carbon Dioxide in the Plasma Feedgas

The samples described in Section 3.1 showed boron concentrations higher than the optimized boron concentration of approximately 10^{16} to 10^{17}cm^{-3} for lightly boron doped diamond for electronic applications. Controlling the doping to a low and repeatable level for lightly boron doped diamond is a key goal in this dissertation work, as it is crucial for the realization of high power diamond electronics.

Adding 0.25% oxygen to the feedgas mixture during CVD growth has been shown to lower the boron concentration in grown diamond films [94, 95]. To investigate if the oxygen containing species that result from adding carbon dioxide to the growth plasma have a similar effect of controlling the boron concentration, a series of experiments were performed. The details of these experiments are given in Table 3.3.

Initial experiments in this investigation of the effects carbon dioxide tested growth chemistries with $\leq 1\%$ CO_2 in the plasma feedgas. A reactor pressure of 160 Torr was selected as this was a typical pressure for depositions performed on DS1 at that time. The defect morphologies of these samples are shown in Figure 3.1. The samples of Figure 3.1 all show a relatively high concentration of mixed pyramidal and flat topped hillocks. SND03 was grown with 1% CO_2 , whereas the other samples of Figure 3.1 were grown with similar

Sample	P [Torr]	CH ₄ [%]	B ₂ H ₆ [ppm]	CO ₂ [%]	Temp [°C]	Growth rate [μm h ⁻¹]	Grown thickness [μm]	N _A - N _D [cm ⁻³]
SND02	160	4.0	0.25	0.25	900	7.05	28	3.0 × 10 ¹⁷
SND03	160	4.0	0.25	1.0	900	2.32	9	3.9 × 10 ¹⁷
SND04	160	4.0	0*	0.25	900	4.10	16	6.0 × 10 ¹⁷
SND05	160	4.0	0*	0.25	900	3.52	16	3.0 × 10 ¹⁷
SND07	75	3.7	0*	3.5	900	0.24	2	< 1.2 × 10 ¹⁷ ‡
SND08	75	3.7	0.06	3.5	850	0.18	3	< 7.3 × 10 ¹⁶ ‡
SND10	160	3.7	0.06	3.5	900	- †	- †	< 6.5 × 10 ¹⁶ ‡
SND17	160	3.7	0*	3.5	1000	- †	- †	< 2.0 × 10 ¹⁷ ‡

Table 3.3 Effect of Carbon Dioxide in the Plasma Feedgas

* - 0 diborane flow in the feedgas - doping in sample is due to residual boron in reactor from previous runs

† - Grown thickness below measureable threshold

‡ - 2800 cm⁻¹ peak below resolution limits. Upper bound of uncompensated acceptor concentration estimated based on maximum concentration possible for grown film thickness

growth conditions, but with only 0.25% CO₂. From Table 3.3, it is clear that there was no substantial decrease in boron concentration from SND02 to SND03, despite increasing the CO₂ concentration by a factor of four, in fact, the FTIR estimate of boron concentration actually increased. Even when the diborane was removed from the feedgas, as was done in SND04 and SND05, with 0.25%CO₂ still in the feedgas mixture, there was still no substantial decrease in the estimated boron concentration. The most substantial change achieved by increasing the CO₂ concentration from 0.25% to 1% was a drop in the growth rate. There seems as well to be a decrease in the size of defects in SND03 compared to the other samples, however this could also be due to the decreased thickness compared to the other films.

To determine whether a more substantial increase in the carbon dioxide concentration would affect the boron concentration, two experiments with 3.5% CO₂ at 75 Torr were performed, and the grown sample morphologies are shown in Figure 3.2. Both samples show high concentrations of very small hillock-type defects. The presence of this morphology in

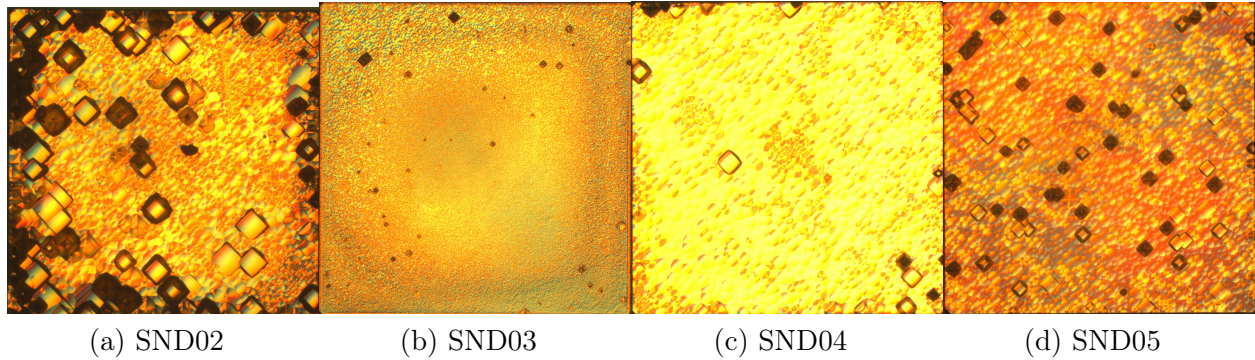


Figure 3.1 Reflection mode optical micrographs of SND03, SND04, and SND05, samples grown at 160 Torr and $\leq 1\%$ CO_2

both samples indicates that these defects may be related to the high CO_2 content at this lower deposition pressure. In both samples the 2800 cm^{-1} absorption feature was below detection limits, showing that a decrease in the boron concentration was achieved. However, the growth rates dropped extremely low, and only a very thin film was grown during the deposition time.

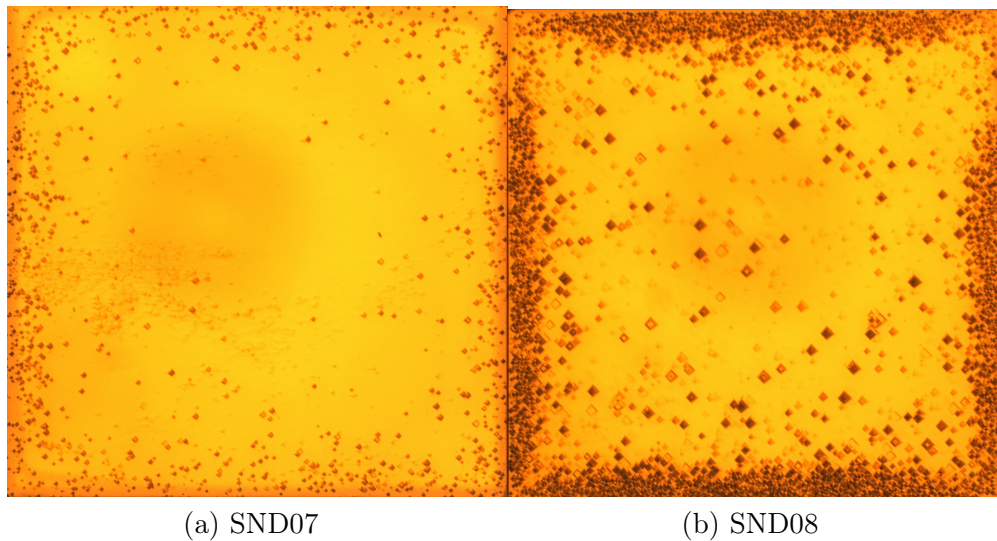


Figure 3.2 Reflection mode optical micrographs of SND07, and SND08, samples grown at 75 Torr and 3.5% CO_2

Increasing the reactor pressure can increase the growth rate for CVD diamond growth. To

determine if the low pressure was the cause of the very low growth rates in the SND07 and SND08, two samples were grown with 3.5% CO₂ at 160 Torr, and the resulting morphologies are shown in Figure 3.3. The morphologies suggest that etching was the dominant process during the deposition, and the grown sample thicknesses were below the measurable threshold.

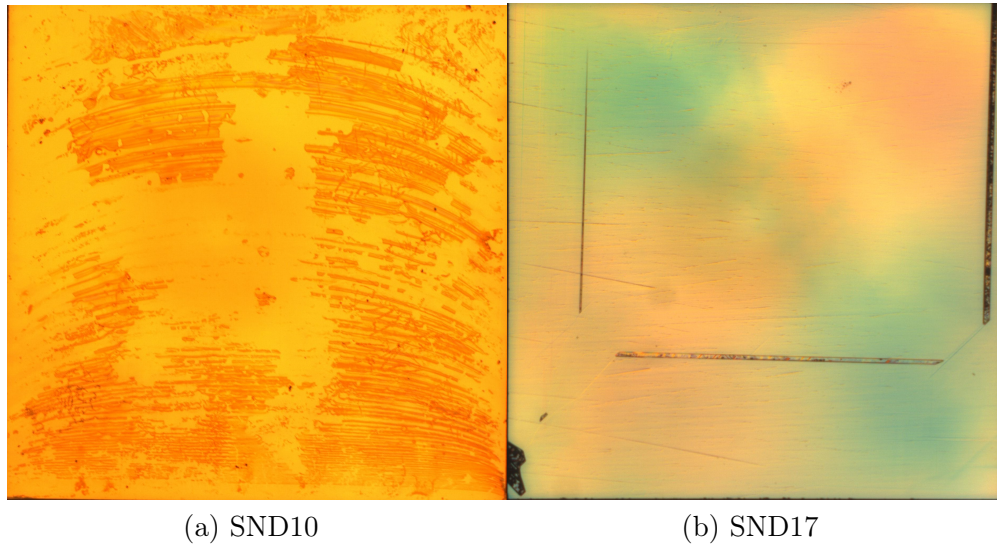


Figure 3.3 Reflection mode optical micrographs of SND10, and SND17, samples grown at 160 Torr and 3.5% CO₂

The results of the investigation of the effects of carbon dioxide in the plasma feedgas during boron doped diamond growth suggest that high concentrations of carbon dioxide (3.5%) may decrease the boron concentration in grown films. However, the results clearly indicate that the carbon dioxide decreases the growth rate, to the point where the dominant process may be etching, especially at high CO₂ concentration and high pressure (160 Torr).

3.3 Electrical Characterization

The electrical characteristics of several SCD samples grown in DS1 were studied to determine the activation energy of the boron acceptor. The use of temperature dependent four point

probe conductivity measurements for activation energy determination was described in Section 2.4. The deposition conditions for the samples studied are given in Table 3.4. Some of the samples described here have also previously been described in Section 3.2, but are repeated here for convenience.

Sample	Pressure [Torr]	CH ₄ [%]	B ₂ H ₆ gas phase [ppm]	B/C gas phase [ppm]	CO ₂ gas phase [%]	Sample temperature during growth [°C]
150	160	4.7	1	27	0	1100
SND01	160	3.8	0.25	12.5	0	900
SND02	160	3.8	0.25	12.5	0.25	900
SND03	160	3.8	0.25	12.5	1	900
SND04	160	3.8	0*	0*	0.25	900
SND05	160	3.8	0*	0*	0.25	900
174	160	3.8	0*	0*	0.25	900
RR02	140	4	10	500	0	1070

Table 3.4 Deposition characteristics for the electrically characterized samples. All samples grown in DS1.

* 0 - diborane flow in the feedgas, doping in sample is due to residual boron in reactor from previous runs

Temperature dependent four-point probe conductivity data was taken for the samples listed in Table 3.4, as described in Section 2.4. The conductivity data was used to determine the acceptor activation energy, E_A , by fitting to the relationship of Equation (3.1).

$$p^2 + pN_D = \frac{N_V}{g_a} (N_A - N_D - p) \exp\left(\frac{-E_A}{k T}\right) \quad (3.1)$$

The temperature range used for fitting E_A , was 21 to 120 °C. E_A values and $\mu(T)$ were fitted to each curve. Teraji [3] reported that the mobility decreases with increasing temperature as $\mu \propto T^{-1.3} - T^{-1.6}$ for $T < 270$ K. This dependence is attributable to acoustic phonon scattering [3]. Above 270 K however, (in the range measured in this investigation), Teraji reported that $\mu(T)$ has a dependence of $T^{-4} - T^{-4.5}$. The mechanism for this scattering

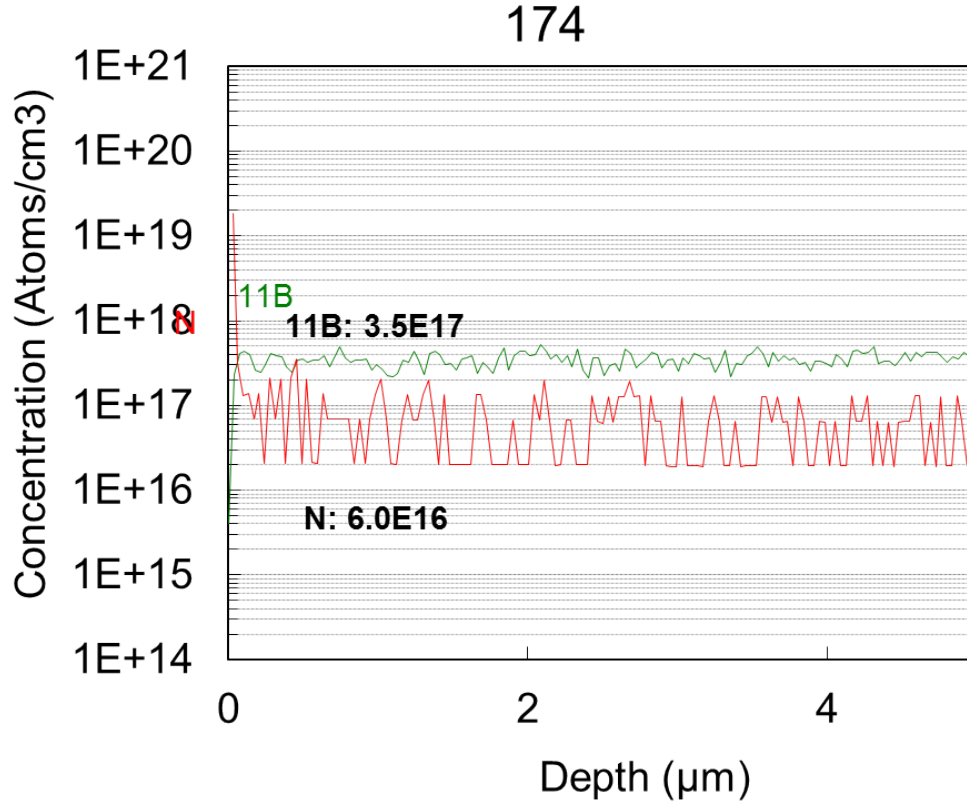


Figure 3.4 SIMS data from Sample 174

remains unclear, however a strong temperature dependence of the mobility for temperatures above 300 K has been obtained in many investigations [96, 97, 98]. In this work, $\mu(T)$ is therefore assumed to have a $T^{-4.0}$ temperature dependence [3].

Room temperature μ (hereafter μ_{300}) values of 400 to 800 $\text{cm}^2 \text{V}^{-1} \text{s}^{-1}$ were fitted to the curves for the more lightly boron doped samples, and $\mu_{300} = 60 \text{ cm}^2 \text{V}^{-1} \text{s}^{-1}$ was fitted to the highly doped sample RR02, which had been grown in an earlier investigation in this lab [51], prior to the start of this dissertation research. N_A values were approximated from FTIR measurements, as described in Section 2.2. N_D was approximated at $1 \times 10^{16} \text{ cm}^{-3}$, based on the level of N found by SIMS. As described in Section 2.3, SIMS measures the total N content, and since N_D is exclusively the electrically active N, N_D is estimated lower than the

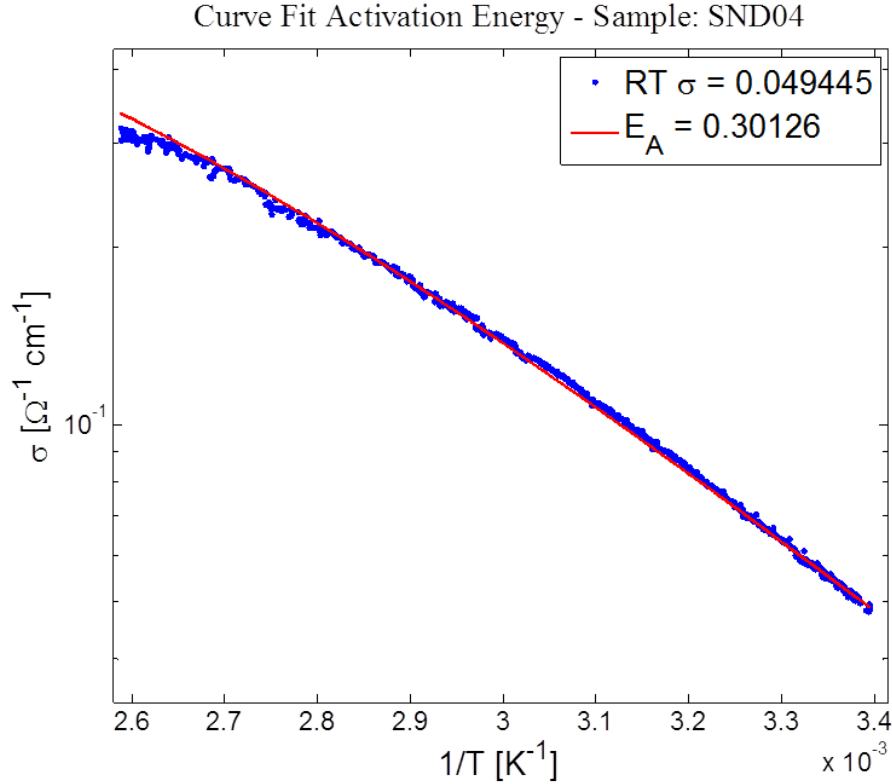


Figure 3.5 Temperature dependent conductivity data for SND04 (blue), shown with the curve from the fit used to determine E_A (red)

SIMS value. Figure 3.4 shows the SIMS results for Sample 174. An example of the fitting is shown in Figure 3.5, where the temperature dependent conductivity data for SND04 is fitted with $E_A = 0.30$ eV. The room temperature conductivity, σ_{RT} is also given, where room temperature is given as the lowest temperature measured, at $\sim 22^\circ\text{C}$. Samples were oxygen plasma treated to remove surface conductivity, except where it is noted that a sample was acid cleaned but not oxygen plasma treated prior to measurement.

The results of the activation energy fitting and FTIR characterization of the samples from Table 3.4 are given in Table 3.5. The activation energies were found to be on the range of 0.32 to 0.35 eV, which is what might be expected for samples with this range of boron concentration. Figure 3.6 shows the activation energies along with other values reported in the literature [99, 100] and the model of Bardeen and Pearson [101], to guide the eye, plotted

Sample	Grown film thickness [μm]	σ_{RT} Room temp. conductivity [$\Omega^{-1} \text{cm}^{-1}$]	I_{2800} [eV cm^{-1}]	$N_A - N_D$ estimate (FTIR) [cm^{-3}]	E_A from $\sigma(T)$ [eV]
150	13	0.0539	0.7743	6.2×10^{17}	0.3526
SND01	10	0.0597	0.6385	5.1×10^{17}	0.3463
SND02	28	0.0369	0.3732	3.0×10^{17}	0.3395
SND03	9	0.0288*	0.4830	3.9×10^{17}	0.3438
SND04	16	0.0209	0.7540	6.0×10^{17}	0.3390
SND05	16	0.0344	0.3819	3.1×10^{17}	0.3261
174	10	0.0810*	0.9566	7.7×10^{17}	0.3478
RR02	142	0.0355	-	2.0×10^{18}	0.3222

Table 3.5 Electrical characterization results for the samples of Table 3.4

* - Acid cleaned, but not oxygen plasma treated prior to measurement

using the method of [102].

Even for the characterized samples grown without diborane added to the plasma feedgas, doping concentrations above $3 \times 10^{17} \text{cm}^{-3}$ were still obtained. This level of doping is also supported by the range of activation energies found for these samples. This high level of unintentional boron doping shows that the reactor memory effect, as described in Section 1.7.2, is a serious issue in DS1.

3.4 Defects and the Uniformity of Doping

Defects, like the ones on sample SND02, shown in Figure 3.7, have previously been shown to have a high incorporated boron concentration. As pyramidal hillock defects develop during growth, they expose (111) surfaces to the CVD reaction process. (111) surfaces have been shown to have an order of magnitude or more incorporated boron concentration after CVD growth than (100) surfaces. [103, 104]

To investigate the influence of the pyramidal defects on the measured boron concentra-

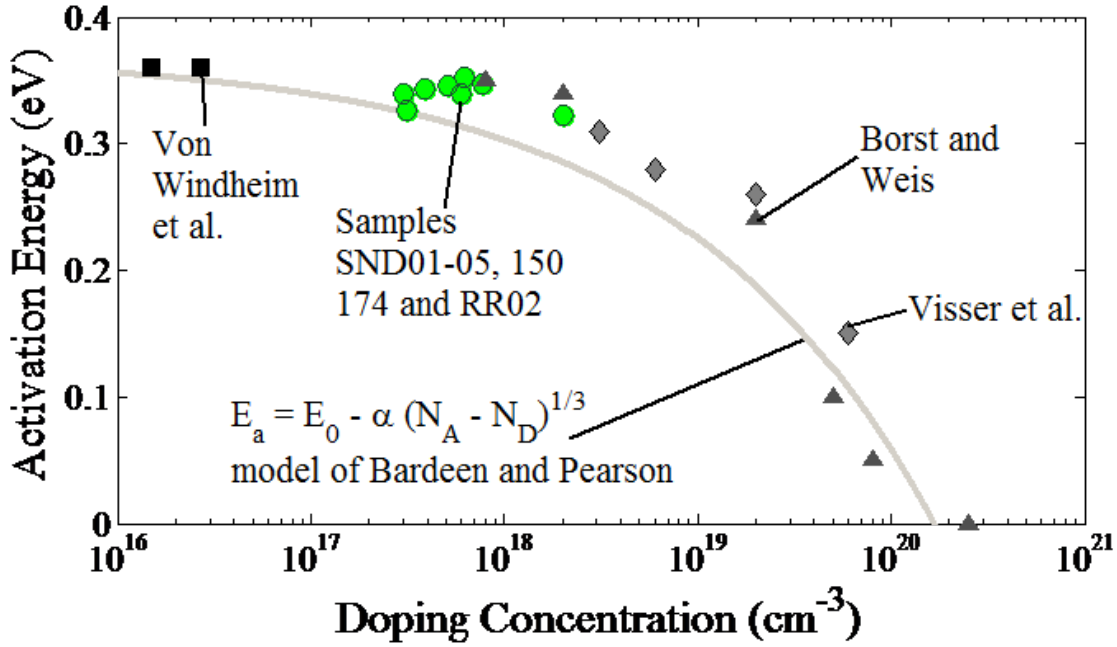


Figure 3.6 Activation energies from this work, shown with other values reported in the literature [99, 100] and the model of Bardeen and Pearson [101], following the method of [102], to guide the eye.

tion using the FTIR method, SND02 was analyzed, since on this sample the defects are asymmetrically distributed, with a higher concentration in some orientations than in others. To see the effect of the orientation of the sample, half of the FTIR aperture was blocked along the diagonal of the sample, and the sample was rotated in the half-open/half-closed aperture through four orientations that exposed different sections of the sample surface for IR transmission spectrum collection. Depending on the orientation, the absorption feature at 2800 cm^{-1} changed in size, as seen in Figure 3.8. When only Side 1, as shown in Figure 3.7 is exposed, the FTIR determined uncompensated acceptor concentration was measured as $2.9 \times 10^{17}\text{ cm}^{-3}$. When only Side 2, which has a higher defect density as determined by analysis of the darker regions of the optical micrograph, is exposed, the estimated concentration increases to $3.2 \times 10^{17}\text{ cm}^{-3}$

The results of this investigation of the role of defects in dopant uniformity indicate that

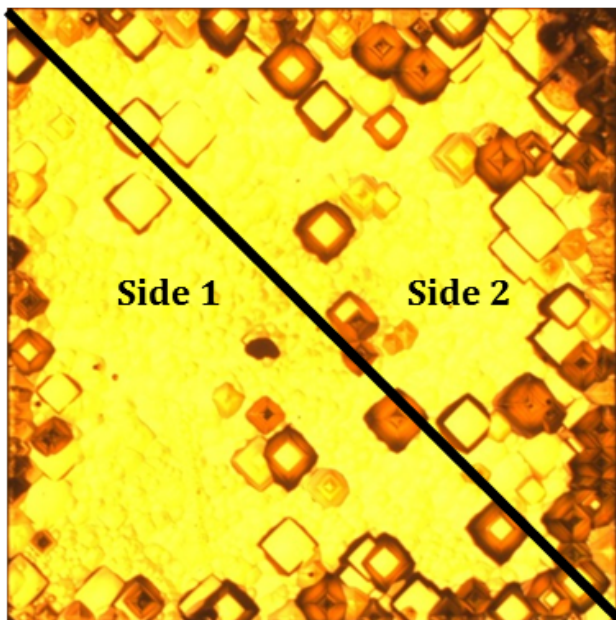


Figure 3.7 Optical micrograph of SND02, which has asymmetrically distributed defects. The FTIR spectrum when only Side 1 is exposed gives a lower estimate of the uncompensated acceptor concentration than the more defect-dense Side 2 (see text). Sample has dimensions: 3.5 mm 3.5 mm

the defects are a key parameter in the dopant uniformity, and must be minimized to achieve the goal of uniform doping.

3.5 New Low Boron Doping System (DS6) Results

The reactor memory effect, as described in Section 1.7.2, proved to be a significant issue in the samples grown in DS1 in the lightly boron doped investigations described in Section 3.2 and Section 3.3. Boron concentrations above $3 \times 10^{17} \text{ cm}^{-3}$ were obtained for samples grown in DS1 even without any diborane in the feedgas. The reactor memory effect is a significant obstacle in achieving electronic grade lightly boron doped diamond, since it causes higher levels of boron than are desirable for many applications, and inconsistent results for lightly doped films depending on the recent reactor usage. To overcome this issue, DS6 was built

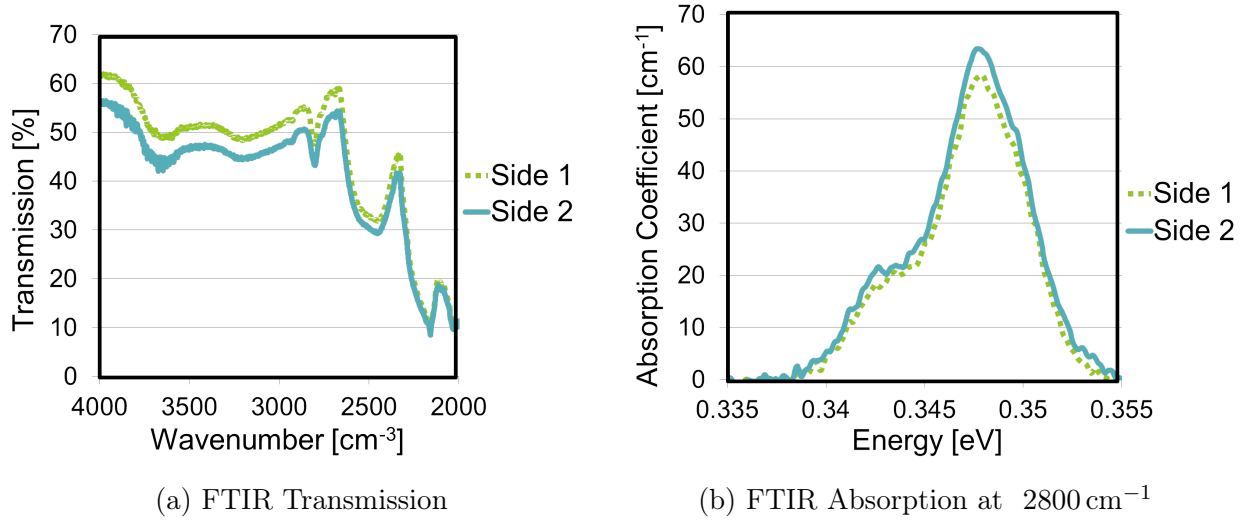


Figure 3.8 Transmission (a) and absorption coefficient (b) spectra for two half aperture orientations of SND02, showing the difference in the measured boron concentration based on the distribution of defects

for the purpose of the dedicated deposition of lightly boron doped SCD, as described in Section 2.1.2. This section will describe the realization of lightly boron doped diamond in DS6, and present the optimization process for achieving low defect, lightly boron doped diamond.

Sample	Growth temp. (°C)	MW power (kW)	Pressure (Torr)	B/C gas phase (ppm)	Growth time (h)	Grown thickness at center (μm)	$N_A - N_D$ FTIR approx. (cm^{-3})
LB01	870	2.25	190	0	5.5	33.7	—
LB02	920	2.55	170	4.8	6.5	39.5	2.4×10^{16}
LB03	790	2.15	170	9.6	5.25	9.0	3.3×10^{17}
LB04	804	2.15	170	9.6	3.0	7.5	1.3×10^{17}
LB05	809	2.15	170	19.2	5.5	11.2	3.2×10^{17}
156_1	800	2.0	170	4.8	3.5	5.2	1.6×10^{17}

Table 3.6 Growth conditions for the lightly boron doped process optimization experiments performed on the new low boron doping diamond deposition system

To determine optimal conditions for high quality lightly boron doped films, a series of

deposition experiments were performed. All of the samples were run with 3.75% methane in the hydrogen plasma feedgas, and the other deposition parameters are given in Table 3.6. Table 3.6 also lists the approximate boron concentration, obtained by FTIR, using the calibration for the 2800 cm^{-1} absorption feature given by Collins and Williams [81], using the method described in Section 2.2.

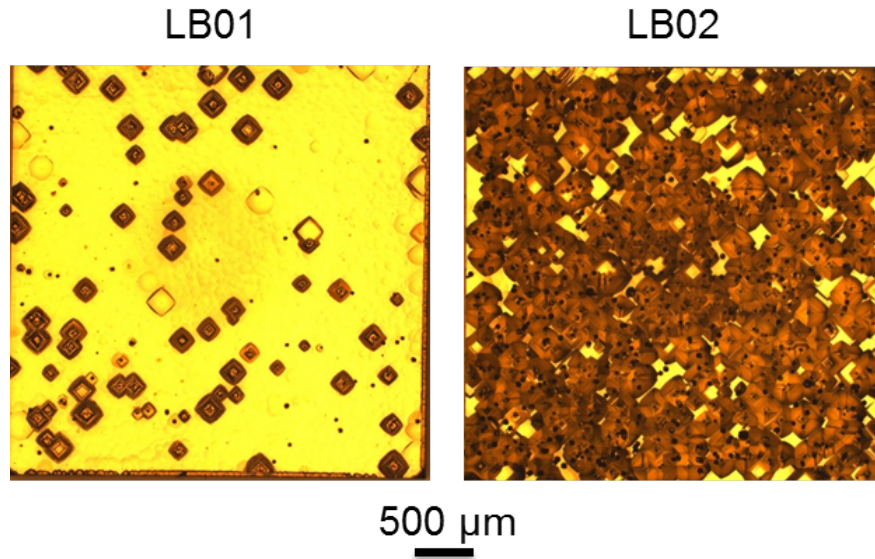


Figure 3.9 Optical micrographs taken at $2.5\times$ magnification in reflection mode, showing the surface morphology of Samples LB01 and LB02. These samples were grown with substrate temperatures of 870 to $920\text{ }^{\circ}\text{C}$ in DS6, and showed many pyramidal hillock defects

The first deposition experiments in DS6 are shown in Figure 3.9. Initially, a sample temperature of approximately $900\text{ }^{\circ}\text{C}$ was selected, as this temperature had led to high quality diamond deposition in DS1, as will be discussed further in Chapter 4. As shown in Figure 3.9 however, the samples grown at approximately this temperature in DS6 showed many pyramidal hillocks, which tended to form in DS1 at much higher temperatures.

To reduce the formation of the pyramidal hillocks, a lower substrate temperature of approximately $800\text{ }^{\circ}\text{C}$ was tried, and the resulting defect morphologies of samples grown in the temperature range of 790 to $809\text{ }^{\circ}\text{C}$ are shown in Figure 3.10.

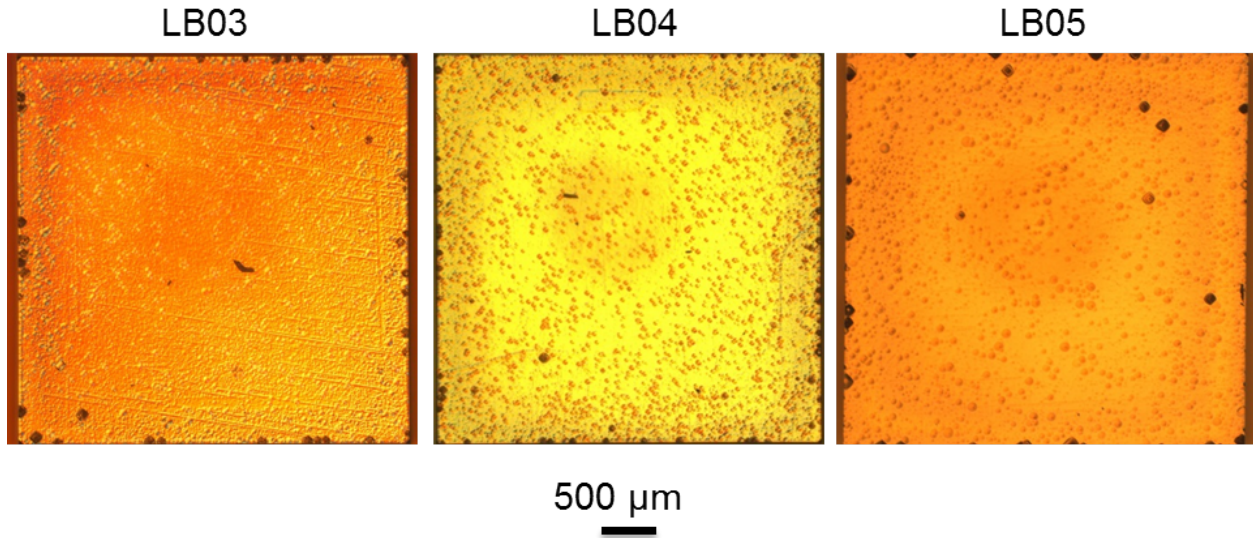


Figure 3.10 Optical micrographs taken at $2.5\times$ magnification in reflection mode, showing the surface morphology of samples LB03, LB04, and LB05, grown in DS6. These samples were grown with substrate temperatures of 790 to 809 °C, and have almost no pyramidal hillock defects

For the fabrication of a corner architecture diode, as will be described in Chapter 5, it was necessary to develop an optimized process for the deposition of high quality lightly boron doped diamond on a thin sample substrate. Sample 156_1, with surface morphology shown in Figure 3.11, was grown on an $\sim 500\ \mu\text{m}$ thick substrate that had been grown at MSU by CVD, and subsequently laser cut and polished. The laser cutting and polishing processes used will be described in Chapter 5. The resulting sample morphology was smooth and had very few visible defects. The optimized process used for the deposition of sample 156_1 will also be used for the p^- -layer in the corner architecture diode that will be described in Chapter 5.

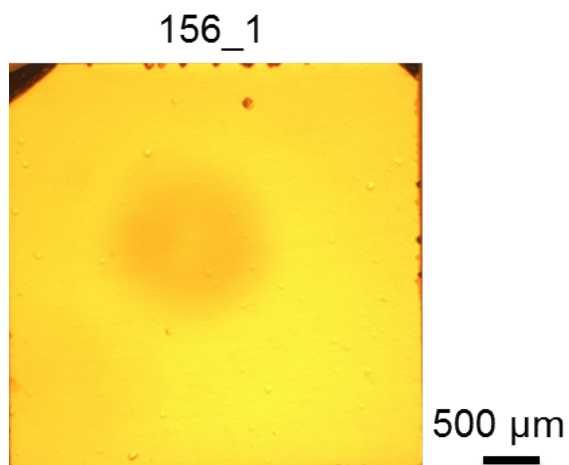


Figure 3.11 Optical micrograph taken at $2.5\times$ magnification in reflection mode, showing the surface morphology of sample 156_1, grown in DS6. The optimized process resulted in a very smooth, low defect surface.

Chapter 4

Heavy Boron Doping

The realization of high power diode structures, as discussed in Section 1.3, requires a heavily boron doped layer to reduce the on-state resistance and form a good ohmic contact. For the formation of a vertical architecture, as discussed in Section 1.3.2, this heavily doped layer would need to be grown thick enough to be laser cut from the growth substrate, and still be mechanically handleable for polishing, which means a grown layer of at least approximately 300 μm thickness. Ideally this layer would also have as low a resistance as possible, which in principle means that the doping level should be as high as possible. As discussed previously in Section 1.7.5, some researchers have found that as the plasma gas phase boron-to-carbon ratio increases that there is a decreasing doping efficiency into the grown diamond film that reaches a saturation value of $\approx 4 \times 10^{19} \text{ cm}^{-3}$ [55]. Determining the factors responsible for this saturation value and then overcoming this challenge is important for the ultimate realization of high power diode structures. In order to achieve this goal, a number of experimental investigations have been carried out on the growth and characterization of heavily boron doped SCD. These results are presented in this chapter. A systematic study of the effect of the substrate temperature during growth is described in Section 4.1, and results on the effect of flow rate are given in Section 4.2.

4.1 Effect of Substrate Temperature During Growth

To better understand the role of substrate temperature during growth, a series of experiments varying the growth temperature and boron-to-carbon feedgas ratio were performed. In the deposition experiments of this investigation, a reactor pressure of 240 Torr, methane concentration of 3.75% in the plasma feedgas, and total flow rate of 400 sccm were held constant. Using this growth regime, three growth temperatures were initially tried, and the resulting grown defect morphologies are shown in Figure 4.1.

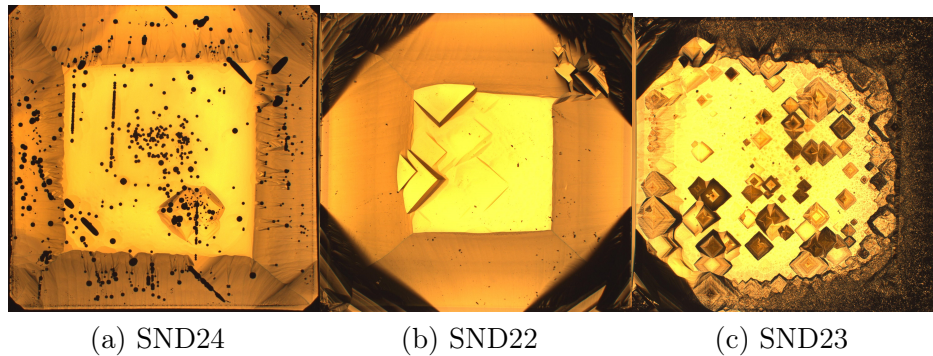


Figure 4.1 Optical micrographs, taken in reflection mode, showing the defect morphologies of samples grown with $[B]/[C] = 666$ ppm in the plasma gas phase at three different substrate growth temperatures: (a) 850 °C, (b) 950 °C, (c) 1050 °C

The sample grown at 1050 °C showed a large number of pyramidal hillock type defects and polycrystalline regions. The formation of polycrystalline regions at higher deposition temperatures may be expected, and has been noted by other groups as well [105]. Soot deposition during boron doped diamond growth is known to increase with increasing microwave power levels [55], and so there were additional concerns that increasing the microwave power to achieve higher temperatures would produce more soot deposition at higher doping levels. As a result, 1050 °C was eliminated as a temperature from the experimental design in this investigation. Samples were therefore grown at either 850 °C or 950 °C. Only the temperature

during growth (controlled by the microwave power) and the diborane concentration were varied in this investigation, and the other deposition variables were held constant in order to minimize the influence of other factors on the growth. The deposition conditions are given in Table 4.1.

Sample	Growth temp. [°C]	MW power during growth [kW]	B/C gas phase [ppm]	Center growth rate [$\mu\text{m h}^{-1}$]	Corner growth rate [$\mu\text{m h}^{-1}$]	Grown thickness at center [μm]	[B] estimate from FTIR [cm^{-3}]
SND24	850	1.6 – 1.8	666	2.08	5.48	16.60	4.2×10^{19}
SND22	950	1.7 – 1.9	666	2.02	10.64	16.18	4.8×10^{19}
SND25	850	1.6 – 1.9	933	4.96	10.13	39.68	5.9×10^{19}
SND26	950	1.8 – 2.2	933	1.17	8.38	9.33	7.4×10^{19}
SND27	850	1.6 – 1.9	1333	2.21	5.05	17.68	9.8×10^{19}
SND28	950	1.7 – 1.9	1333	1.13	4.43	9.02	9.7×10^{19}
SND30	850	1.5 – 1.8	2000	3.05	6.19	24.40	8.2×10^{19}
SND29	950	1.5 – 1.7	2000	2.06	9.06	16.48	3.0×10^{20}
SND33	850	1.6 – 2.1	3333	2.78	8.54	16.65	2.0×10^{20}
SND34	950	2.0 – 2.1	3333	1.51	8.64	11.35	4.1×10^{20}

Table 4.1 Effect of Substrate Temperature During Growth

Deposition times are counted from the point when the reactor reaches 240 Torr and the methane flow is started. Depositions were run for 8 hours, except for the two highest doping concentration runs, which had to be stopped early due to soot deposition on the reactor quartz dome after 6 hours (SND33) and 7.5 hours (SND34).

Microwave power was varied between 1.5 kW and 2.2 kW to maintain a constant substrate temperature, as given in Table 4.1. The microwave power was adjusted as needed during the runs, and most samples required greater applied microwave power at the beginning of deposition runs to maintain the set point temperature than near the end of the deposition. The microwave power is therefore given as a range in Table 4.1. The as-received type Ib

HPHT substrates, which have a nominal thickness of 1.4 mm, can vary in thickness by 100 μm or more, and since the same sample holder set was used for all the depositions, the thinner substrates were used for the 850 $^{\circ}\text{C}$ experiments, and thicker substrates were used for the 950 $^{\circ}\text{C}$ experiments. This was done to minimize the difference in the applied microwave power needed to maintain the required substrate temperatures, and therefore as similar a plasma chemistry as possible was maintained for the depositions from run to run. It should be noted however, that varying the applied microwave power by as much as 32% may have an effect on the microwave power density, and therefore the plasma chemistry. The samples grown at 950 $^{\circ}\text{C}$ did require slightly higher applied microwave power, averaging 1.74 – 1.96 kW, while the samples grown at 850 $^{\circ}\text{C}$ averaged 1.58 – 1.9 kW. These two ranges have significant overlap, and the microwave power used for individual samples is quite similar. As a result, the differences noted in samples from the two temperature set-point groups are assumed to be due to the growth temperature, rather than primarily due to a change in plasma chemistry.

Growth rates of 1 to 5 $\mu\text{m h}^{-1}$ at the center and 4 to 11 $\mu\text{m h}^{-1}$ at the corners were obtained, as given in Table 4.1. The boron concentration was determined from FTIR using the Davies calibration for the absorption feature at 1290 cm^{-1} , as previously described in section Section 2.2.2.4. The thickness used for the FTIR calculation is the center thickness reported in Table 4.1, since the center region is exposed for the FTIR measurement.

The main conclusions of this investigation, that heavily boron-doped diamond samples grown with a substrate temperature of 950 $^{\circ}\text{C}$ show fewer defects and higher doping efficiency than those grown at 850 $^{\circ}\text{C}$, will be detailed in sections Sections 4.1.1 to 4.1.3. These are significant positive results, as they identify a reactor regime in which reasonably high quality heavily boron doped diamond can be grown.

Section 4.1.4 will show that the gas phase boron to sample carbon flux ratio, as obtained

by dividing the $[B]/[C]$ gas phase ratio by the growth rate, is a more predictive measure of boron content in the grown diamond than the $[B]/[C]$ ratio alone. This suggests that the boron incorporation rate does not increase at the same rate as the growth rate, and therefore faster growth rates will result in lower boron concentration levels. This is an interesting result, which will help to guide future boron doped diamond growth experiments.

Section 4.1.5 will compare the results of FTIR and SIMS measurements for the determination of boron content for heavily boron doped samples.

4.1.1 Temperature Dependent Defect Morphology

Optical micrographs of the grown sample surfaces are given in Figures 4.1 and 4.2. The samples grown at 950 °C show a different defect morphology, with virtually none of the unepitaxial crystallite nucleation defects that dominate the surface of the samples grown at 850 °C. The reflection mode optical microscopy images shown in Figures 4.1 and 4.2, which are used for comparison of defect morphologies, tend to exaggerate the yellow color of the grown films. For comparison, an as-received HPHT seed and two of the samples of this work are shown in the photograph in Figure 4.3, where the heavily doped sample appears much darker than in the optical micrographs.

One possible mechanism by which the samples grown at 950 °C grow smoother, with less unepitaxial crystallite defects than those grown at 850 °C, could be related to the increase in the migration of the carbon species across the epitaxial surface during growth. At higher growth temperatures the carbon species may migrate more during growth. For lower simulated deposition temperatures, May *et al.* have shown that increasing migration events gives smoother films than direct absorption dominated growth processes with fewer migration events [106].

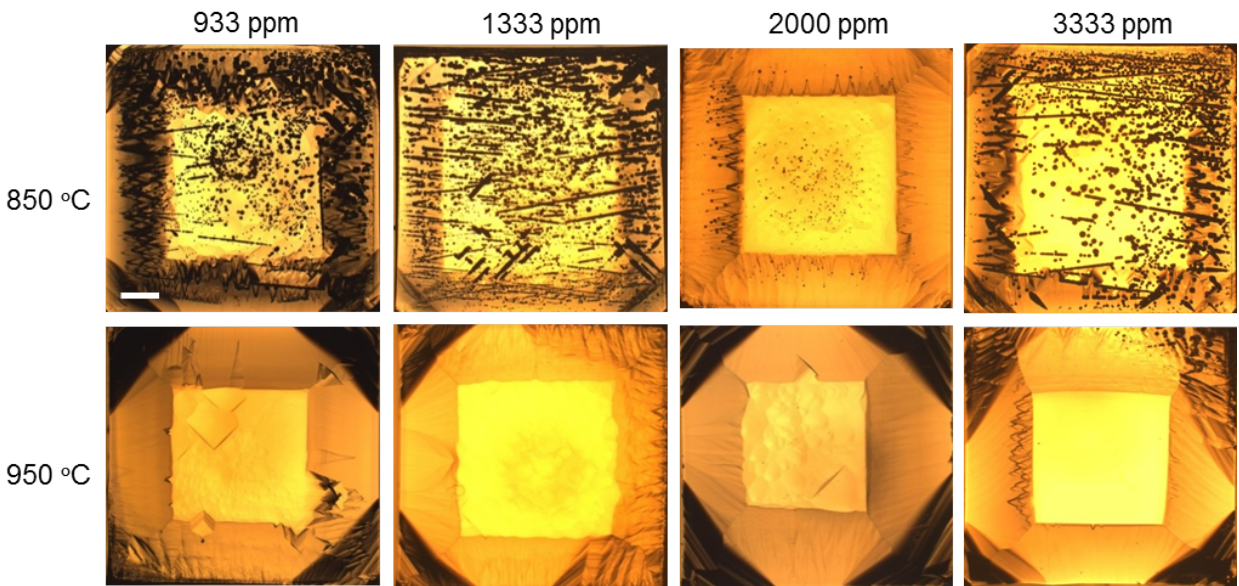


Figure 4.2 Optical micrographs, taken in reflection mode, showing the defect morphologies samples grown at 850 °C (top row) and 950 °C (bottom row). The [B]/[C] ratio in the plasma feedgas for each sample is given in the column headings. For comparison, the morphologies of samples grown at 666 ppm were shown in Figure 4.1. The scale bar for all images, in the lower left of the sample grown at 850 °C and 933 ppm, is 500 μm

4.1.2 Temperature Dependent Doping Efficiency

To determine if the substrate growth temperature had any significant effect on the plasma gas to solid phase diamond boron doping efficiency, the boron concentration as estimated by FTIR was plotted against the [B]/[C] ratio in the plasma feedgas as shown in Figure 4.4. For the same [B]/[C] ratio in the plasma gas phase, the samples grown at 950 °C show a higher level of boron incorporated into the grown films, suggesting that there is a temperature dependency to the doping efficiency. The samples grown in this work also show a higher doping level than samples from the recent work of Achard *et al.* [55], which are shown in Figure 4.4 as red triangles for comparison with the data of this investigation.

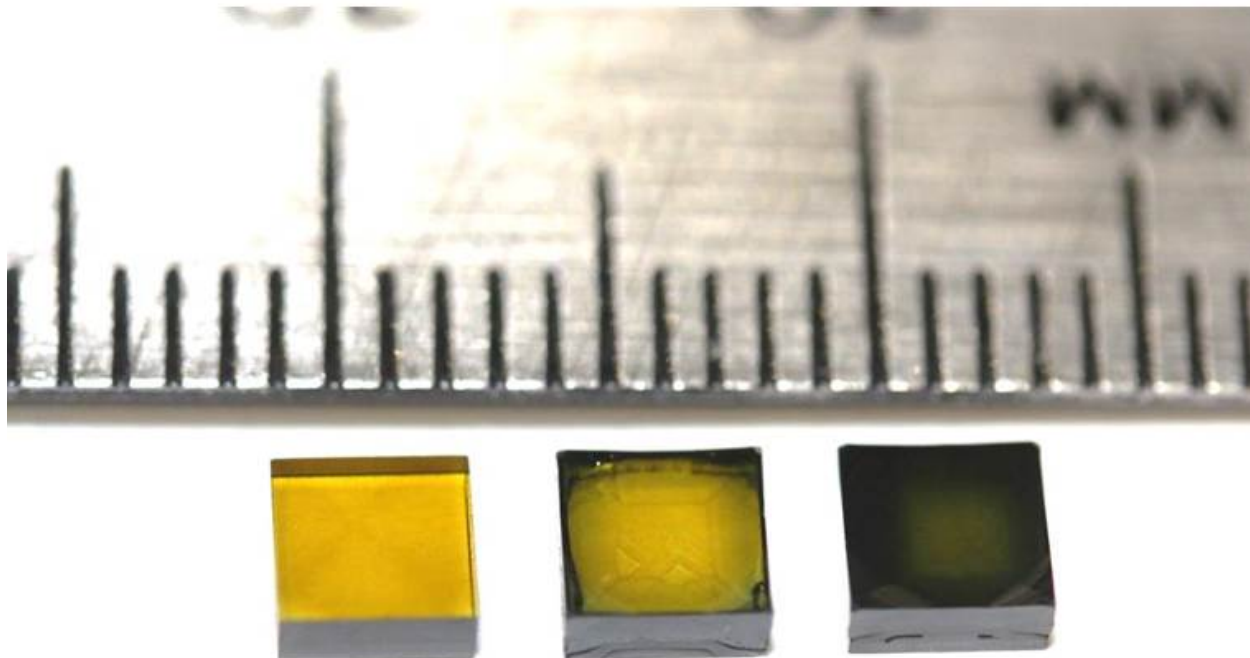


Figure 4.3 Examples of the appearances of samples of this work, shown left to right: an as received type Ib HPHT seed, sample SND22 and sample SND29

4.1.3 Temperature Dependence of the Center Growth Rate

The growth rate results given in Table 4.1 seem to indicate a temperature dependence to the sample growth rate, with the samples grown at 950°C growing slower in the center regions than the samples grown at 850°C . This is an unusual result, as the growth rate is generally seen to increase with the growth temperature. For example, Hamada *et al.* [107] saw for their undoped single crystal diamond that the growth rate increased with temperature, which they attributed to an increase in the apparent lateral growth, which also improved the crystalline quality. The mechanism by which the 950°C samples in this study grew slower in the center than the 850°C samples must therefore be a different mechanism.

The increase of the center growth rate of the 850°C samples over the 950°C samples could

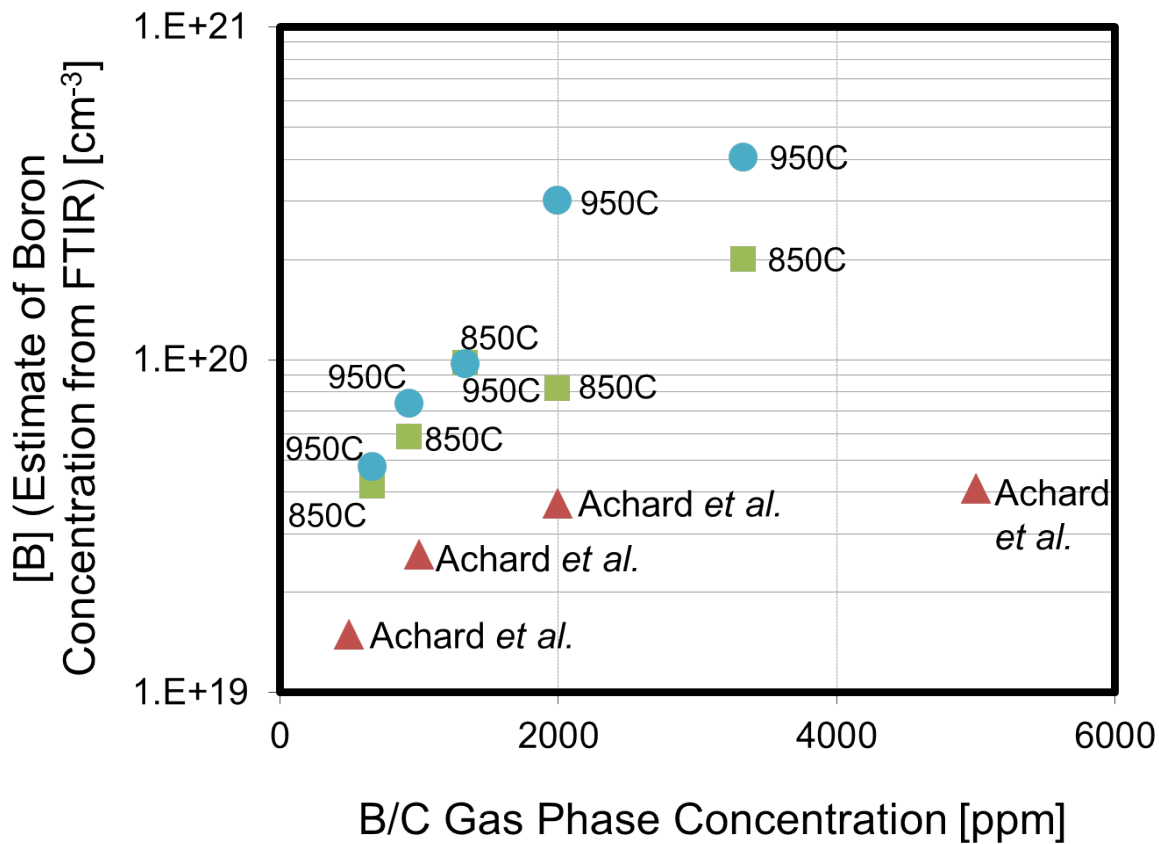


Figure 4.4 [B]/[C] ratio in the plasma gas phase vs. incorporated electrically active [B] in the grown diamond sample. This figure illustrates graphically the doping efficiency. Samples grown at 950 °C are shown with blue circles, samples grown at 850 °C are shown with green squares, and for comparison, samples from the work of Achard *et al.* [55] measured in that reference by FTIR using the same relationship of Equation (2.14) and confirmed by SIMS, are shown as red triangles.

potentially be explained with a simple model, which is related to the higher crystalline quality in the center of the 950 °C samples. The nucleation of new lattice planes is the limiting step in smooth epitaxial diamond growth, and with the absence of the unepitaxial crystallites which may provide additional nucleation sites in the center of the 950 °C samples, the samples grown at 950 °C grow slower. That the samples grown at higher temperatures are smoother, and that the samples with more defects grow faster is also consistent with results obtained by May *et al.* in Kinetic Monte Carlo modeling studies [106, 108]. In their model, increasing

the substrate growth temperature increases the migration of the carbon species across the surface, which becomes the major process by which the surface becomes smoother [106]. At higher growth temperatures the carbon species should therefore migrate more during growth, giving smoother films. This smoothing effect with increasing temperature has an apparent upper limit however, due to the formation of pyramidal hillock defects, as seen in the sample grown at 1050 °C in Figure 4.1. Additionally, when random surface defects form, which allow for the nucleation of a new growth layer, May *et al.* found that the growth rate can increase dramatically [108]. The decrease in the center growth rate with increasing temperature between the 850 °C and 950 °C samples is therefore likely due to the concomitant decrease in defects, rather than due to the increase in temperature.

4.1.4 Gas Phase Boron to Carbon Flux Ratio as a Predictor of Boron Concentration

The doping efficiencies achieved in this work are higher than those reported by Achard *et al.* [55], as seen in Figure 4.4, and understanding the cause for this disparity is important in interpreting the results of this investigation. The [B]/[C] ratio in the plasma feedgas seems to be a poor predictor of the boron concentration in the resulting diamond. With the same [B]/[C] ratio, samples could have widely varying doping concentrations, differing by as much as a factor of 10. It was discussed in Section 4.1.2 above that the substrate temperature may play a role in the doping efficiency, however the samples of Achard *et al.* were reported to have been grown at 850 °C as well, and even if there is a difference in the calibration of the actual value of the temperature measurements between the two groups, the difference in the two doping efficiencies is still likely to be too large for the temperature alone to account for

it.

A notable disparity between the samples of this work and the samples of Achard *et al.* are the differences in the growth rates of the samples of these two works. Achard *et al.* [55] report growth rates of $10 \mu\text{m h}^{-1}$, however the samples in this investigation have growth rates, given in Table 4.1, of only 1 to $5 \mu\text{m h}^{-1}$. We theorize that the rate of boron incorporation into the grown diamond film may not increase at the same rate as the total growth rate, and therefore as the growth rate increases, the doping efficiency will decrease. The relevant ratio for the estimation of boron concentration from the growth parameters could therefore be the ratio of the boron in the plasma feedgas to the flux of carbon into the grown diamond. This ratio can be found by taking the $[\text{B}]/[\text{C}]$ ratio in the plasma feedgas, and dividing it by the growth rate, thereby normalizing the carbon in the feedgas to the rate at which it is incorporated. Figure 4.5 shows the data of Figure 4.4 reinterpreted this way, using the growth rates of Table 4.1 for the samples from this investigation, and the $10 \mu\text{m h}^{-1}$ quoted in Achard *et al.* [55] for those samples. Figure 4.5 shows a much more linear relationship than Figure 4.4, suggesting that the feedgas boron to “incorporated carbon flux” (feedgas carbon multiplied by growth rate) is a more predictive measure of the boron concentration in a grown diamond film than the $[\text{B}]/[\text{C}]$ gas phase ratio alone.

4.1.5 Comparison of FTIR and SIMS for boron concentration

SIMS measurements of samples SND25, SND26, SND33 and SND 34 were performed by EAG labs, as described in Section 2.3. The results of these measurements are shown in Figure 4.7. The SIMS measurements were all performed in the center of the samples. The SIMS measurements give high boron incorporation levels, of $8.9 \times 10^{18} \text{ cm}^{-3}$ to $5.8 \times 10^{19} \text{ cm}^{-3}$. These concentrations are 5 to 8 times lower than the FTIR estimated concentrations given in

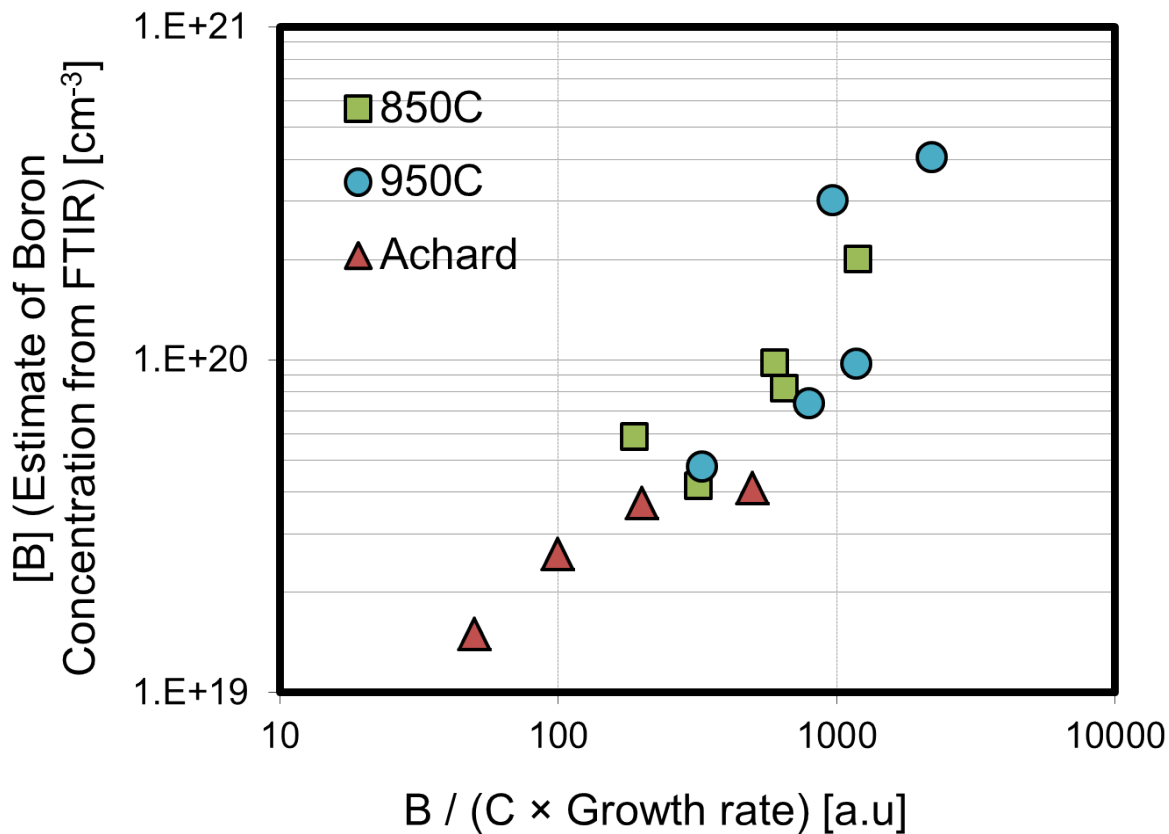


Figure 4.5 The data from Figure 4.4 is reoriented by dividing the plasma feedgas $[B]/[C]$ ratio by the growth rate. The samples of this investigation are divided by their individual growth rates, which are given in Table 4.1, and for comparison the samples of Achard *et al.* [55] are included as well, using the $10 \mu\text{m h}^{-1}$ growth rate given in that reference. A legend is given in the top left of the plot area.

Table 4.1, and this discrepancy could be due to a number of factors. The FTIR measurement could overestimate the boron concentration due to imperfect transmission through the grown samples. The slightly angled surfaces at the edges of the samples, especially those grown at 950°C , could reflect or refract the incident IR beam away from the detector beam, giving a lower IR absorption measurement. The thicker edge regions also extend slightly into the FTIR aperture window, which would further increase the absorption assumed to occur in the thinner center region. The angled edge regions may also have a higher boron incorporation level, since boron is known to preferentially incorporate on (111) facets [104] and the boron

concentration has been shown to increase with the misorientation angle from the (100) surface [109]. The transmission would also be attenuated due to the presence of defects, for example the high density of dark colored unepitaxial defects on the 850 °C samples. These sources of error in the FTIR measurement could tend to overestimate the boron concentration, and may be the reason for the discrepancy.

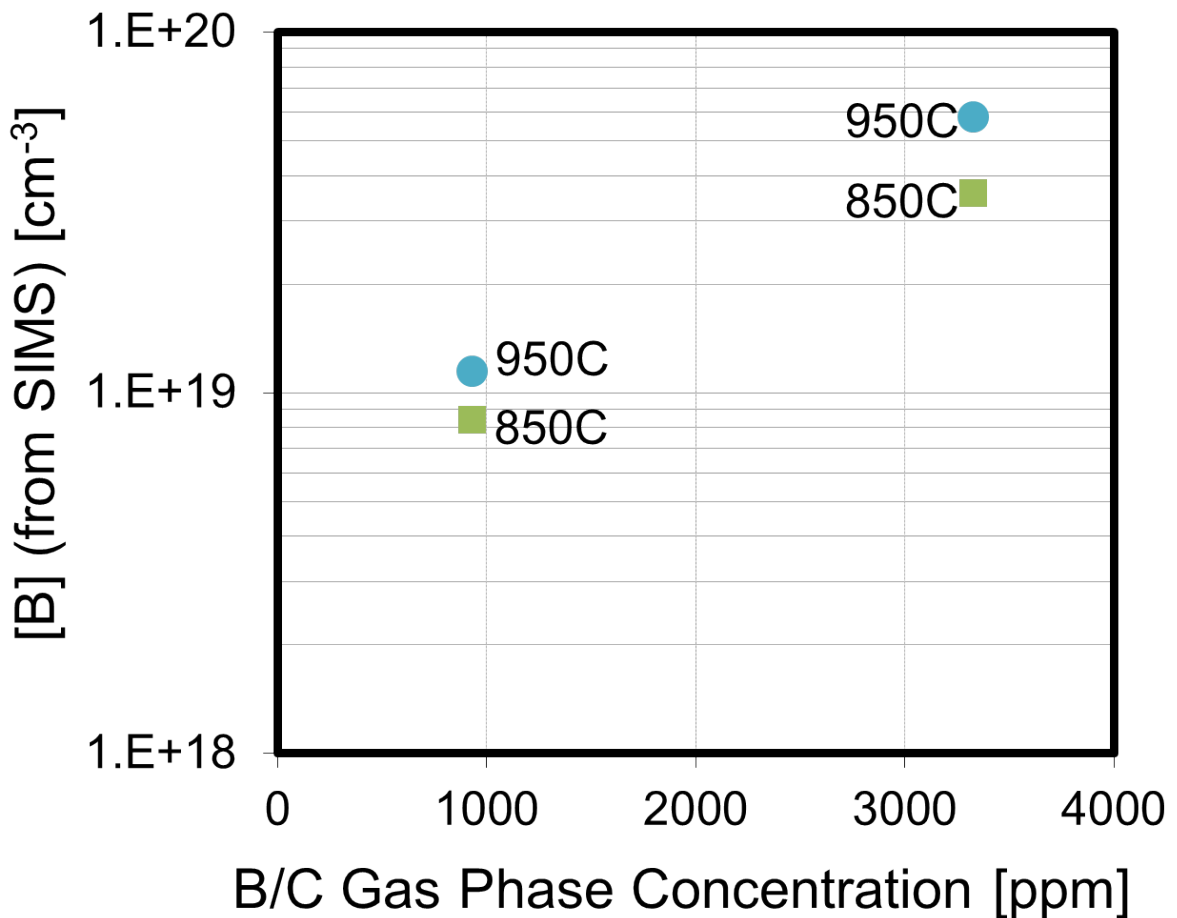


Figure 4.6 [B]/[C] ratio in the plasma gas phase vs. boron concentration in the grown diamond sample measured by SIMS (Evans Analytical Group, www.eaglabs.com). Samples grown at 950 °C are shown with blue circles, samples grown at 850 °C are shown with green squares.

In addition to the sources of possible overestimation of the boron concentration by FTIR, the SIMS calibration was performed by the commercial laboratory, and the details of this calibration and the resulting possible error quantification were not made available.

However, even if there is some error in the calibration, the SIMS boron concentrations are still comparable relative to each other. The boron concentrations measured by SIMS show the same temperature dependence of the doping efficiency that was seen in the concentrations determined by the FTIR method, with the samples grown at 950 °C showing a higher incorporation of boron than those grown at 850 °C. For example, the heavily doped sample SND34 grown at 950 °C was measured by SIMS to have 39% more incorporated boron than SND33, which was grown under the same reactor conditions but at 850 °C.

The depth profiles of the SIMS measurements are shown in Figure 4.7. The characterized samples all show good dopant uniformity across the depth of the measurement. The SIMS measurements were all taken in the center of the samples, and although the thicknesses reported in Table 4.1 are given as an average over the center regions of the samples, there may be some variation in the thickness in this region. The grown film of sample SND26 was only 7 μm thick at the point of the SIMS measurement, and the boron concentration that is shown measured after this depth is a SIMS artifact due to the high boron concentration in the grown layer.

4.2 Effect of Feedgas Flow Rate

To better understand the role of the total plasma feedgas during growth, a series of experiments were performed that varied the total flow rate, using feedgas boron-to-carbon ratios previously studied in the temperature dependence experiments of Section 4.1. In this investigation, the reactor pressure of 240 Torr and methane concentration of 3.75 % in the plasma feedgas were held constant. The pressure and methane concentrations were previously held constant at these values for the temperature dependence investigation of Section 4.1 as well. The growth

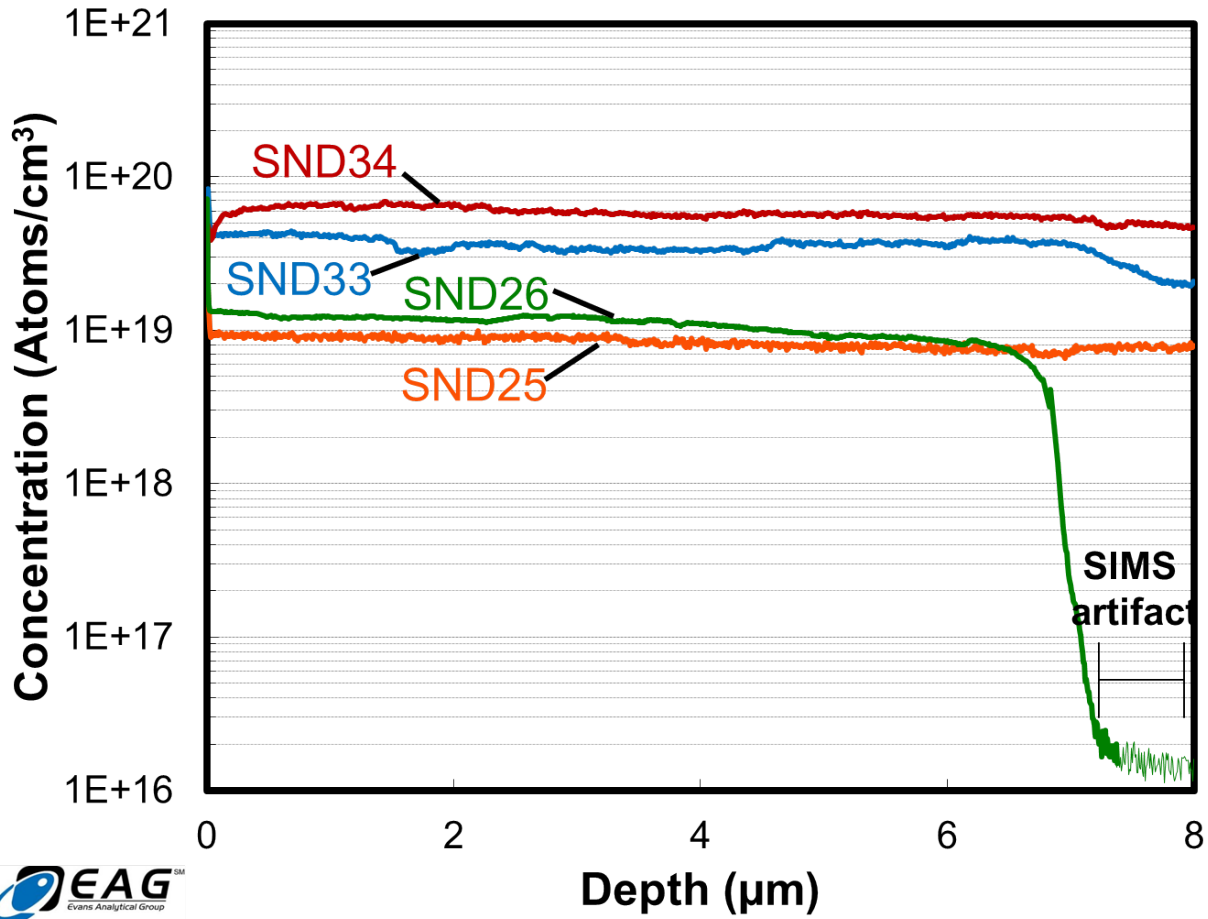


Figure 4.7 Depth profile of SIMS measurements showing uniformity of doping profile through the sample depth. The SIMS artifact of sample SND26 is due to the high boron concentration in the grown layer on top.

temperature of 950 °C and B/C feedgas ratio of 1333 ppm were also held constant. In addition to 400 sccm, which was the flow rate during the temperature dependence investigations, flow rates of 200 sccm and 800 sccm were also studied, as these flow rates are half and double the 400 sccm used in the temperature dependence investigation, and were possible gas flow rates using the existing mass flow controller set up of DS1. The deposition conditions for the experiments of this work are given in Table 4.2

The grown sample morphologies from the first three experiments in this investigation are shown in Figure 4.8. The boron concentration for these samples was estimated by FTIR using

Sample	Total plasma feedgas flow rate [sccm]	Center growth rate [$\mu\text{m h}^{-1}$]	FTIR boron concentration [cm^{-3}]
SND37	200	0.65	7.22×10^{18}
SND35	400	1.34	1.95×10^{19}
SND36	800	1.96	2.11×10^{20}
SND39	200	1.15	3.60×10^{19}
SND28	400	1.13	9.79×10^{19}
SND38	800	5.56	6.03×10^{19}

Table 4.2 Effect of Total Plasma Feedgas Flow Rate

Equation (2.14), and is given in Table 4.2. The boron concentration was seen to increase with increasing flow rate. The center growth rate for these samples also increased with increasing flow rate. This is a significant result, since it suggests a mechanism by which the growth rate and doping efficiency can be increased simultaneously, which is critical since the temperature dependence investigation of Section 4.1 found that the doping efficiency tended to drop with increasing growth rate.

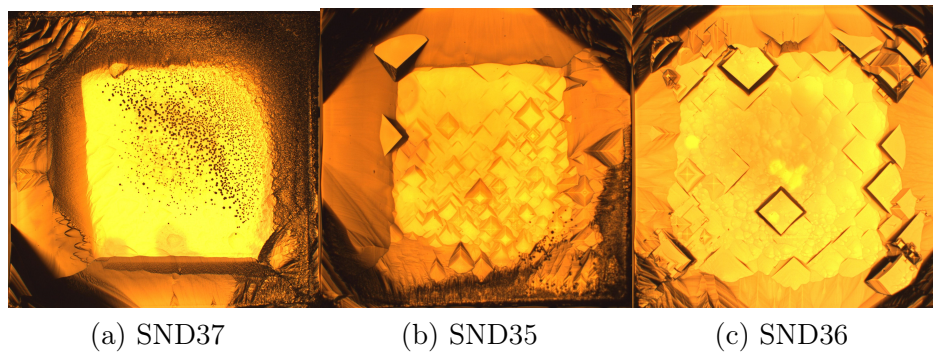


Figure 4.8 Reflection mode optical micrographs of samples grown with a low purity bell jar, with total flow rates of: (a) 200 sccm, (b) 400 sccm, (c) 800 sccm

The grown morphologies from the samples shown in Figure 4.8 had a high density of defects, significantly more than had been seen previously in the temperature dependence investigation of Section 4.1. A main difference between that investigation and this one was

the quartz bell jar used during the deposition run. The samples shown in Figure 4.8 were grown using a bell jar that was older and had been previously used to grow polycrystalline diamond. To determine if the increased defect density was due to the bell jar, an additional two experiments were performed using the quartz bell jar that had been used to grow the samples during the temperature dependence investigation. These two are shown alongside SND28, which was grown using the higher quality bell jar with the same reactor conditions during the temperature dependence investigation, in Figure 4.9.

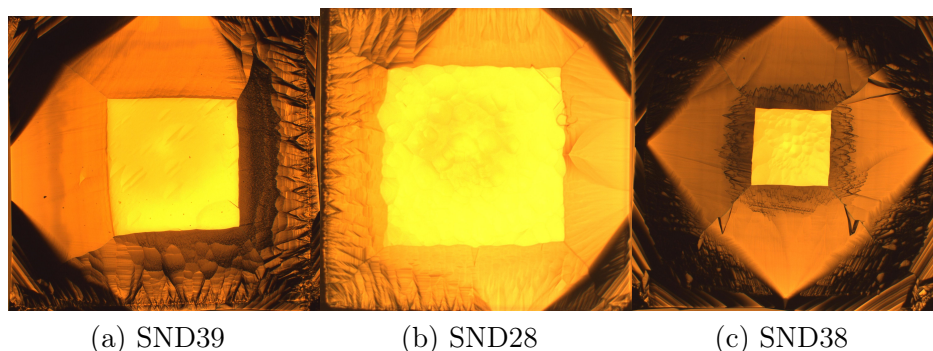


Figure 4.9 Reflection mode optical micrographs of samples grown with high quality bell jar, with total flow rates of: (a) 200 sccm, (b) 400 sccm, (c) 800 sccm

The significant improvement in the grown sample defect morphologies in Figure 4.9 indicates that the quality of the quartz bell jar plays a significant role in controlling the concentration of defects. The results of this investigation on the effect of the flow rate indicate that increasing the flow rate could be an effective strategy for improving both the doping efficiency and the growth rate.

The results of the investigations presented in this chapter show that a regime for high quality heavily boron doped diamond has been identified. Several strategies for improving the doping efficiency have also been presented, which accomplishes the aim of overcoming the difficulty of decreasing doping concentrations and a saturation of the boron concentration

that had been reported by other researchers [55].

Chapter 5

Corner-Architecture Schottky Barrier

Diodes

The successful demonstration of both high and low levels of boron doping allows for the investigation of Schottky barrier diode (SBD) structures, with the intention of optimizing their electronic properties, as discussed in Section 1.3.1. The heavily boron doped p^+ -diamond layer is essential for a high quality ohmic contact and low on-state resistance in the forward direction, and the optimization of this layer is needed for the realization of high quality SBD devices. As described in Chapter 4, a substrate growth temperature dependence for the formation of unepitaxial crystallites has been shown, which is significant, since unepitaxial crystallites are known to adversely affect SBD performance [110, 111].

The etch-pit density associated with crystalline dislocations has also been shown to be adversely related to the reverse characteristics of SBDs [111]. Further, the dependence of the reverse current on the size of the Schottky contact area, where the current increases sharply with increasing area [112], has led to the general consensus that the threading dislocations which propagate in the growth direction from the heavily boron doped layer are the primary reason for the poor reverse characteristics [113]. As was previously described

in Section 1.7.1, Friel *et al.* [54] demonstrated that growing homoepitaxial diamond in a direction perpendicular to the direction of previous epitaxial growth leads to a reduction of screw- and edge-type threading dislocations in the resulting CVD diamond film.

In this work, the method of growing perpendicular to the previous epitaxial direction will be employed for the growth of the lightly boron doped p^- active layer of an SBD, forming a corner architecture SBD. The corner architecture seeks to minimize the threading dislocations while simultaneously benefitting from an overall vertical path for the current, so as to achieve the advantages that were described in Section 1.3.2. The heavily boron doped diamond used will be SND34, which was described in Chapter 4. The lightly boron doped layer will be grown using the optimized parameters reported for sample 156_1, as described in Chapter 3.

The fabricated SBDs use gold (Au) on oxygen terminated diamond as the Schottky contacts. Au on oxygenated diamond has been the focus of several recent investigations of SBD performance, and the quality of the oxygen termination of the diamond surface has been shown to be critical for device performance, particularly at high temperatures [72, 114]. The oxygenation of the diamond surface was done by oxygen plasma treatment.

5.1 Corner Architecture Diode Fabrication

The fabrication steps necessary to produce a corner architecture SBD are shown schematically in Figure 5.1. Optical micrographs showing the realization of each of the steps of Figure 5.1 are given in Figure 5.2.

The resulting diode structure is shown in Figure 5.3. A well-designed corner diode will have a vertical path between the Schottky contact and the ohmic contact. This should give the advantage of a uniform current density in the active region of the device, and therefore

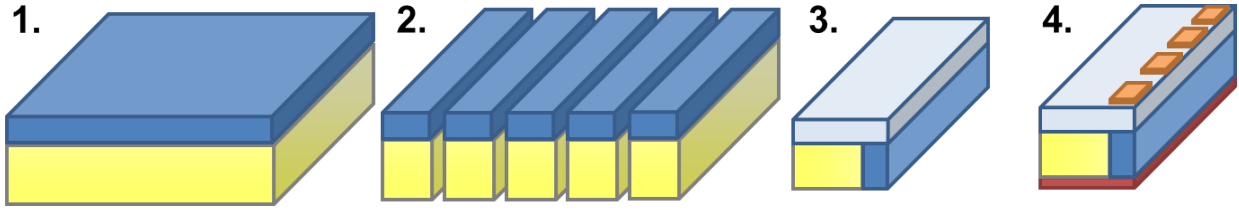


Figure 5.1 The growth steps for the fabrication of a corner architecture SBD: 1. Heavily boron doped diamond is deposited on a type Ib HPHT seed. 2. The sample is then laser-cut lengthwise and both sides of a resulting slab are polished. 3. Lightly boron-doped diamond is grown perpendicular to the direction of the previous CVD growth. 4. Schottky and ohmic contacts are deposited to form a vertically oriented SBD structure

the same benefits to the diode characteristics that should be achievable from a vertical architecture SBD.

5.1.1 Heavy Boron Doped Deposition

In step 1 of the fabrication process to produce a corner architecture diode, as shown in Figure 5.1, heavily boron doped diamond is deposited on a high pressure high temperature (HPHT) type Ib substrate. The heavily boron doped layer deposition used in this work was previously reported as sample SND34, which was described in Chapter 4.

5.1.2 Laser Cutting and Polishing

In step 2 of the fabrication process shown in Figure 5.1, the sample consisting of the heavily boron doped layer deposited on the HPHT seed from step 1 is then laser cut and polished, to produce a thin slab. Such a slab was laser cut and polished from sample SND34 for the corner diode fabricated in this work. A Bettonville Ultra Shape 5xs-IR system was used to make the laser cut. The laser is a CSI Group Nd:YAG laser with a wavelength of 1064 nm. The laser has an 18 W power output and can be focused to a spot size with a diameter less than 20 μm . The details of the laser cutting process have been recently described in [115].

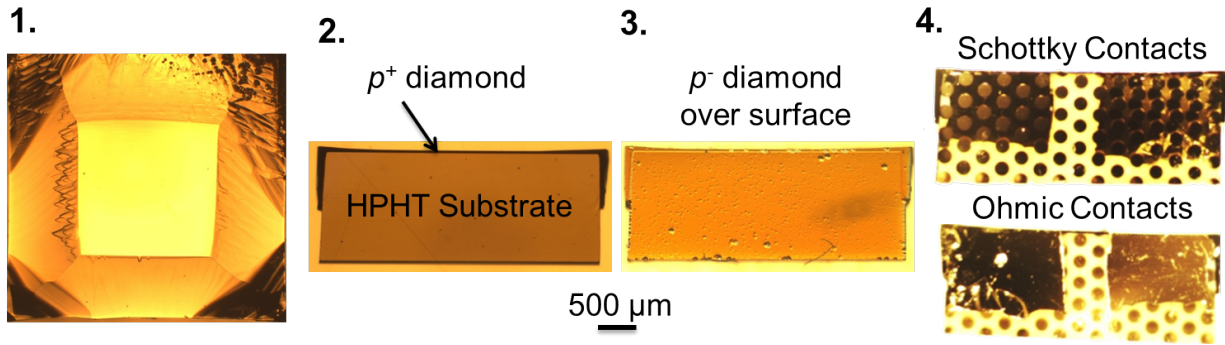


Figure 5.2 Reflection mode optical micrographs showing the actualization of the fabrication process shown in Figure 5.1: 1. Sample SND34, as described in Chapter 4, will be used for the heavily boron doped diamond on an HPHT seed. 2. A slab cut from the side of SND34 after laser cutting and polishing. This image was taken in the direction normal to the cut plane. 3. Lightly boron-doped diamond is grown perpendicular to the direction of the previous CVD growth, on top of the slab cut from sample SND34. The same optimized low boron doped growth process is used as was used for sample 156_1, which was described in Chapter 3. 4. Au Schottky and Ti/Au ohmic contacts are deposited to form a corner architecture diode structure.

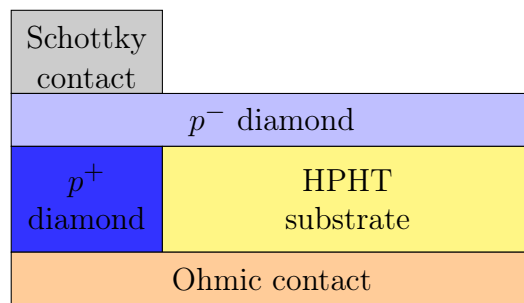


Figure 5.3 Diagram of a Corner-architecture SBD

The laser cutting was performed by Michael Becker of the Fraunhofer USA, Inc. Center for Coatings and Diamond Technologies (CCD).

The surface and subsurface damage caused by the laser cutting process are removed by mechanical polishing. Techniques used in diamond polishing have been recently described in [116]. The polishing was performed on a planetary lapping bench with a cast iron scaife seeded with diamond powder and olive oil, which rotates at 3420 rpm. Approximately 20 to 50 μm of material is ablated in the process. The resulting polished sample has an R_a of less than 10 nm. The polishing was performed by Aaron Hardy of the Fraunhofer USA, Inc.

Center for Coatings and Diamond Technologies (CCD).

The resulting slab after the laser cutting and polishing process is shown normal to the cut plane, in step 2 of Figure 5.2.

5.1.3 Lightly Boron Doped Deposition

In step 3 of the fabrication process shown in Figure 5.1, a lightly boron doped layer is grown on the slab formed in step 2. The optimized process of sample 156_1, as reported in Chapter 3, resulted in very few visible defects on the grown surface. The same growth process was therefore applied to grow the lightly boron doped layer in step 3 of Figure 5.1, and the resulting thickness is also assumed to be approximately 5 μm . The morphology of the resulting lightly boron doped diamond film on the laser cut and polished slab from step 2 of the fabrication process is shown in step 3 of Figure 5.2.

5.1.4 Contact Deposition

As described above, in step 4 of the fabrication process shown in Figure 5.1, the corner architecture SBD is formed by applying Schottky contacts to the lightly boron doped diamond layer grown in step 3, and ohmic contacts to the backside of the slab, forming a vertical architecture. The contact deposition was performed by Stephen Zajac, a graduate student at Michigan State University.

Ohmic contacts were deposited first, onto the backside of the acid cleaned sample, by sputtering Ti/Au (30 nm/300 nm thick) pads that extended to the edge of the sample, covering the thin p^+ region. The ohmic contact was formed as two individual gold pads, as a consequence of the method used to hold the sample in place during the sputtering process.

The resulting contacts were annealed under vacuum at 400 °C for 30 min.

The sample was oxygen plasma treated to oxygenate the surface, and then 300 nm thick Au Schottky contacts were applied by sputtering. Although the design of an ideal corner architecture diode would place the Schottky contacts immediately above the ohmic contact to form a vertical conduction path, as shown in Figure 5.3, additional Schottky contacts were also deposited in this work over the whole of the lightly doped layer, to give a larger number of diodes in the completed sample. In all, 67 Schottky contacts were deposited. A shadow mask of holes through metal was used for patterning without lithography steps, and the resulting Schottky contacts had a diameter of 150 μm . Optical micrographs of the sample front and back with the deposited contacts are shown in step 4 of Figure 5.2.

5.2 Diode Characterization

The electrical characterization measurements of the fabricated corner architecture SBD sample were taken by Stephen Zajac of MSU. The measurements were carried out on a Keithley 236 Source-Measure Unit, using a tungsten probe tip to probe the individual SBDs. The Au pads were contacted through a piece of copper placed beneath the sample, which was held in place by the spring force of the top probe tip. For reverse characterization above the Keithley 236 limit of approximately 100 V, the leakage current was measured as the voltage drop across a 1 M Ω resistor. The minimum voltage step measured in this way was 100 μV , (corresponding to 100 pA). This measurement was used only to check the breakdown voltage, which was taken to be the last reverse bias voltage measured before the leakage current exceeded 1 μA . An example of this characterization method is shown in Figure 5.4.

The forward characteristics were measured as a function of temperature. A 24 W ceramic

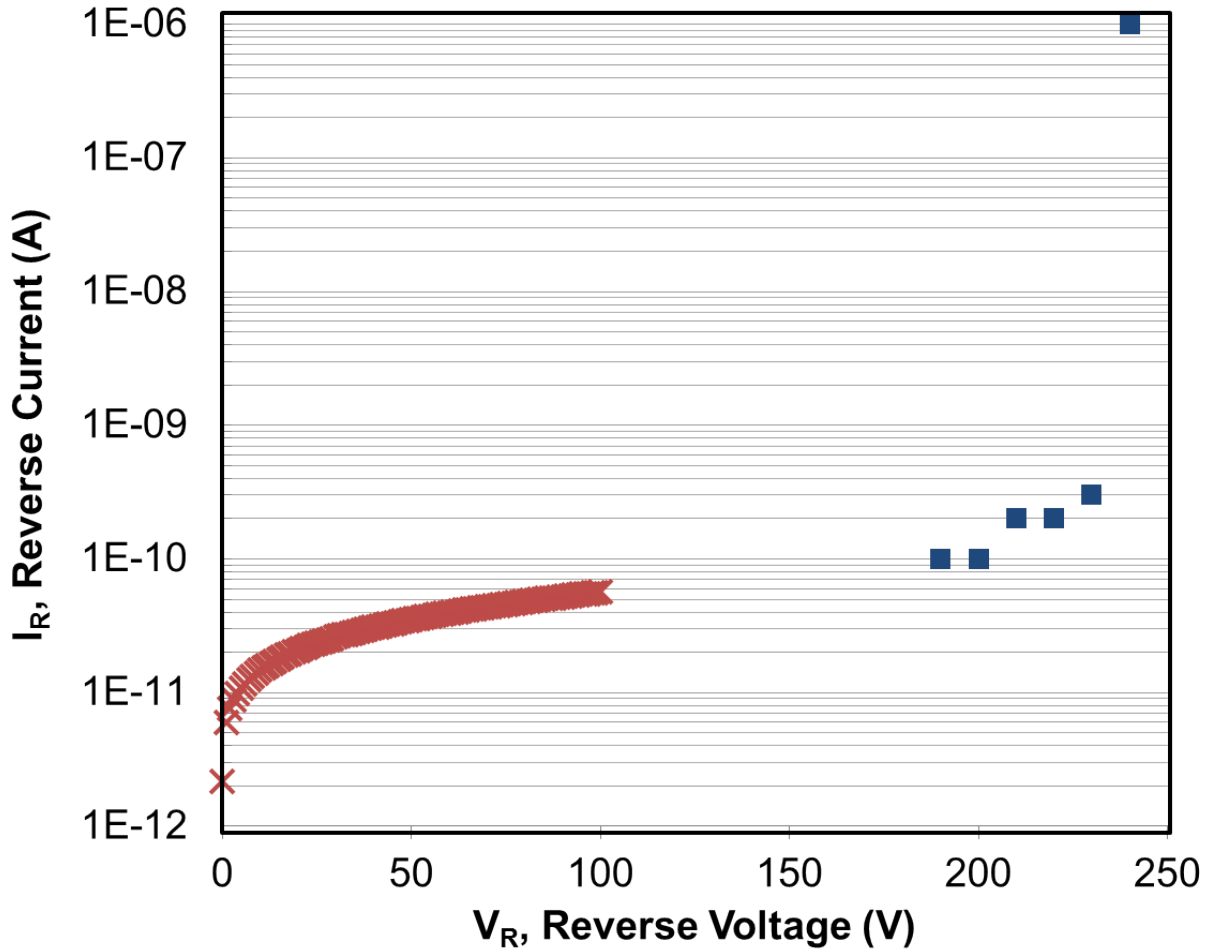


Figure 5.4 Example of the determination of the breakdown voltage of one of the SBDs. The leakage current is characterized from 0 V to 100 V with the Keithley 236. The reverse current is then checked by the voltage drop across a 1 MΩ resistor until a current above 1 μA is reached.

heater, placed under the copper bottom contact, was used as the temperature control.

The Schottky-barrier height ϕ_B and ideality factor n were determined by fitting the linear portion of the log scale current density (J) vs. forward bias voltage (V) plot, using the ideal thermionic emission SBD equation given in Equation (5.1), where A^* , T , q , and k_B , are the Richardson’s constant, absolute temperature, electron charge and Boltzmann’s constant, respectively. A value of $90 \text{ A cm}^{-2} \text{ K}^{-2}$ was assumed for A^* , as has been commonly done in

the literature [117, 118, 119].

$$J = A^*T^2 \exp\left(\frac{-q\phi_B}{k_B T}\right) \times \left[\exp\left(\frac{qV}{nk_B T}\right) - 1 \right] \quad (5.1)$$

5.2.1 Reverse Characteristics

The breakdown voltages of the 67 fabricated SBDs were measured, and are shown in Figure 5.5. Of the fabricated diodes, only three did not show diode behavior, due to shorting along the sample sides. The remaining 64 diodes showed breakdown voltages of 100-230 V.

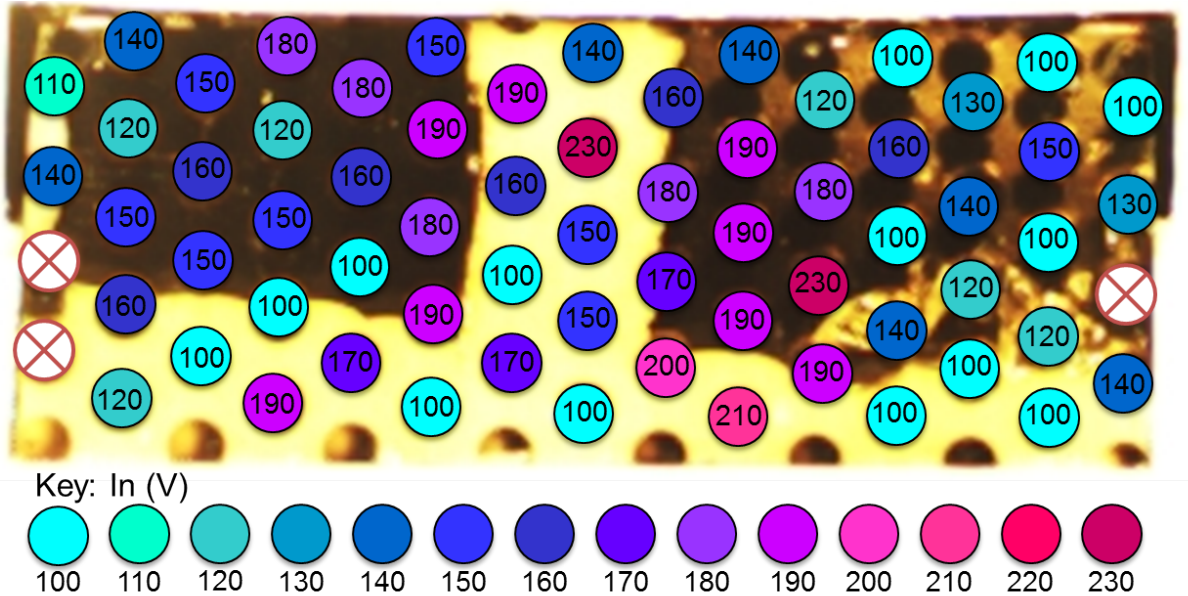


Figure 5.5 The breakdown voltage of the individual diodes, shown by superimposing a color coded circle marked with the breakdown voltage in [V] onto the location of each Schottky contact. The underlying image is the optical micrograph of the Schottky contacts from Figure 5.2. Those diodes marked with an \otimes were shorted to the backside contact along the sample sides, and did not show diode behavior.

5.2.2 Position Dependence of Diode Performance

The corner architecture diodes fabricated in this work used an HPHT/ p^+ -slab with a thin p^+ -layer of only $11.4\mu\text{m}$ at the center. As a result, none of the $150\mu\text{m}$ diameter SBD contacts were able to be fully overlapping the p^+ -layer, as would be the case in an ideal corner architecture. The diode characteristics, particularly in the forward direction, are sensitive to the distance from the heavily doped p^+ -layer. The diodes numbered 7 and 12-15, enclosed in the red box in Figure 5.6, for example, show increasing on resistance, R_{ON} , as the distance from the top heavily doped region increases, as shown in Figure 5.7. The diodes numbered 1-11, which overlapped the most with the heavily doped p^+ -layer, showed the best forward characteristics. As expected, the thickness of the p^+ -layer near the diode is also important, for example, diode 10, which is slightly overlapping a thick region of the p^+ -layer, showed the best forward characteristics of the diodes studied.

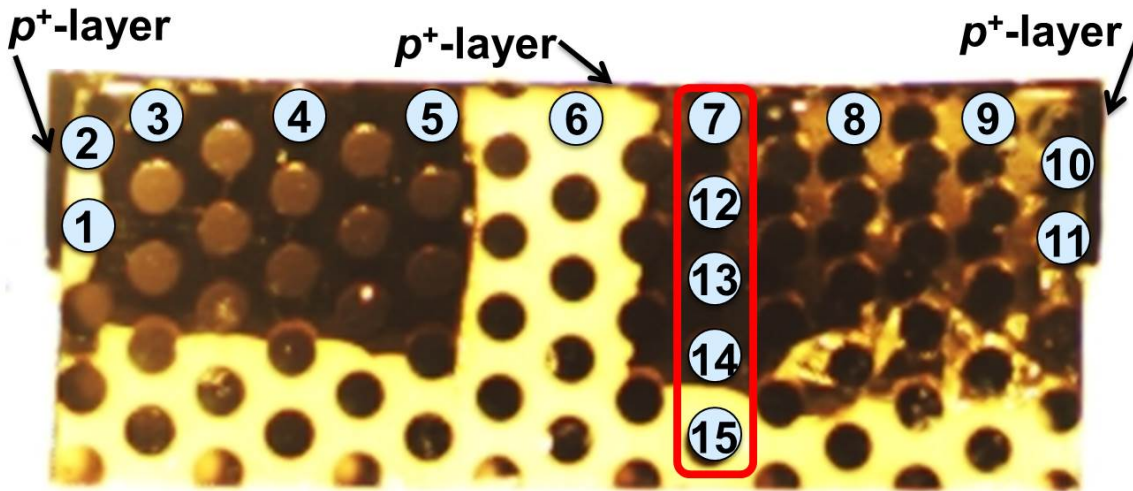


Figure 5.6 Several of the 64 working SBD contacts are numbered for reference in the text. The location of the heavily doped p^+ -layer is indicated, along the top surface. The underlying image is the optical micrograph of the Schottky contacts from Figure 5.2.

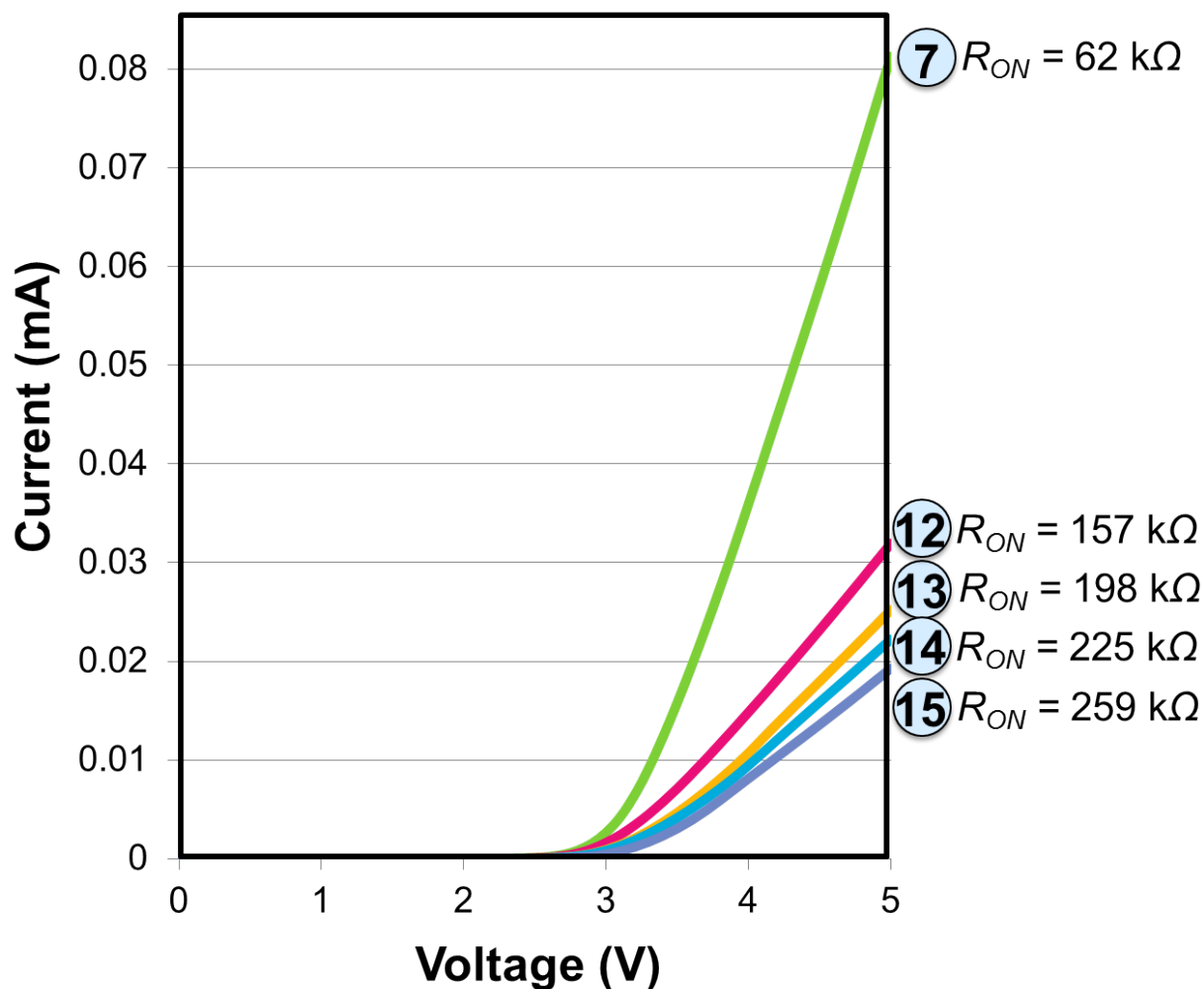


Figure 5.7 The $I - V$ characteristics of diodes numbered 7 and 12-15, which are enclosed in the red box in Figure 5.6. The on-state resistance, R_{ON} , shown next to the diode number, is calculated at 5 V.

5.2.3 Ideality Factor and Rectification Ratio

The rectification ratio is the ratio of the on-state current to the reverse leakage current at the same absolute voltage. A high rectification ratio of 1.6×10^9 at $|8 \text{ V}|$ was achieved, as shown in Figure 5.8 for diode 10 (shown in Figure 5.6), at room temperature. The linear fitting line for ϕ_B and n is also shown. The ideality factor for this diode was 3.42, which is substantially different from 1, the ideality factor of an ideal diode. However, the diode displayed low

off-state leakage currents in the 1×10^{-11} A range and high on-state forward currents above 10 mA, even at room temperature. It is expected that the forward characteristics would improve with a thicker p^+ -layer.

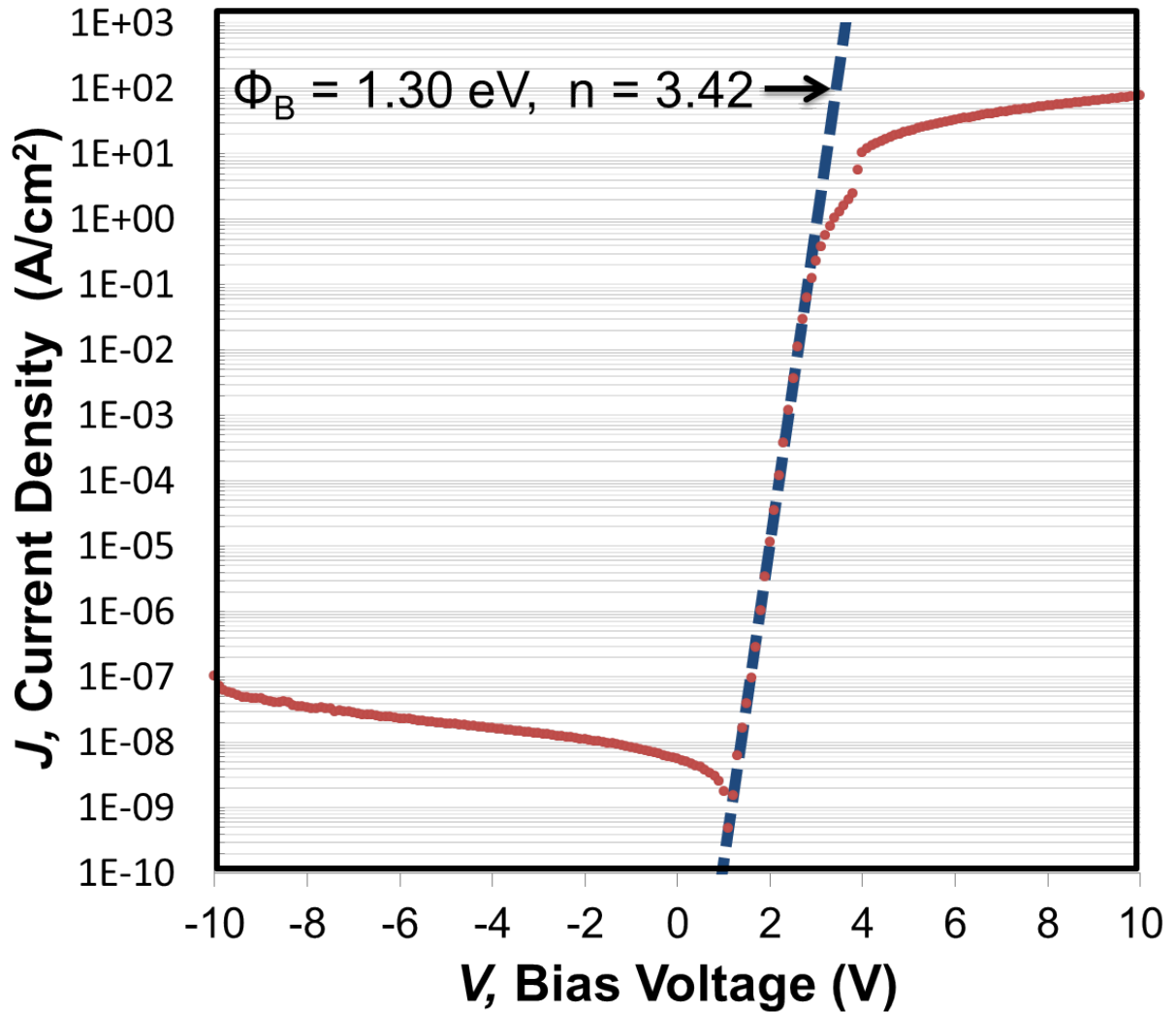


Figure 5.8 Example of the determination of the Schottky-barrier height ϕ_B , and ideality factor n by linear fitting to the diode curve of diode 10 (shown in Figure 5.6), at room temperature. The rectification ratio of 1.6×10^9 at $|8 \text{ V}|$ is also determined from this plot.

5.2.4 Forward Characteristics

The forward characteristics of diode 10 (shown in Figure 5.6), were measured at each of seven temperatures, and the resulting forward $I - V$ curves are shown in Figure 5.9. The on-state resistance decreases with increasing temperature, and the forward current increases. At 8 V and 273 °C, a high forward current above the Keithley 236 limit of 100 mA is achieved.

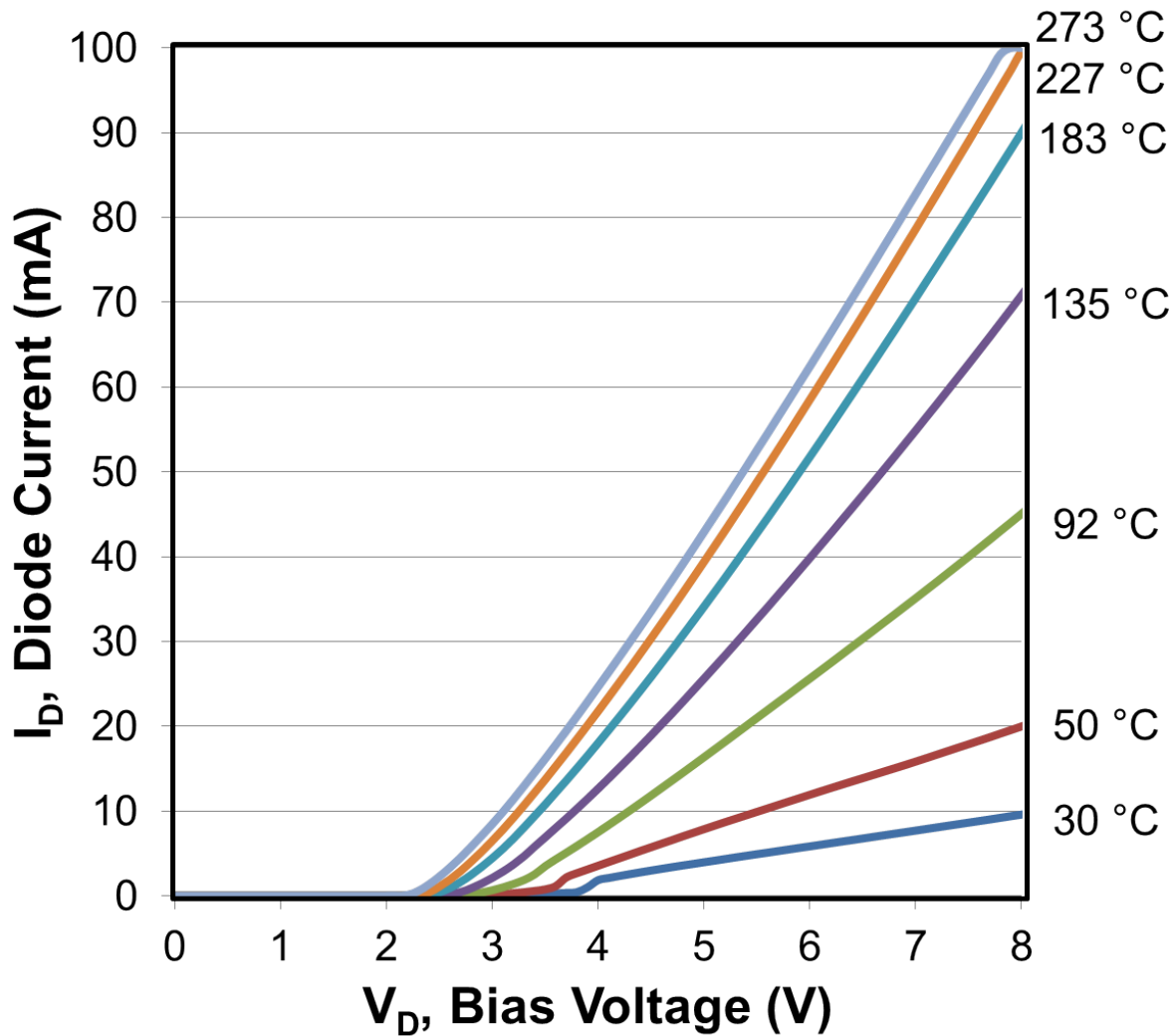


Figure 5.9 The temperature dependent forward characteristics of diode 10 from Figure 5.6 is shown. The current increases with increasing temperature, and the on-state resistance decreases. High forward currents in the mA range, up to above the Keithley 236 limit of 100 mA are achieved.

The ideality factors n and Schottky-barrier heights ϕ_B for the temperature series shown

in Figure 5.9 are shown in Figure 5.10. As the temperature increased, the ideality factor initially decreased from 3.4 to 2.5 for temperatures from 30 °C to 183 °C. As the temperature increased up to 273 °C, n then slightly increased up to 2.8. For the temperature range measured, the Schottky-barrier height increased from 1.30 eV to 1.65 eV. This overall trend is similar to what has been reported in the literature [117, 119]. The slight increase in n at higher temperatures has been proposed to be caused by SBH inhomogeneity [119].

By keeping a substantial portion of the original insulating HPHT seed attached to the heavily boron doped layer, a diode can be fabricated from a much thinner p^+ deposition. This was demonstrated in this example corner architecture diode, where the p^+ -layer was only about 11 μm thick in the center. The realization of a vertical architecture without needing to grow approximately 300 μm thick heavily doped diamond to create freestanding substrates is a significant result.

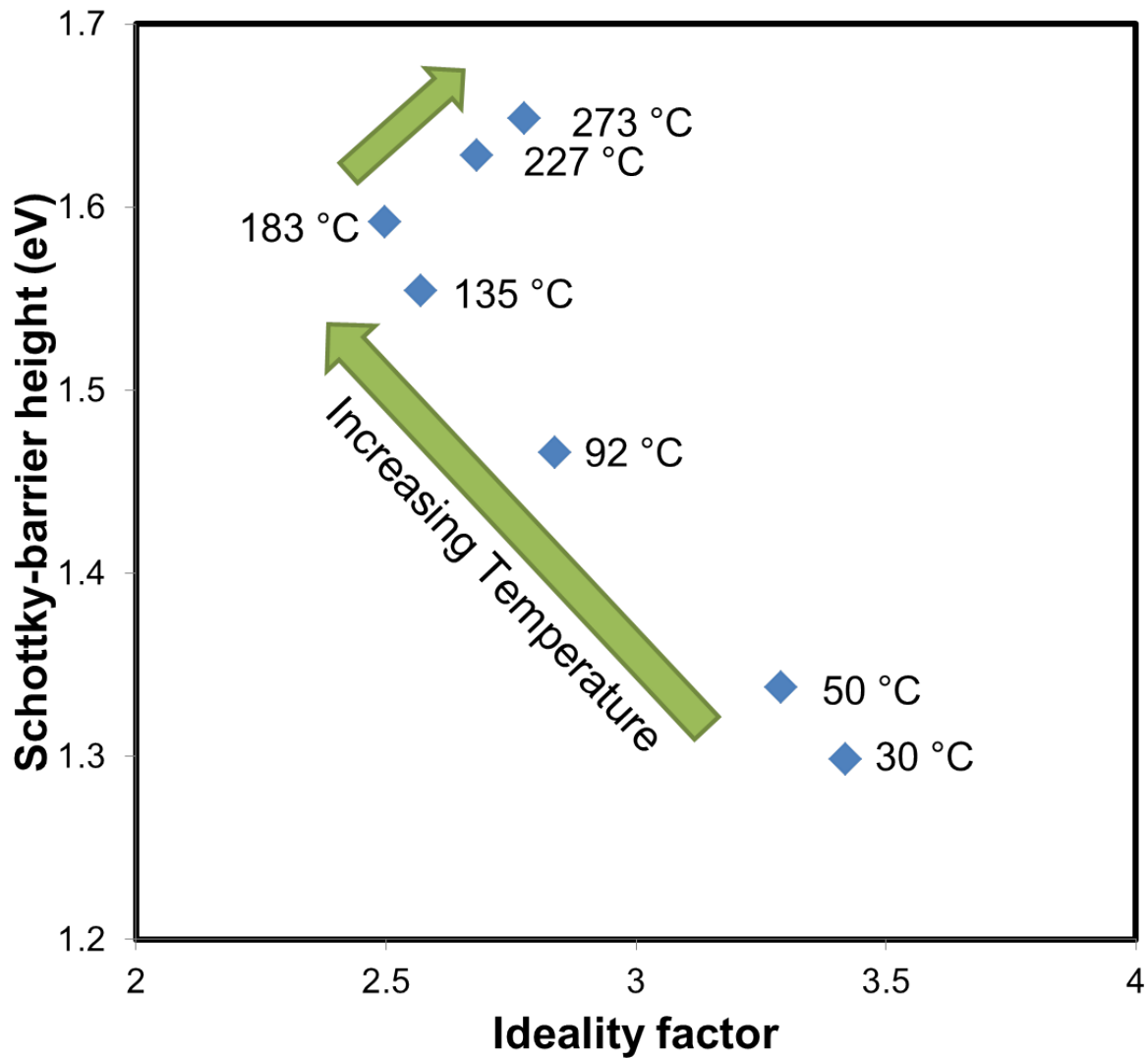


Figure 5.10 The ideality factors n and Schottky-barrier heights, ϕ_B , fitted from the temperature varied series of diode measurements shown in Figure 5.9. The trend of the Schottky-barrier height increasing and the ideality factor initially decreasing, and then subsequently slightly increasing with increasing temperature is noted by the green arrows.

Chapter 6

Summary and Conclusions

The objectives of this dissertation research, as given in Section 1.1, were the following:

1. To control the doping concentration of lightly boron doped diamond by reducing the boron concentration in grown films.
2. To improve the doping efficiency at high boron doping levels.
3. To identify regimes for high quality diamond growth that minimize the number of defects that form at both high and low doping levels.
4. To fabricate and characterize a SBD utilizing these optimized regimes, with an architecture designed to improve the diode characteristics of diamond devices.

This chapter will address the success of this work in meeting these objectives by summarizing the major results of this dissertation. The success of achieving objective 1 will be summarized in Section 6.1. Objective 2 will be addressed in Section 6.2. Sections 6.1 and 6.2 will also address the achievement of objective 3. The completion of objective 4 will be summarized in Section 6.3. The overall conclusions of this work will be given in Section 6.4.

6.1 Low Level Boron Doping

The results of this dissertation research for low level boron doping were presented in Chapter 3. The experiments performed were aimed at identifying a regime for high quality single crystal diamond with a repeatable, low concentration of boron for electronic applications. Initial experiments indicated that the reactor memory effect was a significant effect causing a high level of unintentional doping in samples grown in DS1. Several growth experiments attempted to reduce the boron content in samples grown in DS1 by including CO₂ in the reactor plasma feedgas. High concentrations of CO₂ (3.5%) reduced the boron content below measurable levels, however etching became the dominant effect, especially at higher pressure (160 Torr). Grown samples were characterized with FTIR and temperature dependent four point probe. Minimizing grown defects was found to be crucial for controlling the dopant uniformity. Without a method for reducing the unintentional doping, the reactor memory effect was found to be a significant effect for samples grown in DS1. To achieve the objectives of this dissertation research it was therefore necessary to use a dedicated diamond deposition system for lightly boron doped diamond. As a result, DS6 was designed and constructed, as detailed in Section 2.1.2. By using this new reactor exclusively for lightly boron doped diamond, the reactor memory effect is significantly reduced, achieving the objective of reducing the boron concentration of lightly boron doped diamond films. With the verification of high quality diamond deposition in DS6, the objective of determining a growth regime for lightly boron doped diamond for electronic applications was achieved.

6.2 Heavy Boron Doping

The heavily boron doped diamond deposition results were given in Chapter 4. One of the aims of this work was to increase the doping efficiency. The decreasing of the doping efficiency with increasing B/C gas phase ratios had been reported in the literature by Achard *et al.* [55] and others as a significant problem for heavily boron doped diamond deposition, as described in Section 1.7.5. One major difference between the work of Achard *et al.* and the work performed early in this dissertation research was that Achard *et al.* had reported a lower sample deposition temperature (850 °C) than the typical deposition temperature that was used at MSU on DS1 for boron doped diamond growth. To determine if the substrate temperature had a significant effect on the doping efficiency, a series of growth experiments that varied the B/C ratio in the plasma feedgas at two different temperatures was performed. This investigation found that samples grown in DS1 at 950 °C showed a higher doping efficiency and a significant reduction of visible defects compared to samples grown at 850 °C. The growth rate was also seen to affect the doping efficiency, and a plot of the boron-to-carbon flux into the sample, obtained by dividing the B/C gas phase ratio by the growth rate, was found to be much more predictive of the boron concentration than the gas phase B/C ratio alone. The total reactor feedgas flow rate was also investigated, and the growth rate and doping efficiency were both found to increase with increasing flow rate. These investigations achieved the objectives of this dissertation work for heavily boron doped diamond, doping efficiency was improved and the grown defects were minimized by optimizing the growth temperature and flow rate.

6.3 Corner Architecture SBD

The results of this dissertation work on the corner architecture SBD were presented in Chapter 5. The final objective of this dissertation research was to use the optimized growth regimes for both lightly boron doped and heavily boron doped diamond to fabricate a diode structure. The corner architecture SBD was proposed for the first time as a part of this dissertation research, as an alternative vertical diode structure designed to have the benefits of the vertical current path of a vertical architecture SBD, as were described in Section 1.3.2. The corner architecture SBD is also designed to minimize the threading dislocations in the lightly doped active layer of the device, by growing in a direction perpendicular to the direction of the heavily boron doped epitaxial growth, as described in Section 1.7.1. The fabrication and characterization of the first example of a corner architecture diode was completed as a part of this dissertation research, achieving this objective.

6.4 Conclusions of this Work

A significant contribution of the experiments performed in this work is the description of the complicated interaction of growth parameters, such as pressure, substrate temperature, flow rate, and gas composition, on the parameters of interest in boron doped diamond, namely the growth rate, defect morphology and boron concentration in the grown diamond. By studying these parameters, regimes for high quality diamond at both high and low levels of boron incorporation have been identified. This work also included the construction of a new dedicated lightly boron doped electronic grade SCD deposition system, DS6, and the design, fabrication and characterization of the corner architecture SBD. The results of this thesis therefore represent a significant contribution to the field of diamond growth and electronics.

REFERENCES

REFERENCES

- [1] J.E. Field. *The Properties of Natural and Synthetic Diamond*. Academic Press, 1992.
- [2] Paul W May. Diamond thin films: a 21st-century material. *Philosophical Transactions of the Royal Society of London. Series A: Mathematical, Physical and Engineering Sciences*, 358(1766):473–495, 2000.
- [3] Tokuyuki Teraji. Chemical vapor deposition of homoepitaxial diamond films. *physica status solidi (a)*, 203(13):3324–3357, 2006.
- [4] Chris J.H. Wort and Richard S. Balmer. Diamond as an electronic material. *Materials Today*, 11:22 – 28, 2008.
- [5] E. Johnson. Physical limitations on frequency and power parameters of transistors. In *IRE International Convention Record*, volume 13, pages 27–34, March 1965.
- [6] R.W. Keyes. Figure of merit for semiconductors for high-speed switches. *Proceedings of the IEEE*, 60(2):225–225, Feb 1972.
- [7] B. J. Baliga. Semiconductors for high voltage, vertical channel field effect transistors. *Journal of Applied Physics*, 53(3):1759–1764, 1982.
- [8] A.A. Lebedev and V.E. Chelnokov. Wide-gap semiconductors for high-power electronics. *Semiconductors*, 33(9):999–1001, 1999.
- [9] B. Jayant Baliga. *Advanced Power Rectifier Concepts*. Springer US, 2009.
- [10] Simon M. Sze and Kwok K. Ng. *Physics of Semiconductor Devices*. Wiley, 2006.
- [11] D. Takeuchi, S. Yamanaka, H. Watanabe, and H. Okushi. Device grade b-doped homoepitaxial diamond thin films. *physica status solidi (a)*, 186(2):269–280, 2001.
- [12] K. Kobashi. *Diamond Films: Chemical Vapor Deposition for Oriented and Heteroepitaxial Growth*. London, 2005.
- [13] S. Koizumi. Growth and characterization of phosphorus doped n-type diamond thin films. *physica status solidi (a)*, 172(1):71–78, 1999.

- [14] E Gheeraert, S Koizumi, T Teraji, and H Kanda. Electronic transitions of electrons bound to phosphorus donors in diamond. *Solid State Communications*, 113(10):577 – 580, 2000.
- [15] R.G. Farrer. On the substitutional nitrogen donor in diamond. *Solid State Communications*, 7(9):685 – 688, 1969.
- [16] P. W. Bridgman. An experimental contribution to the problem of diamond synthesis. *The Journal of Chemical Physics*, 15(2):92–98, 1947.
- [17] F. P. Bundy, H. T. Hall, H. M. Strong, and R. H. Wentorf Jr. Man-made diamond. *Nature*, 176:51–55, 1955.
- [18] H. P. Bovenkerk, F. P. Bundy, R. M. Chrenko, P. J. Codella, H. M. Strong, and R. H. Wentorf. Errors in diamond synthesis. *Nature*, 365:19, 1993.
- [19] H. P. Bovenkerk, F. P. Bundy, H. T. Hall, H. M. Strong, and R. H. Wentorf Jr. Preparation of diamond. *Nature*, 184:1094–1098, 1959.
- [20] A.R. Ubbelohde and F.A. Lewis. *Graphite and its crystal compounds*. Clarendon Press, 1960.
- [21] J.J. Lander and J. Morrison. Low energy electron diffraction study of the (111) diamond surface. *Surface Science*, 4(3):241 – 246, 1966.
- [22] John C. Angus, Herbert A. Will, and Wayne S. Stanko. Growth of diamond seed crystals by vapor deposition. *Journal of Applied Physics*, 39(6):2915–2922, 1968.
- [23] J.A. Brinkman, H.M. Dieckamp, and C.J. Meechan. Method for artificial synthesis of diamonds, July 28 1964. US Patent 3,142,539.
- [24] William G. Eversole. Synthesis of diamond, 1962. US Patent 3,030,188.
- [25] B.V. Derjaguin, D.V. Fedoseev, V.M. Lukyanovich, B.V. Spitzin, V.A. Ryabov, and A.V. Lavrentyev. Filamentary diamond crystals. *Journal of Crystal Growth*, 2(6):380 – 384, 1968.
- [26] B. V. Deryagin, B. V. Spitsyn, L. L. Builov, A. A. Klochkov, A. E. Gorodetskii, and A. V. Smol’Yaninov. Diamond crystal synthesis on nondiamond substrates. *Soviet Physics Doklady*, 21:676, November 1976.

- [27] B.V. Spitsyn, L.L. Bouilov, and B.V. Derjaguin. Vapor growth of diamond on diamond and other surfaces. *Journal of Crystal Growth*, 52, Part 1(0):219 – 226, 1981.
- [28] Seiichiro Matsumoto, Yoichiro Sato, Mutsukazu Kamo, and Nobuo Setaka. Vapor deposition of diamond particles from methane. *Japanese Journal of Applied Physics*, 21:L183–L185, April 1982.
- [29] Seiichiro Matsumoto, Yoichiro Sato, Masayuki Tsutsumi, and Nobuo Setaka. Growth of diamond particles from methane-hydrogen gas. *Journal of Materials Science*, 17(11):3106–3112, 1982.
- [30] Mutsukazu Kamo, Yoichiro Sato, Seiichiro Matsumoto, and Nobuo Setaka. Diamond synthesis from gas phase in microwave plasma. *Journal of Crystal Growth*, 62(3):642 – 644, 1983.
- [31] Yukio Saito, Shinpe Matsuda, and Shunsuke Nogita. Synthesis of diamond by decomposition of methane in microwave plasma. *Journal of Materials Science Letters*, 5(5):565–568, 1986.
- [32] P. K. Bachmann, W. Drawl, D. Knight, R. Weimer, and R.F. Messier. Diamond and diamond-like material synthesis. pages 99–112. Materials Research Society, Pittsburgh, PA, 1988.
- [33] Y. Liou, A. Inspektor, R. Weimer, and R. Messier. Low-temperature diamond deposition by microwave plasma-enhanced chemical vapor deposition. *Applied Physics Letters*, 55(7):631–633, 1989.
- [34] J. Asmussen and J.J. Root. Ion generating apparatus and method for the use thereof, March 26 1985. US Patent 4,507,588.
- [35] J. Asmussen and D.K. Reinhard. Microwave or uhf plasma improved apparatus, December 23 1986. US Patent 4,630,566.
- [36] J. Asmussen and D.K. Reinhard. Ultrahigh frequency, integrated circuits, April 29 1986. US Patent 4,585,668.
- [37] T.A. Roppel, J. Asmussen, and D.K. Reinhard. Dual plasma microwave apparatus and method for treating a surface, September 8 1987. US Patent 4,691,662.
- [38] J. Asmussen, D.K. Reinhard, and M. Dahimene. Plasma generating apparatus using magnets and method, February 23 1988. US Patent 4,727,293.

- [39] J. Asmussen. Method for treating a material using radiofrequency waves, October 11 1988. US Patent 4,777,336.
- [40] J. Asmussen. Microwave apparatus, December 20 1988. US Patent 4,792,772.
- [41] Joseph Root and Jes Asmussen. Experimental performance of a microwave cavity plasma disk ion source. *Review of Scientific Instruments*, 56(8):1511–1519, 1985.
- [42] T. Roppel, D. K. Reinhard, and J. Asmussen. Low temperature oxidation of silicon using a microwave plasma disk source. *Journal of Vacuum Science & Technology B*, 4(1):295–298, 1986.
- [43] J. Asmussen and M. Dahimene. The experimental test of a microwave ion beam source in oxygen. *Journal of Vacuum Science & Technology B*, 5(1):328–331, 1987.
- [44] Jes Asmussen. Electron cyclotron resonance microwave discharges for etching and thin-film deposition. *Journal of Vacuum Science & Technology A*, 7(3):883–893, 1989.
- [45] Jie Zhang. *Experimental development of microwave cavity plasma reactors for large area and high rate diamond film deposition*. PhD thesis, Michigan State University. Department of Electrical Engineering, 1993.
- [46] J. Zhang, B. Huang, D. K. Reinhard, and J. Asmussen. An investigation of electromagnetic field patterns during microwave plasma diamond thin film deposition. *Journal of Vacuum Science & Technology A*, 8(3):2124–2128, 1990.
- [47] S. Khatami. *Controlled synthesis of diamond films using a microwave discharge (non-equilibrium plasma)*. PhD thesis, Michigan State University, 1997.
- [48] K.-P. Kuo. *Microwave-assisted plasma CVD of diamond films using thermal-like plasma discharge*. PhD thesis, Michigan State University, 1997.
- [49] Kuo-Ping Kuo and Jes Asmussen. An experimental study of high pressure synthesis of diamond films using a microwave cavity plasma reactor. *Diamond and Related Materials*, 6(9):1097 – 1105, 1997.
- [50] R. Ramamurti, M. Becker, T. Schuelke, T. Grotjohn, D. Reinhard, G. Swain, and J. Asmussen. Boron doped diamond deposited by microwave plasma-assisted {CVD} at low and high pressures. *Diamond and Related Materials*, 17:481 – 485, 2008. {NDNC} 2007 Proceedings of the International Conference on New Diamond and Nano Carbons 2007.

- [51] R. Ramamurti, M. Becker, T. Schuelke, T. Grotjohn, D. Reinhard, and J. Asmussen. Synthesis of boron-doped homoepitaxial single crystal diamond by microwave plasma chemical vapor deposition. *Diamond and Related Materials*, 17:1320 – 1323, 2008. Proceedings of Diamond 2007, the 18th European Conference on Diamond, Diamond-Like Materials, Carbon Nanotubes, Nitrides and Silicon Carbide Diamond 2006 Proceedings of Diamond 2007, the 18th European Conference on Diamond, Diamond-Like Materials, Carbon Nanotubes, Nitrides and Silicon Carbide.
- [52] R. Ramamurti, M. Becker, T. Schuelke, T.A. Grotjohn, D.K. Reinhard, and J. Asmussen. Deposition of thick boron-doped homoepitaxial single crystal diamond by microwave plasma chemical vapor deposition. *Diamond and Related Materials*, 18:704 – 706, 2009. Proceedings of Diamond 2008, the 19th European Conference on Diamond, Diamond-Like Materials, Carbon Nanotubes, Nitrides and Silicon Carbide.
- [53] Hitoshi Umezawa, Natsuo Tatsumi, Yukako Kato, and Shinichi Shikata. Leakage current analysis of diamond schottky barrier diodes by defect imaging. *Diamond and Related Materials*, 40(0):56 – 59, 2013.
- [54] I. Friel, S.L. Clewes, H.K. Dhillon, N. Perkins, D.J. Twitchen, and G.A. Scarsbrook. Control of surface and bulk crystalline quality in single crystal diamond grown by chemical vapour deposition. *Diamond and Related Materials*, 18:808 – 815, 2009.
- [55] J. Achard, R. Issaoui, A. Tallaire, F. Silva, J. Barjon, F. Jomard, and A. Gicquel. Freestanding cvd boron doped diamond single crystals: A substrate for vertical power electronic devices? *physica status solidi (a)*, 209(9):1651–1658, 2012.
- [56] Norio Tokuda, Hitoshi Umezawa, Takeyasu Saito, Kikuo Yamabe, Hideyo Okushi, and Satoshi Yamasaki. Surface roughening of diamond (001) films during homoepitaxial growth in heavy boron doping. *Diamond and Related Materials*, 16:767 – 770, 2007. Proceedings of Diamond 2006, the 17th European Conference on Diamond, Diamond-Like Materials, Carbon Nanotubes, Nitrides and Silicon Carbide Diamond 2006.
- [57] J. Achard, F. Silva, R. Issaoui, O. Brinza, A. Tallaire, H. Schneider, K. Isoird, H. Ding, S. Kone, M.A. Pinault, F. Jomard, and A. Gicquel. Thick boron doped diamond single crystals for high power electronics. *Diamond and Related Materials*, 20(2):145 – 152, 2011.
- [58] M. Rayar, P. Supiot, P. Veis, and A. Gicquel. Optical emission study of a doped diamond deposition process by plasma enhanced chemical vapor deposition. *Journal of Applied Physics*, 104(3):-, 2008.

- [59] J. Ristein, W. Stein, and L. Ley. Defect spectroscopy and determination of the electron diffusion length in single crystal diamond by total photoelectron yield spectroscopy. *Phys. Rev. Lett.*, 78:1803–1806, Mar 1997.
- [60] C. Bandis and B. B. Pate. Electron emission due to exciton breakup from negative electron affinity diamond. *Phys. Rev. Lett.*, 74:777–780, Jan 1995.
- [61] I-Nan Lin, Satoshi Koizumi, Joan Yater, and Franz Koeck. Diamond electron emission. *MRS Bulletin*, 39:533–541, 6 2014.
- [62] M. I. Landstrass and K. V. Ravi. Resistivity of chemical vapor deposited diamond films. *Applied Physics Letters*, 55(10):975–977, 1989.
- [63] Sacharia Albin and Linwood Watkins. Electrical properties of hydrogenated diamond. *Applied Physics Letters*, 56(15):1454–1456, 1990.
- [64] Tetsuro Maki, Syozo Shikama, Masaaki Komori, Yoshiyuki Sakaguchi, Ken Sakuta, and Takeshi Kobayashi. Hydrogenating effect of single-crystal diamond surface. *Japanese Journal of Applied Physics*, 31(10A):L1446, 1992.
- [65] Yusuke Mori, Yoshiyuki Show, Masahiro Deguchi, Hiromasa Yagi, Hiroyuki Yagyū, Nobuhiro Eimori, Takashi Okada, Akimitsu Hatta, Kazuhito Nishimura, Makoto Kitabatake, Toshimichi Ito, Takashi Hirao, Tomio Izumi, Takatomo Sasaki, and Akio Hiraki. Characterization of surface conductive diamond layer grown by microwave plasma chemical vapor deposition. *Japanese Journal of Applied Physics*, 32(7B):L987, 1993.
- [66] Kazushi Hayashi, Sadanori Yamanaka, Hideyo Okushi, and Koji Kajimura. Study of the effect of hydrogen on transport properties in chemical vapor deposited diamond films by hall measurements. *Applied Physics Letters*, 68(3):376–378, 1996.
- [67] Kazushi Hayashi, Sadanori Yamanaka, Hideyuki Watanabe, Takashi Sekiguchi, Hideyo Okushi, and Koji Kajimura. Investigation of the effect of hydrogen on electrical and optical properties in chemical vapor deposited on homoepitaxial diamond films. *Journal of Applied Physics*, 81(2):744–753, 1997.
- [68] Hiroshi Kawarada, Hidehiro Sasaki, and Atsuhiko Sato. Scanning-tunneling-microscope observation of the homoepitaxial diamond (001) 2×1 reconstruction observed under atmospheric pressure. *Phys. Rev. B*, 52:11351–11358, Oct 1995.
- [69] F. Maier, M. Riedel, B. Mantel, J. Ristein, and L. Ley. Origin of surface conductivity in diamond. *Phys. Rev. Lett.*, 85:3472–3475, Oct 2000.

- [70] Sung Gi Ri, Tatsuhiro Mizumasa, Yukio Akiba, Yoichi Hirose, Tateki Kurosu, and Masamori Iida. Formation mechanism of p-type surface conductive layer on deposited diamond films. *Japanese Journal of Applied Physics*, 34(10R):5550, 1995.
- [71] J. B. Cui, J. Ristein, and L. Ley. Electron affinity of the bare and hydrogen covered single crystal diamond (111) surface. *Phys. Rev. Lett.*, 81:429–432, Jul 1998.
- [72] Tokuyuki Teraji, Yasuo Koide, and Toshimichi Ito. High-temperature stability of au/p-type diamond schottky diode. *physica status solidi (RRL) Rapid Research Letters*, 3(6):211–213, 2009.
- [73] Nan Jiang and Toshimichi Ito. Electrical properties of surface conductive layers of homoepitaxial diamond films. *Journal of Applied Physics*, 85(12):8267–8273, 1999.
- [74] J.F.H. Custers. Unusual phosphorescence of a diamond. *Physica*, 18(8-9):489 – 496, 1952.
- [75] J.F.H. Custers. Type {I Ib} diamonds. *Physica*, 20:183 – 184, 1954.
- [76] James J. Brophy. Preliminary study of the electrical properties of a semiconducting diamond. *Phys. Rev.*, 99:1336–1337, Aug 1955.
- [77] I G Austin and R Wolfe. Electrical and optical properties of a semiconducting diamond. *Proceedings of the Physical Society. Section B*, 69(3):329, 1956.
- [78] H B Dyer and P T Wedepohl. Electrical measurements on type iib diamonds. *Proceedings of the Physical Society. Section B*, 69(3):410, 1956.
- [79] C. D. Clark, R. W. Ditchburn, and H. B. Dyer. The absorption spectra of natural and irradiated diamonds. *Proceedings of the Royal Society of London A: Mathematical, Physical and Engineering Sciences*, 234(1198):363–381, 1956.
- [80] P T Wedepohl. Electrical and optical properties of type iib diamonds. *Proceedings of the Physical Society. Section B*, 70(2):177, 1957.
- [81] A T Collins and A W S Williams. The nature of the acceptor centre in semiconducting diamond. *Journal of Physics C: Solid State Physics*, 4(13):1789, 1971.
- [82] E. Gheeraert, A. Deneuve, and J. Mambou. Boron-related infra-red absorption in homoepitaxial diamond films. *Diamond and Related Materials*, 7(10):1509 – 1512, 1998.

- [83] R. M. Chrenko. Boron, the dominant acceptor in semiconducting diamond. *Phys. Rev. B*, 7:4560–4567, May 1973.
- [84] R.C. Burns, Vesna Cvetkovic, C.N. Dodge, D.J.F. Evans, Marie-Line T. Rooney, P.M. Spear, and C.M. Welbourn. Growth-sector dependence of optical features in large synthetic diamonds. *Journal of Crystal Growth*, 104(2):257 – 279, 1990.
- [85] V.D. Blank, M.S. Kuznetsov, S.A. Nosukhin, S.A. Terentiev, and V.N. Denisov. The influence of crystallization temperature and boron concentration in growth environment on its distribution in growth sectors of type {IIb} diamond. *Diamond and Related Materials*, 16:800 – 804, 2007. Proceedings of Diamond 2006, the 17th European Conference on Diamond, Diamond-Like Materials, Carbon Nanotubes, Nitrides and Silicon Carbide Diamond 2006.
- [86] N. V. Novikov, editor. *Физические свойства алмаза (Physical Properties of Diamond)*, page 117. Naukova Dumka, Kiev, 1987.
- [87] V. G. Malogolovets. Примесный бор в монокристаллах синтетического алмаза (boron impurity in synthetic diamond monocrystals). In N.V. Novikov, editor, *Международный семинар "Сверхтвердые материалы" (International Workshop "Superhard materials")*, volume T. 1, page 142. Ин-т сверхтвердых материалов АН УССР (Institute of Superhard Materials AN UkrSSR), Киев: ИСМ АН УССР (Kiev: ISM Akademija Nauk Ukrainskoj SSR), 17-21 June 1981.
- [88] G. Davies. The optical properties of diamond. In P.L. Walker and P.A. Throver, editors, *The Chemistry and Physics of Carbon*, pages 1–143. Marcel Dekker, New York, 1977.
- [89] L. B. Valdes. Resistivity measurements on germanium for transistors. *Proceedings of the IRE*, 42(2):420–427, Feb 1954.
- [90] F. M. Smits. Measurement of sheet resistivities with the four-point probe. *Bell System Technical Journal*, 37(3):711–718, 1958.
- [91] J.-P. Lagrange, A. Deneuve, and E. Gheeraert. Activation energy in low compensated homoepitaxial boron-doped diamond films. *Diamond and Related Materials*, 7(9):1390 – 1393, 1998.
- [92] A.T. Collins and E.C. Lightowers. Electrical properties. In J. E. Field, editor, *The Properties of Diamond*, chapter 3, pages 79–105. Academic Press, London, 1979.
- [93] E. Gheeraert, S. Koizumi, T. Teraji, H. Kanda, and M. Nešl̃dek. Electronic states of boron and phosphorus in diamond. *physica status solidi (a)*, 174(1):39–51, 1999.

- [94] M. Kadri, D. Araujo, M. Wade, A. Deneuve, and E. Bustarret. Effect of oxygen on the cathodoluminescence signal from excitons, impurities and structural defects in homoepitaxial (100) diamond films. *Diamond and Related Materials*, 14:566 – 569, 2005. Proceedings of Diamond 2004, the 15th European Conference on Diamond, Diamond-Like Materials, Carbon Nanotubes, Nitrides and Silicon Carbide 15th European Conference on Diamond, Diamond-Like Materials, Carbon Nanotubes, Nitrides and Silicon Carbide.
- [95] Pierre-Nicolas Volpe, Julien Pernot, Pierre Muret, and Franck Omnès. High hole mobility in boron doped diamond for power device applications. *Applied Physics Letters*, 94(9):–, 2009.
- [96] Sadanori Yamanaka, Hideyuki Watanabe, Shigeo Masai, Daisuke Takeuchi, Hideyo Okushi, and Koji Kajimura. High-quality b-doped homoepitaxial diamond films using trimethylboron. *Japanese Journal of Applied Physics*, 37(10A):L1129, 1998.
- [97] A. Hatta, S. Sonoda, and T. Ito. Electrical properties of b-doped homoepitaxial diamond films grown from {UHP} gas sources. *Diamond and Related Materials*, 8(8–9):1470 – 1475, 1999.
- [98] B.A. Fox, M.L. Hartsell, D.M. Malta, H.A. Wynands, C.-T. Kao, L.S. Plano, G.J. Tessmer, R.B. Henard, J.S. Holmes, A.J. Tessmer, and D.L. Dreifus. Diamond devices and electrical properties. *Diamond and Related Materials*, 4(5–6):622 – 627, 1995. Diamond Films '94.
- [99] J.A. Von Windheim, V. Venkatesan, D.M. Malta, and K. Das. Electrical characterization of semiconducting diamond thin films and single crystals. *Journal of Electronic Materials*, 22(4):391–398, 1993.
- [100] E P Visser, G J Bauhuis, G Janssen, W Vollenberg, J P van Enkevort, and L J Giling. Electrical conduction in homoepitaxial, boron-doped diamond films. *Journal of Physics: Condensed Matter*, 4(36):7365, 1992.
- [101] G. L. Pearson and J. Bardeen. Electrical properties of pure silicon and silicon alloys containing boron and phosphorus. *Phys. Rev.*, 75:865–883, Mar 1949.
- [102] T. H. Borst and O. Weis. Boron-doped homoepitaxial diamond layers: Fabrication, characterization, and electronic applications. *physica status solidi (a)*, 154(1):423–444, 1996.
- [103] Hideaki Maeda, Kyo Ohtsubo, Masanori Kameta, Takeyasu Saito, Katsuki Kusakabe, Shigeharu Morooka, and Tanemasa Asano. Growth behavior of boron-doped diamond

in microwave plasma-assisted chemical vapor deposition using trimethylboron as the dopant source. *Diamond and Related Materials*, 7(1):88 – 95, 1998.

- [104] Koichi Ushizawa, Kenji Watanabe, Toshihiro Ando, Isao Sakaguchi, Mikka Nishitani-Gamo, Yoichiro Sato, and Hisao Kanda. Boron concentration dependence of raman spectra on 100 and 111 facets of b-doped {CVD} diamond. *Diamond and Related Materials*, 7:1719 – 1722, 1998.
- [105] T. Bauer, M. Schreck, H. Sternschulte, and B. Stritzker. High growth rate homoepitaxial diamond deposition on off-axis substrates. *Diamond and Related Materials*, 14:266 – 271, 2005. Proceedings of Diamond 2004, the 15th European Conference on Diamond, Diamond-Like Materials, Carbon Nanotubes, Nitrides and Silicon Carbide 15th European Conference on Diamond, Diamond-Like Materials, Carbon Nanotubes, Nitrides and Silicon Carbide.
- [106] P. W. May, J. N. Harvey, N. L. Allan, J. C. Richley, and Yu. A. Mankelevich. Simulations of chemical vapor deposition diamond film growth using a kinetic monte carlo model. *Journal of Applied Physics*, 108(1):–, 2010.
- [107] Mitsuhiro Hamada, Tokuyuki Teraji, and Toshimichi Ito. Hillock-free homoepitaxial diamond (100) films grown at high methane concentrations. *Japanese Journal of Applied Physics*, 44(1L):L216, 2005.
- [108] Paul W May, Neil L Allan, Michael N R Ashfold, James C Richley, and Yuri A Mankelevich. Simplified monte carlo simulations of chemical vapour deposition diamond growth. *Journal of Physics: Condensed Matter*, 21(36):364203, 2009.
- [109] Masahiko Ogura, Hiromitsu Kato, Toshiharu Makino, Hideyo Okushi, and Satoshi Yamasaki. Misorientation-angle dependence of boron incorporation into (0 0 1)-oriented chemical-vapor-deposited (cvd) diamond. *Journal of Crystal Growth*, 317(1):60 – 63, 2011.
- [110] Hitoshi Umezawa, Norio Tokuda, Masahiko Ogura, Sung-Gi Ri, and Shinichi Shikata. Characterization of leakage current on diamond schottky barrier diodes using thermionic-field emission modeling. *Diamond and Related Materials*, 15(11-12):1949 – 1953, 2006. Proceedings of the joint 11th International Conference on New Diamond Science and Technology and the 9th Applied Diamond Conference 2006 ICNDST-ADC 2006.
- [111] Natsuo Tatsumi, Kazuhiro Ikeda, Hitoshi Umezawa, and Shinichi Shikata. Development of diamond schottky barrier diode. *SEI Tech. Rev*, pages 54–61, 2009.

- [112] Hitoshi Umezawa, Takeyasu Saito, Norio Tokuda, Masahiko Ogura, Sung-Gi Ri, Hiromichi Yoshikawa, and Shinichi Shikata. Leakage current analysis of diamond schottky barrier diode. *Applied Physics Letters*, 90(7):073506, 2007.
- [113] Shinya Ohmagari, Tokuyuki Teraji, and Yasuo Koide. Non-destructive detection of killer defects of diamond schottky barrier diodes. *Journal of Applied Physics*, 110(5):056105, 2011.
- [114] Tokuyuki Teraji, Yasuo Koide, and Toshimichi Ito. Schottky barrier height and thermal stability of p-diamond (100) schottky interfaces. *Thin Solid Films*, 557(0):241 – 248, 2014. The 8th International Conference on Silicon Epitaxy and Heterostructures (ICSI-8) and the 6th International Symposium on Control of Semiconductor Interfaces (ISCSI-VI).
- [115] M. Muehle, M.F. Becker, T. Schuelke, and J. Asmussen. Substrate crystal recovery for homoepitaxial diamond synthesis. *Diamond and Related Materials*, 42(0):8 – 14, 2014.
- [116] Thomas Schuelke and Timothy A. Grotjohn. Diamond polishing. *Diamond and Related Materials*, 32(0):17 – 26, 2013.
- [117] K. Ueda, K. Kawamoto, T. Soumiya, and H. Asano. High-temperature characteristics of ag and ni/diamond schottky diodes. *Diamond and Related Materials*, 38(0):41 – 44, 2013.
- [118] A. Traore, P. Muret, A. Fiori, D. Eon, E. Gheeraert, and J. Pernot. Zr/oxidized diamond interface for high power schottky diodes. *Applied Physics Letters*, 104(5):052105, 2014.
- [119] A. Fiori, T. Teraji, and Y. Koide. Diamond schottky diodes with ideality factors close to 1. *Applied Physics Letters*, 105(13):133515, 2014.